

Synthesis, Properties, and Applications of Multifunctional Magnetic Nanostructures

Lead Guest Editor: Vidyadhar Singh

Guest Editors: Rajasekhar Madugundo, Anil Annadi, Biswanath Bhoi,
K. Devi Chandrasekhar, and Murtaza Bohra





Synthesis, Properties, and Applications of Multifunctional Magnetic Nanostructures

Journal of Nanomaterials

Synthesis, Properties, and Applications of Multifunctional Magnetic Nanostructures

Lead Guest Editor: Vidyadhar Singh

Guest Editors: Rajasekhar Madugundo, Anil Annadi,
Biswanath Bhoi, K. Devi Chandrasekhar, and Murtaza Bohra



Copyright © 2017 Hindawi. All rights reserved.

This is a special issue published in "Journal of Nanomaterials." All articles are open access articles distributed under the Creative Commons Attribution License, which permits unrestricted use, distribution, and reproduction in any medium, provided the original work is properly cited.

Editorial Board

Domenico Acierno, Italy
Katerina Aifantis, USA
Nageh K. Allam, USA
Margarida Amaral, Portugal
Martin Andersson, Sweden
Raul Arenal, Spain
Ilaria Armentano, Italy
Vincenzo Baglio, Italy
Lavinia Balan, France
Thierry Baron, France
Andrew R. Barron, USA
Hongbin Bei, USA
Stefano Bellucci, Italy
Enrico Bergamaschi, Italy
Debes Bhattacharyya, New Zealand
Sergio Bietti, Italy
Giovanni Bongiovanni, Italy
Mohamed Bououdina, Bahrain
Philippe Caroff, Australia
Victor M. Castaño, Mexico
Albano Cavaleiro, Portugal
Bhanu P. S. Chauhan, USA
Shafiq Chowdhury, USA
Jin-Ho Choy, Republic of Korea
Yu-Lun Chueh, Taiwan
Elisabetta Comini, Italy
Giuseppe Compagnini, Italy
David Cornu, France
Miguel A. Correa-Duarte, Spain
P. Davide Cozzoli, Italy
Yong Ding, USA
Zehra Durmus, Turkey
Joydeep Dutta, Oman
Ovidiu Ersen, France
Claude Estournès, France
Andrea Falqui, KSA
Matteo Ferroni, Italy
Ilaria Fratoddi, Italy
Miguel A. Garcia, Spain
Siddhartha Ghosh, Singapore
Filippo Giubileo, Italy
Fabien Grasset, France
Jean M. Greneche, France

Kimberly Hamad-Schifferli, USA
Simo-Pekka Hannula, Finland
Michael Harris, USA
Yasuhiko Hayashi, Japan
Michael Z. Hu, USA
Nay Ming Huang, Malaysia
Zafar Iqbal, USA
Balachandran Jeyadevan, Japan
Jeong-won Kang, Republic of Korea
Hassan Karimi-Maleh, Iran
Antonios Kelarakis, UK
Alireza Khataee, Iran
Ali Khorsand Zak, Iran
Philippe Knauth, France
Prashant Kumar, UK
Eric Le Bourhis, France
Jun Li, Singapore
Meiyong Liao, Japan
Shijun Liao, China
Silvia Licocchia, Italy
Nathan C. Lindquist, USA
Zainovia Lockman, Malaysia
Jim Low, Australia
Laura M. Maestro, Spain
Gaurav Mago, USA
Muhamamd A. Malik, UK
Francesco Marotti de Sciarra, Italy
Sanjay R. Mathur, Germany
Tony McNally, UK
Yogendra Mishra, Germany
Paulo Cesar Morais, Brazil
Paul Munroe, Australia
Jae-Min Myoung, Republic of Korea
Rajesh R. Naik, USA
Albert Nasibulin, Russia
Toshiaki Natsuki, Japan
Natalia Noginova, USA
Sherine Obare, USA
Won-Chun Oh, Republic of Korea
Abdelwahab Omri, Canada
Ungyu Paik, Republic of Korea
Piersandro Pallavicini, Italy
Edward A. Payzant, USA

Alessandro Pegoretti, Italy
Oscar Perales-Pérez, Puerto Rico
Jorge Pérez-Juste, Spain
Alexey P. Popov, Finland
Helena Prima-García, Spain
Alexander Pyatenko, Japan
You Qiang, USA
Philip D. Rack, USA
Peter Reiss, France
Ilker S. Bayer, Italy
Sudipta Seal, USA
Shu Seki, Japan
Donglu Shi, USA
Bhanu P. Singh, India
Surinder Singh, USA
Vladimir Sivakov, Germany
Adolfo Speghini, Italy
Marinella Striccoli, Italy
Xuping Sun, KSA
Ashok K. Sundramoorthy, India
Angelo Taglietti, Italy
Bo Tan, Canada
Leander Tapfer, Italy
Valeri P. Tolstoy, Russia
Muhammet S. Toprak, Sweden
R. Torrecillas, Spain
Achim Trampert, Germany
Takuya Tsuzuki, Australia
Tamer Uyar, Turkey
Luca Valentini, Italy
Antonio Vassallo, Italy
Ester Vazquez, Spain
Ajayan Vinu, Australia
Ruibing Wang, Macau
Shiren Wang, USA
Yong Wang, USA
Magnus Willander, Sweden
Ping Xiao, UK
Zhi Li Xiao, USA
Yoke K. Yap, USA
William Yu, USA
Michele Zappalorto, Italy
Renyun Zhang, Sweden

Contents

Synthesis, Properties, and Applications of Multifunctional Magnetic Nanostructures

Vidyadhar Singh, Rajasekhar Madugundo, Anil Annadi, Biswanath Bhoi, K. Devi Chandrasekhar, and Murtaza Bohra

Volume 2017, Article ID 2638715, 2 pages

Influence of the Distance between Nanoparticles in Clusters on the Magnetization Reversal Process

Andrea Ehrmann and Tomasz Blachowicz

Volume 2017, Article ID 5046076, 6 pages

Writing Field Analysis for Shingled Bit-Patterned Magnetic Recording

X. G. Li, Z. J. Liu, A. G. Kang, and X. Y. Xie

Volume 2017, Article ID 4254029, 9 pages

Development of Stabilized Magnetite Nanoparticles for Medical Applications

Ioana Lavinia Ardelean, Luric Bogdan Niculae Stoencea, Denisa Ficai, Anton Ficai, Roxana Trusca, Bogdan Stefan Vasile, Gheorghe Nechifor, and Ecaterina Andronescu

Volume 2017, Article ID 6514659, 9 pages

Magnetic Mineral Nanocomposite Sorbents for Wastewater Treatment

Oksana Makarchuk, Tetiana Dontsova, Anatolii Perekos, Alexander Skoblik, and Yevhen Svystunov

Volume 2017, Article ID 8579598, 7 pages

Investigation of Various Cross-Linking Methods for the Immobilization of Cytosine Arabinoside on Bacterial Magnetosomes

Qinglei Dai, Yiming Ma, Shibin Wang, Ranjith Kumar Kankala, and Yuangang Liu

Volume 2017, Article ID 6738484, 7 pages

Preparation and Characterization of a Tumor-Targeting Dual-Image System Based on Iron Oxide Nanoparticles Functionalized with Folic Acid and Rhodamine

Alejandra Ancira-Cortez, Enrique Morales-Avila, Blanca E. Ocampo-García, Carlos González-Romero, Luis A. Medina, Gustavo López-Téllez, and Erick Cuevas-Yáñez

Volume 2017, Article ID 5184167, 11 pages

Room Temperature Ferromagnetic and Optical Properties of Chrome Doped ZnS Nanorods Prepared by Hydrothermal Method

Wenhua Zhao, Zhiqiang Wei, Li Zhang, Xiaojuan Wu, Xuan Wang, and Jinlong Jiang

Volume 2017, Article ID 9378349, 8 pages

Biocompatibility and Toxicity of Polylactic Acid/Ferrosulfate Nanomagnetic Microsphere

Hongzhao Xiang, Yuanhua Mu, Chengbo Hu, and Xiaobing Luo

Volume 2017, Article ID 5429063, 8 pages

Effect of Annealing Temperature and Spin Coating Speed on Mn-Doped ZnS Nanocrystals Thin Film by Spin Coating

Noor Azie Azura Mohd Arif, Chong Chee Jiun, and Sahbudin Shaari

Volume 2017, Article ID 2560436, 6 pages

Editorial

Synthesis, Properties, and Applications of Multifunctional Magnetic Nanostructures

**Vidyadhar Singh,¹ Rajasekhar Madugundo,² Anil Annadi,³ Biswanath Bhoi,⁴
K. Devi Chandrasekhar,⁵ and Murtaza Bohra⁶**

¹*Nanoparticles by Design Unit, Okinawa Institute of Science and Technology (OIST) Graduate University, 1919-1 Tancha, Onna-son, Okinawa 904-0495, Japan*

²*BCMaterials, Bizkaia Science and Technology Park, 48160 Derio, Spain*

³*Institute for Molecular Engineering, University of Chicago, Chicago, IL 60637, USA*

⁴*Seoul National University, Seoul 08826, Republic of Korea*

⁵*Department of Physics, National Sun Yat-sen University, Kaohsiung 80424, Taiwan*

⁶*Mahindra École Centrale College of Engineering, Hyderabad 500043, India*

Correspondence should be addressed to Vidyadhar Singh; vidya.singh@oist.jp

Received 24 July 2017; Accepted 24 July 2017; Published 25 October 2017

Copyright © 2017 Vidyadhar Singh et al. This is an open access article distributed under the Creative Commons Attribution License, which permits unrestricted use, distribution, and reproduction in any medium, provided the original work is properly cited.

Magnetic nanostructures have emerged as a novel class of materials being used in variety of applications such as ultra-high-density magnetic recording media, drug delivery, magnetic resonance imaging, sensing, hyperthermia, and catalysts. These magnetic nanostructures can be synthesized in various forms ranging from nanoparticles, nanoclusters, nanorods, nanowires, and nanotubes to the thin films and multilayers, depending upon growth conditions. During last decade, interest in magnetic nanostructures has grown exponentially being inspired by recent advances in nanostructure growth and characterization techniques from which various fascinating properties can be realized which were not observed in the bulk material. These distinct properties can be ascribed to the energies associated with various physical parameters; those are comparable with size of nanostructures. Control over these properties enables researcher to develop new concepts that would lead to novel end products.

In this special issue, total of nine manuscripts were accepted for publication. These manuscripts are mainly focused on synthesis and characterizations of multifunctional magnetic nanostructures and their promising applications. We hope that these articles will give the readers useful information and pathway for futuristic scientific applications. In the following, we will summarize the results from accepted manuscripts.

A. Ehrmann et al. theoretically simulated the magnetic states at remanence for particle of two different shapes at nanoscale. For clusters of these particles, the probability of reaching the additional intermediate onion states in the same field region is strongly reduced with decreased interparticle distance. Significantly, the intermediate onion state, often found in fourfold nanoparticles with open core, which is shown to be stable for interparticle distance down to 12 nm in specific shape arrangement is of technological interest due to the possibility of using such particles in quaternary memory devices. These findings on understanding the interparticle interactions between both shapes indicate possible solution is in the form of designing new magnetic nanoparticle shapes.

X. G. Li et al. reported a novel method for the analysis of the combined influence of writing head geometry and media properties on writing field performance. They have used the response surface methodology (RSM) for this work. Author analyzed the influence of several parameters such as shielding trailing gap, medium coercivity, and shielding side gap on the effective writing field (EWF) gradient. Their method is useful for evaluation of the bit error rate and SNR of shingled bit patterned recording systems.

W. Zhao et al. studied Cr doped ZnS nanorods synthesized by hydrothermal method. The authors investigated the magnetic and optical properties of $Zn_{1-x}Cr_xS$ nanorods as

a function of Cr concentration. The authors found that as the concentration of Cr increased, the blue emissions intensity improved and the band gap underwent blue shift while the saturation magnetization weakened significantly compared to pure ZnS.

N. A. A. M. Arif et al. proposed a cost effective and simple conventional spin coating method to synthesize high quality sphere-like ZnS:Mn nanocrystalline thin films. The authors investigated the effect of annealing temperature and spin coating speed on the structural and optical properties of Mn-doped ZnS nanocrystalline thin film. The direct band gap for the films was found within the range 4.43 eV–4.60 eV and the absorption spectra for the films have a limiting wavelength of 250 nm. It was also demonstrated that the decrement in annealing temperature results in improvement of the properties.

I. L. Ardelean et al. developed a facile method to synthesize magnetite nanoparticles with mesoporous structure by coprecipitation method using different stabilizing agents like salicylic acid, glutamic acid, and trichloroacetic acid. They used stabilizing agent to prevent the aggregation of the magnetite nanocrystals and to obtain stable nanostructures even in the biological environment. These nanoparticles are potential candidates for contrast agents as well as targeted carrier for specific diseases, especially cancer.

O. Makarchuk et al. synthesized magnetic nanocomposite sorbents for disposal of synthetic detergents from wastewater. Obtained sorbents based on clay minerals (saponite, palygorskite, and spondyle clay) and magnetite were characterized by X-ray powder diffraction, Mössbauer spectroscopy, and ballistic method with Steinberg magnetometer. The efficiency of magnetic composites and implementing of magnetic separation in adsorption purification was confirmed.

A. Ancira-Cortez et al. described the preparation of a dual-image targeting system composed of magnetic iron oxide nanoparticles functionalized with folic acid and rhodamine in order to achieve and enhance the detection of cancer. Folic acid and rhodamine were conjugated with high efficiency. A significant selectivity and uptake, facilitated by surface modification of iron oxide nanoparticles with folic acid, were demonstrated. The multifunctional system showed suitable physicochemical and biological properties for cell targeting through folate receptors.

Finally, Q. Dai et al. investigated the bacterial magnetosomes (BMs), which have potential in drug delivery vehicles, possessing an iron oxide or iron sulfide core surrounded by a natural lipid membrane shell. They immobilized cytosine arabinoside (Ara-C) effectively on BMs by using various methods such as direct absorption (ABMs), and others include different cross-linkers such as genipin (GP) and glutaraldehyde (G). The results indicate that BMs-based nanoconjugates will potentially find widespread applications in pharmaceutical field. Additionally, H. Xiang et al. prepared Fe₃O₄ magnetic nanoparticle coated by PLA and then investigated detail structure, morphology, and biocompatibility of PLA/Fe₃O₄ microsphere. Their study demonstrates that, in comparison with liver cell, liver cancer cells (HepG2) are easy to be disturbed by PLA/Fe₃O₄ nanomagnetic microspheres, which have higher sensitivity and absorption ability. Their

finding can take advantage of the susceptible property of cancer cells for carriers to improve targeted drug function.

Acknowledgments

We would like to express our gratitude to all the authors for their contribution and all reviewers for their critical inputs.

Vidyadhar Singh
Rajasekhar Madugundo
Anil Annadi
Biswanath Bhoi
K. Devi Chandrasekhar
Murtaza Bohra

Research Article

Influence of the Distance between Nanoparticles in Clusters on the Magnetization Reversal Process

Andrea Ehrmann¹ and Tomasz Blachowicz²

¹Faculty of Engineering and Mathematics, Bielefeld University of Applied Sciences, Interaktion 1, 33619 Bielefeld, Germany

²Institute of Physics-Center for Science and Education, Silesian University of Technology, Ul. Konarskiego 22B, 44-100 Gliwice, Poland

Correspondence should be addressed to Andrea Ehrmann; andrea.ehrmann@fh-bielefeld.de

Received 27 March 2017; Accepted 12 July 2017; Published 20 August 2017

Academic Editor: Anil Annadi

Copyright © 2017 Andrea Ehrmann and Tomasz Blachowicz. This is an open access article distributed under the Creative Commons Attribution License, which permits unrestricted use, distribution, and reproduction in any medium, provided the original work is properly cited.

Fourfold magnetic nanoparticles, created from nanowires or in the form of an open square, offer the possibility of creating quaternary memory devices with four unambiguously distinguishable stable states at remanence. This feature, however, has been simulated for single magnetic nanoparticles or clusters with interparticle distances similar to the nanoparticle dimensions. For the possible use in bit-patterned media, it is important to understand the scaling behavior of the stability of the additional intermediate states with the interparticle distance. The paper investigates exemplarily nanoparticles of two shapes which were found to be optimum to gain four states at remanence. For clusters of these particles, the probability of reaching the additional intermediate states in all particles in the same field region is strongly reduced with decreased interparticle distance. The differences between both shapes indicate possible solutions for this problem in the form of new nanoparticle shapes.

1. Introduction

Magnetic nanoparticles are of technological interest, for example, for magnetic storage media, magnetic sensors, and MRAMs [1–3]. Since their overall anisotropy is governed by the shape anisotropy [4], tailoring a nanoparticle's form allows for adjusting its magnetic properties. This is important for the possible use of nanoparticles in bit-patterned media or other applications in which defined anisotropies are necessary. One possible shape consists of a fourfold ring with different shape modifications, leading to two additional magnetic states at remanence which could be used to create quaternary memory systems [5]. In this way, data storage density could be increased by increasing the number of bits per particle instead of increasing the particle density. This approach has also been followed by other groups, resulting in three, four, or up to eight magnetization states in diverse nanostructures [6–10].

Problematic in all these magnetic systems, however, is the interaction between neighboring nanostructures, often strongly modifying the single nanoparticle's magnetic properties. For multilayer systems, for example, distances of 30 nm

were found to be sufficient to approximate independent magnetic behavior of the layers [11]. In an array of nanotubes with distances of 30 nm or 60 nm, however, even the larger distance showed a significant influence of the cluster structure on magnetization reversal, especially by nearly completely annihilating a step in the hysteresis loop which occurred for single nanotubes of identical geometry [12]. Since such a step is also necessary for reaching stable intermediate states at remanence, this finding indicates possible problems with downscaling the fourfold ring structure under investigation here. For a large cluster of nanodots, the geometric shape in which the lowest stray fields and thus the smallest influences between nanoparticles can be expected, nearly random magnetization orientations were found lately [13].

Nevertheless, for the systems under investigation here, it was found in another project that nanoparticles with diameters of 120 nm and identical interparticle distances did nearly not change their coercive fields and retained a collective intermediate onion state which is necessary for the creation of quaternary memory devices [14]. Due to the necessity to further minimize such nanoparticle clusters, it is, however, necessary to investigate the influence of further

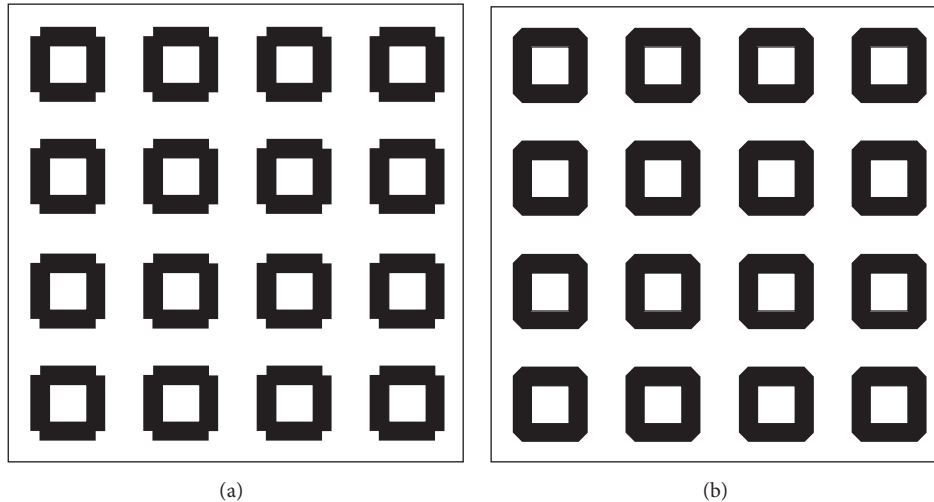


FIGURE 1: Clusters of 4×4 fourfold nanoparticles, showing two different shapes, here defined as “square corner cuts” (a) and “diagonal corner cuts” (b).

reduced distances between the single particles of specific shape, ordered in a cluster.

2. Materials and Methods

Modelling was performed using the micromagnetic simulator OOMMF (Object Oriented MicroMagnetic Framework) [15]. This program is based on finite differences (discretizing space into small cuboids) and utilizes the Landau-Lifshitz-Gilbert (LLG) equation of motion [16].

All simulations were performed using iron (Fe) which has proven to show ideal properties in terms of stable intermediate states [17]. The following parameters were used for modelling, being consistent with typical literature values [18]: saturation magnetization $M_S = 1700 \cdot 10^3$ A/m, exchange constant $A = 21 \cdot 10^{-12}$ J/m, anisotropy constant $K_1 = 48 \cdot 10^3$ J/m³, Gilbert damping constant $\alpha = 0.1$, and mesh diameter $d = 5$ nm. Since such samples are mostly produced by sputtering in reality, the anisotropy was assumed to have randomly oriented axes in each cell.

While the external magnetic field was applied parallel to the sample plane, the orientation of the sample was varied between 0° (defined as parallel orientation of the external magnetic field to the x -axis of the sample, i.e., to one side of the nanoparticle) and 45° in steps of 5° . To ensure that magnetization saturation is reached, external fields were swept within ± 0.25 T.

For the simulation, clusters of 4×4 particles were modelled. The particles under simulation here had slightly different geometries (Figure 1): one of them, defined as “square corner cuts,” has an ideal structure which has shown to lead to two additional intermediate states at remanence [5], while the other one, denoted as “diagonal corner cuts,” has a more realistic shape, as recognized in former lithographically produced nanostructures [19, 20]. Lateral dimensions of each nanoparticle were 120 nm in the sample plane and 5 nm height, corresponding to the smallest samples used in former

experimental investigations [19, 20]. This value was chosen since the aim of this study is to find the highest possible particle density and thus the highest data density. Distances between the nanoparticles were reduced stepwise from 60 nm (1/2 of the nanoparticle diameters) to 12 nm (1/10 of the nanoparticle diameters).

For simulations of single particles, the shapes used here result, amongst others, in the magnetic states depicted in Figure 2. From positive saturation, magnetization switches in a first step into a horseshoe state and afterwards into an onion state. This onion state can be relaxed to zero external magnetic field, resulting in an intermediate, stable state at remanence. Proceeding further to negative saturation, a second horseshoe state becomes visible before finally negative saturation is reached.

Depending on the angle and the exact shape of the single nanoparticle, the horseshoe states may vanish. Intermediate onion states, correlated with stable additional states at remanence, occur in both systems usually in an angular region between 1° and 15° . Additionally, the onion states usually occur in a wider field range than the horseshoe states and are thus of higher technological interest than the horseshoe states and therefore investigated here.

3. Results and Discussion

In Figure 3, hysteresis loops are visible, which are simulated for a sample orientation of 5° on nanoparticles with diagonal corner cuts. While the hysteresis loops for the single particle (black line) and for the 4×4 cluster with interparticle distances half of the particle diameters (red line) are nearly identical, the cluster with interparticle distances of only a quarter of the particle diameters (green line) results in a significantly modified hysteresis loop. Apparently the interaction between particles spaced by distances of half the particle size can still be neglected, while significant interactions occur at smaller distances.

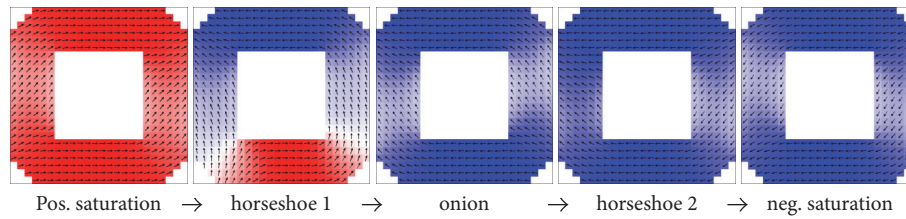


FIGURE 2: Typical magnetization reversal process for single particles at small angles (with or without horseshoe states possible, here shown for 5° , particle size 120 nm).

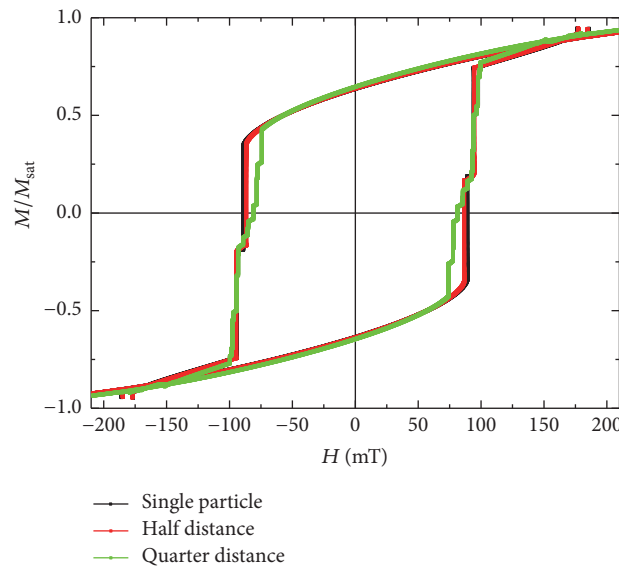


FIGURE 3: Hysteresis loops, simulated for nanoparticles with diagonal corner cuts at 5° , here depicted for a single particle (black line) and clusters with interparticle distances half of the particle diameters (red line) or a quarter of the particle diameters (green line).

Due to this finding, the simulated clusters were modified with respect to their interparticle distances in a range between half the particle dimension and $1/8$ of the particle dimension. In Figure 4, the results for the nanoparticles with diagonal corner cuts can be found.

Firstly, the coercive fields are only slightly modified between the four different situations. The magnetic states, however, change significantly.

For the single particle, at small angles the magnetization reversal proceeds as depicted in Figure 2: Directly at the coercive field, a first horseshoe state is reached, followed by an onion state and a second horseshoe state, marked as blue bar, green bar, and dark blue bar, respectively, in Figure 4. At 20° , the second horseshoe state vanishes; at higher angles, both other states vanish, too, and magnetization reversal occurs via a 180° flip from positive to negative saturation without stable intermediate states. The “blank” areas are correlated with mixed states in which some of the particles of the cluster show one magnetization state and other particles are in another state.

For the cluster with interparticle distances of half the nanoparticle dimensions, the second horseshoe state is completely gone, and the onion state as well as the first horseshoe state is significantly reduced. It should be mentioned that,

in all graphs, only the areas in which all particles in the cluster show the identical state are marked as belonging to the respective magnetization states.

Proceeding to $1/4$ interparticle distance (i.e., 30 nm), the field regions in which all cluster particles are simultaneously in the first horseshoe or the onion state are further reduced. At the $1/8$ interparticle distance, finally, only for one angle the onion state is retained, although with a significantly reduced field region.

Similar results can be found in the simulations of particles with square corner cuts, as depicted in Figure 5. Here, additional states occur, building a vortex with one or two domain walls. While the original single nanoparticle offers a broad spectrum of different magnetic states, most of the coherent states in the higher angle regime are already vanished for the cluster with distances identical to half the particle diameter. Decreasing the interparticle distances further, the coherent states become smaller again, until they completely vanish for the cluster with interparticle distances of $1/8$ of the particle diameters.

Figure 6 shows the widths of the field areas in which all nanoparticles of a cluster are in the onion state at a field orientation of 5° , depicted as a function of the inverse interparticle distance. For both nanoparticle shapes, the

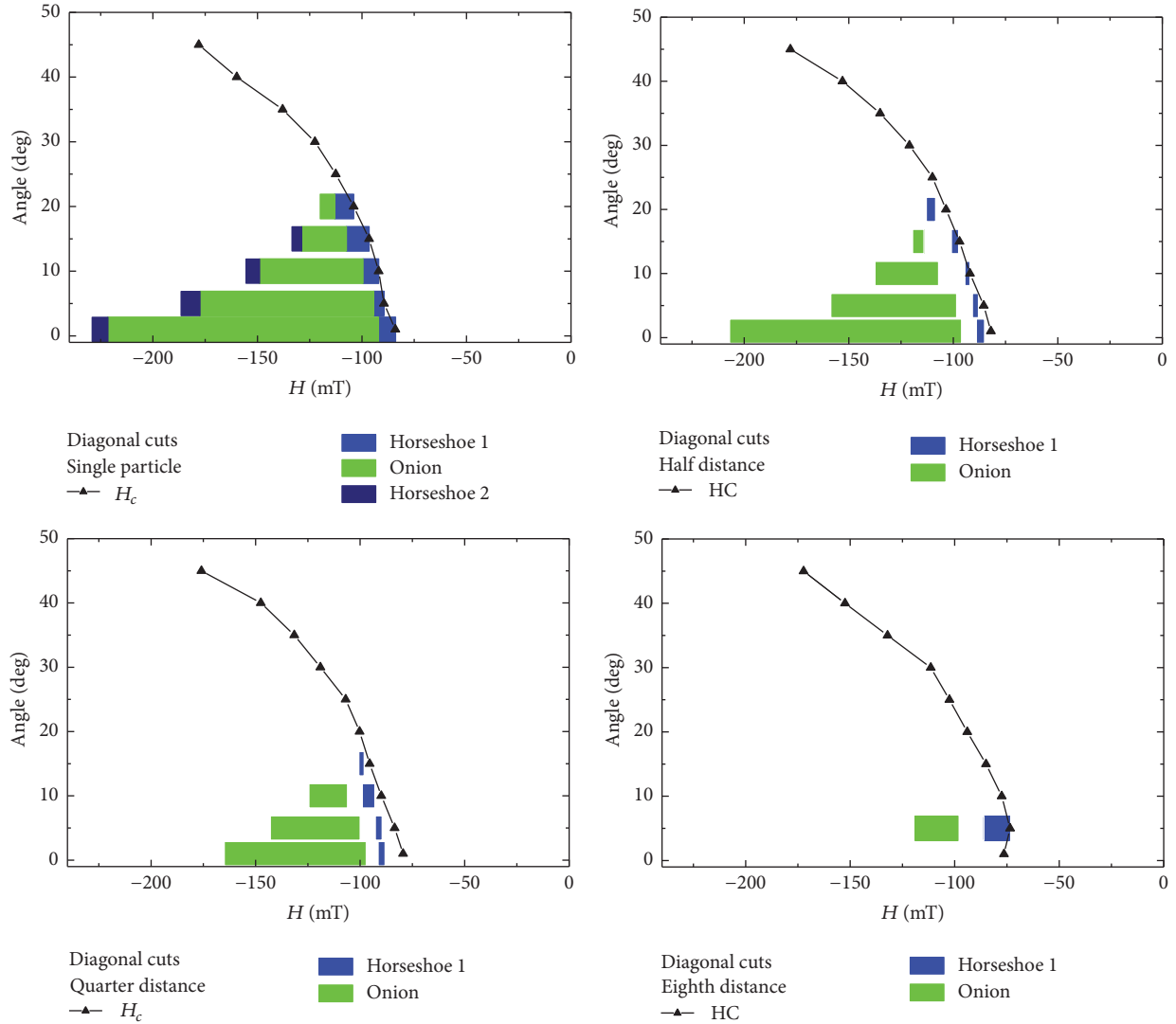


FIGURE 4: Coercive fields and field regions of different coherent magnetic states, as described in the text, for samples with diagonal corner cuts.

correlation is not exactly linear. As derived from Figures 4 and 5, the clusters with diagonal corner cuts show coherent behavior for smaller interparticle distances; however, for a distance of 12 nm between the particles ($= 1/10$ of the nanoparticle diameter), the onion state vanishes here, too.

Thus, additional nanoparticle shapes were tested by building 4×4 clusters with 12 nm interparticle distances and simulating their magnetization reversal behavior for a sample orientation of 5° . This orientation was chosen in agreement with Figure 4 which showed that here the coherent behavior was kept the longest. Figure 7 depicts a few of the tested clusters with the corresponding widths of the coherently ordered onion states. As can be seen here, not only are inner and outer shapes of the nanoparticles of importance, but also their orientation towards the neighbors is crucial. This suggests that biomimetic structures, such as the Fibonacci spirals [21] well-known from sunflowers and several other plants and animals, may be an interesting approach to create

nanoparticle patterns in which the interactions between neighboring particles are as small as possible.

4. Conclusions

Using micromagnetic simulations, we have shown that even for simulated, and thus quite symmetric, particles forming clusters, the dipolar-like interactions between them strongly disturb the formation of coherently ordered magnetization states in which all particles are in the same magnetic state. Particularly, the onion state often found in fourfold nanoparticles with open core, which is of technological interest due to the possibility of using such particles in quaternary memory devices, cannot be maintained for too small distances between neighboring particles.

By modification of shapes and arrangement of the original nanoparticle clusters, new structures could be found in which the particles of 120 nm could be approached to

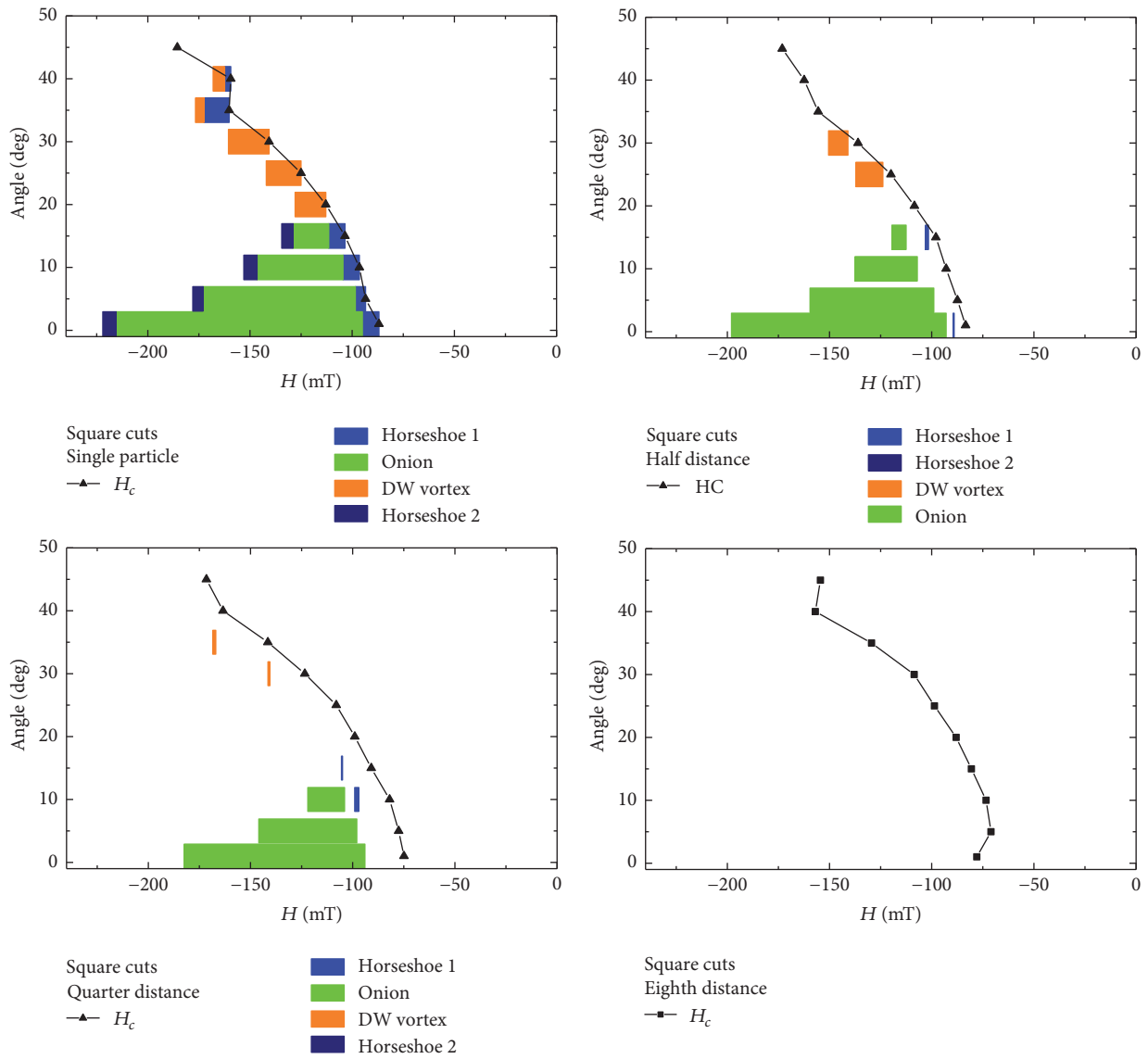


FIGURE 5: Coercive fields and field regions of different coherent magnetic states, as described in the text, for samples with square corner cuts.

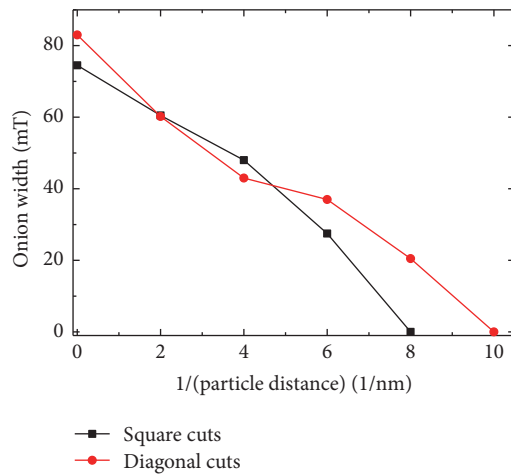


FIGURE 6: Field areas in which onion states occur coherently for clusters investigated at 5° versus the inverse interparticle distances.

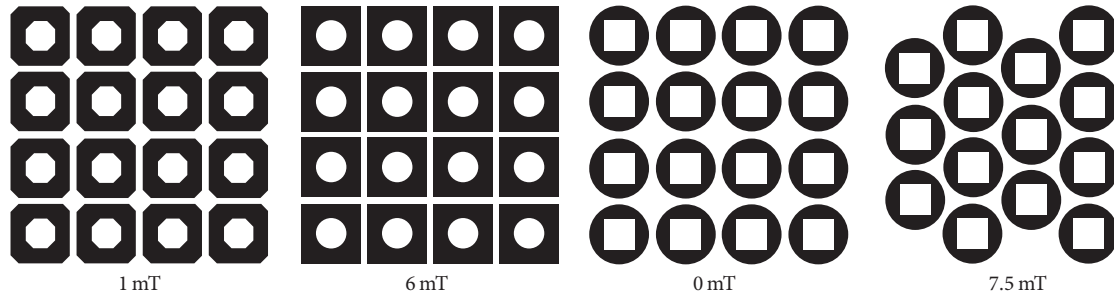


FIGURE 7: Different clusters under simulation, consisting in most cases of 4×4 particles with interparticle distances of 12 nm, and respective widths of coherent onion states.

distances of 12 nm without losing the coherent onion state. These findings suggest new solutions to design clusters of independent magnetic nanoparticles.

Conflicts of Interest

The authors declare that there are no conflicts of interest regarding the publication of this paper.

References

- [1] C. Vogler, F. Bruckner, M. Fuger et al., “Three-dimensional magneto-resistive random access memory devices based on resonant spin-polarized alternating currents,” *Journal of Applied Physics*, vol. 109, no. 12, article 123901, 2011.
- [2] U. Roy, H. Seinige, F. Ferdousi, J. Mantey, M. Tsoi, and S. K. Banerjee, “Spin-transfer-torque switching in spin valve structures with perpendicular, canted, and in-plane magnetic anisotropies,” *Journal of Applied Physics*, vol. 111, no. 7, article 07C913, 2012.
- [3] S. Yoon, Y. Jang, Ch. Nam et al., “Sensitivity enhancement of a giant magnetoresistance alternating spin-valve sensor for high-field applications,” *Journal of Applied Physics*, vol. 111, article 07E504, 2012.
- [4] J. Åkerman, “Toward a universal memory,” *Science*, vol. 308, no. 5721, pp. 508–510, 2005.
- [5] T. Blachowicz and A. Ehrmann, “Fourfold nanosystems for quaternary storage devices,” *Journal of Applied Physics*, vol. 110, no. 7, article 073911, 2011.
- [6] W. Zhang and S. Haas, “Phase diagram of magnetization reversal processes in nanorings,” *Physical Review B*, vol. 81, article 064433, 2010.
- [7] R.-H. Wang, J.-S. Jiang, and M. Hu, “Metallic cobalt microcrystals with flowerlike architectures: synthesis, growth mechanism and magnetic properties,” *Materials Research Bulletin*, vol. 44, no. 7, p. 1468, 2009.
- [8] L. Thevenard, H. T. Zeng, D. Petit, and R. P. Cowburn, “Macrospin limit and configurational anisotropy in nanoscale permalloy triangles,” *Journal of Magnetism and Magnetic Materials*, vol. 322, no. 15, pp. 2152–2156, 2010.
- [9] L. Huang, M. A. Schofield, and Y. Zhu, “Control of double-vortex domain configurations in a shape-engineered trilayer nanomagnet system,” *Advanced Materials*, vol. 22, article 492, 2010.
- [10] J. Moritz, G. Vinai, S. Auffret, and B. Dieny, “Two-bit-per-dot patterned media combining in-plane and perpendicular-to-plane magnetized thin films,” *Journal of Applied Physics*, vol. 109, article 083902, 2011.
- [11] R. A. Escobar, S. Castillo-Sepulveda, S. Allende et al., “Towards independent behavior of magnetic slabs,” *IEEE Magnetics Letters*, vol. 8, pp. 1–5, 2017.
- [12] D. Salazar-Aravena, J. L. Palma, and J. Escrig, “Magnetostatic interactions between wire-tube nanostructures,” *Journal of Applied Physics*, vol. 117, no. 19, article 193905, 2015.
- [13] B. Van De Wiele, S. Fin, A. Sarella, P. Vavassori, and D. Bisero, “How finite sample dimensions affect the reversal process of magnetic dot arrays,” *Applied Physics Letters*, vol. 105, no. 16, article 162407, 2014.
- [14] A. Ehrmann and T. Blachowicz, “Interaction between magnetic nanoparticles in clusters,” *AIMS Materials Science*, vol. 4, pp. 383–390, 2017.
- [15] M. J. Donahue and D. G. Porter, “OOMMF Users Guide, Version 1.0,” Interagency Report NISTIR 6376, National Institute of Standards and Technology, Gaithersburg, MD, USA, 1999.
- [16] T. L. Gilbert, “A phenomenological theory of damping in ferromagnetic materials,” *IEEE Transactions on Magnetics*, vol. 40, no. 6, pp. 3443–3449, 2004.
- [17] A. Ehrmann and T. Blachowicz, “Influence of shape and dimension on magnetic anisotropies and magnetization reversal of Py, Fe, and Co nano-objects with four-fold symmetry,” *AIP Advances*, vol. 5, no. 9, article 097109, 2015.
- [18] E. F. Kneller and R. Hawig, “The exchange-spring magnet: a new material principle for permanent magnets,” *IEEE Transactions on Magnetics*, vol. 27, no. 4, pp. 3588–3600, 1991.
- [19] A. Ehrmann, T. Blachowicz, S. Komraus et al., “Magnetic properties of square Py nanowires: irradiation dose and geometry dependence,” *Journal of Applied Physics*, vol. 117, no. 17, Article ID 173903, 2015.
- [20] A. Ehrmann, S. Komraus, T. Blachowicz et al., “Pseudo exchange bias due to rotational anisotropy,” *Journal of Magnetism and Magnetic Materials*, vol. 412, pp. 7–10, 2016.
- [21] T. O. Omotehinwa and S. O. Ramon, “Fibonacci numbers and golden ratio in mathematics and science,” *International Journal of Computer and Information Technology*, vol. 2, no. 4, article 630, 2013.

Research Article

Writing Field Analysis for Shingled Bit-Patterned Magnetic Recording

X. G. Li, Z. J. Liu, A. G. Kang, and X. Y. Xie

College of Physics and Optoelectronics, Taiyuan University of Technology, Taiyuan, China

Correspondence should be addressed to X. G. Li; vcencent1227@hotmail.com

Received 5 April 2017; Revised 7 June 2017; Accepted 18 June 2017; Published 20 July 2017

Academic Editor: K. Devi Chandrasekhar

Copyright © 2017 X. G. Li et al. This is an open access article distributed under the Creative Commons Attribution License, which permits unrestricted use, distribution, and reproduction in any medium, provided the original work is properly cited.

A novel method utilizing response surface methodology (RSM) is proposed for effective analysis of the combined influence of writing head geometry and media properties on writing field performance. The method comprises two main modules: (1) a parametric writing head model based on finite element electromagnetic field analysis and (2) an effective writing field gradient model based on RSM. Using the method proposed, the writing performance of an asymmetrically shielded writing head for shingled magnetic recording on bit-patterned media (SMR-BPM) is analyzed. The results show that the shielding trailing gap and medium coercivity primarily impact the effective writing field (EWF) gradient and that the shielding side gap has a secondary impact. More importantly, the analysis shows a strong interaction effect between the influences of writing head geometry and medium coercivity on the EWF gradient, which indicates the need for inclusive design.

1. Introduction

The development of perpendicular magnetic recording is restricted by the famous trilemma caused by the super-paramagnetic limit: thermal stability, grain size, and writing ability conflict while the areal density is increasing [1]. In recent years, several new methods and techniques have been proposed to manage this problem, such as heat-assisted magnetic recording (HAMR) [2], microwave-assisted magnetic recording (MAMR) [3, 4], shingled magnetic recording (SMR) [5, 6], and bit-patterned media recording (BPM) [7, 8]. In the BPM scheme, the data are stored in patterned magnetic islands instead of grain clusters in conventional continuous media to achieve higher SNR and thermal stability. More recently, it has been demonstrated that the combination of a shingled magnetic recording scheme with bit-patterned media (SMR-BPM) can achieve bit error rates in the range of 10^{-4} at an areal density of 10 Tb/in^2 [9] and 10^{-8} at 4 Tb/in^2 [10]; 14 Tb/in^2 can be achieved by integrating a heat-assisted scheme [11]. However, for SMR-BPM to fully realize its potential, refined designs for the writing head and recording media are of critical importance. Evaluation of the writing head performance involves precise modeling of relatively

complicated geometry features and material properties. And the media characteristics should be considered due to the increasing complexity of the microstructure of the BPM. Research efforts focusing on writing heads [12–15] or BPM [16–18] have been extensive. However, their interdependence and the resulting effects on the writing performance, especially considering the magnetic field distribution around the shingled writing corner, have hardly been addressed, partly due to the complex nature of the problem. In this paper, we use response surface methodology (RSM) [19] to investigate the interaction effect of the head-head and head-media parameters on the EWF gradient for SMR-BPM. The writing head is asymmetrically shielded, similar to those studied in [13, 15]. However, it includes a slot between the trailing shield and the side shield on the shingled writing side, as suggested in [20]. The response surface model of the effective writing field gradient is constructed using the central composite design (CCD) [19], and its sensitivity to the shield design parameters and BPM magnetic properties at the critical location of the writing field contour is investigated. The slot has an apparent influence on the writing field angle distribution around the shingled writing corner. Moreover, the response surface analysis shows a clear interaction effect

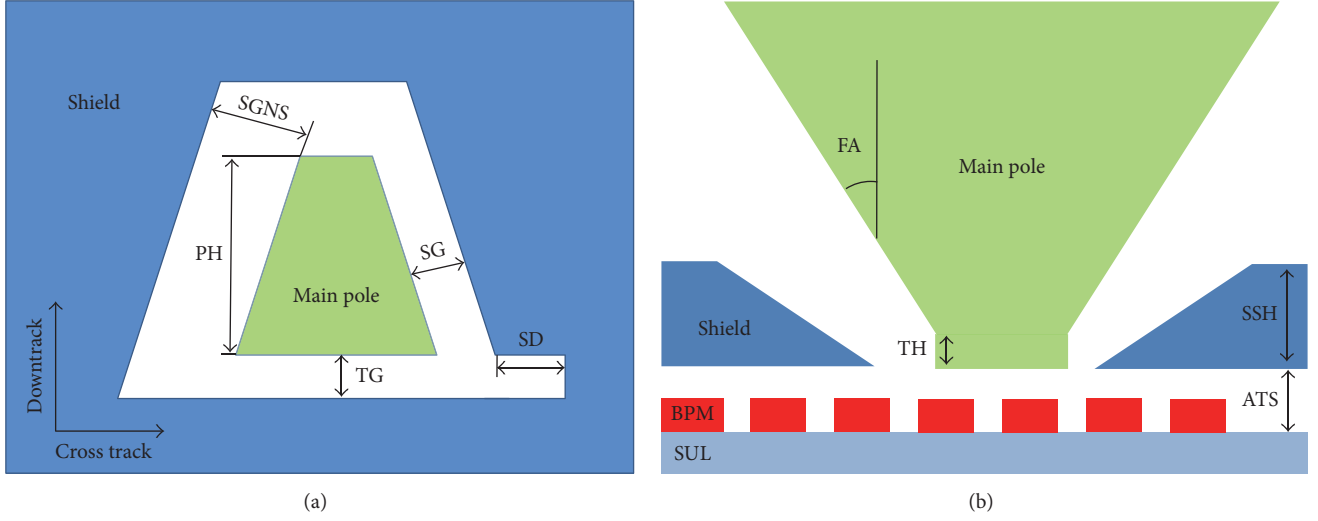


FIGURE 1: Asymmetrically shielded writing head: (a) top view and (b) downtrack view.

between the shield geometric design parameters and the media properties on the EWF gradient, and such effect may have profound influences on the magnetic switching jitter noise and final bit error rate.

2. Modeling Details

2.1. Writing Head Modeling. Utilization of an asymmetrically shielded SMR writing head is believed to help achieve a higher effective writing field and maintain a good field gradient, which is crucial to ultrahigh density recording systems [15]. In this study, an asymmetrically shielded main pole with a slot between the trailing shield and the side shield on the shingled writing side was adopted, and the writing field was analyzed using a finite element Maxwell solver. A schematic view of the investigated writing head structure is shown in Figure 1(a). The shield design parameters considered in the investigation are the trailing gap (TG), side gap on the shingled writing side (SG), and slot depth (SD).

The other parameters were a side gap on the nonshingled writing side (SGNS) of 70 nm, a main pole height (PH) of 75 nm, a throat height (TH) of 5 nm, a main pole flare angle (FA) of 40° , a side shield height (SSH) of 150 nm, and a spacing between the air-bearing surface and the top of the soft-magnetic under layer (ATS) of 25 nm, as shown in Figure 1(b). The saturation magnetization of the main pole was 1910 kA/m, and those of the shield and SUL were 796 kA/m and 955 kA/m, respectively. Notably, the bit-patterned magnetic islands in Figure 1(b) only represent their relative positions and are not included in the finite element model.

The finite element simulation results show that the length of the slot has a clear influence on the writing field distribution near the shingled writing corner. Figure 2 illustrates the change of writing field angle in the media plane (15 nm below the air-bearing surface) when the slot length is varied from

10 nm (Figure 2(a)) to 40 nm (Figure 2(d)) in an increment of 10 nm. The writing field angle around the shingled writing corner increases with increasing slot length.

2.2. Effective Writing Field and Gradient. A major concern for the recording quality in SMR-BPM is that the writing field pertaining to the writing ability tends to spread around the shingled corner of the writing pole [21]. The EWF gradients at this location, particularly where the effective writing field H_{eff} exceeds the coercivity of the magnetic island H_c , are a major factor determining the magnetic switching jitter and the final signal to noise ratio [22]. In this paper, the EWF gradients along the bisector of the main pole base angle (BAB) on the shingle writing side are analyzed using response surface methodology (RSM), as shown in Figure 3.

The magnetization switching behavior of BPM shows clear dependence on the writing field angle, and for magnetic islands with a single phase, the effective writing field can be described by the Stoner-Wohlfarth model [23] as follows:

$$H_{\text{eff}} = H \cdot [(\sin \theta)^{2/3} + (\cos \theta)^{2/3}]^{3/2}, \quad (1)$$

where H is the writing field obtained by the finite element solver mentioned above and θ is the angle between the writing field and the easy axis of the magnetic island, as shown in Figure 2. Notably, exchange coupled composite media with distinct switching field angle dependence [24], which leads to different effective writing field distributions, can also be used to construct the RSM model.

To analyze the influence of design parameters on the writing performance, numerical simulations were devised based on the central composite design (CCD) to construct the second-order response surface model with the EWF gradient as the response target. The model can be expressed as

$$y = \beta_0 + \sum_{i=1}^k \beta_i x_i + \sum_{i=1}^k \beta_{ii} x_i^2 + \sum_{i < j} \beta_{ij} x_i x_j + \varepsilon, \quad (2)$$

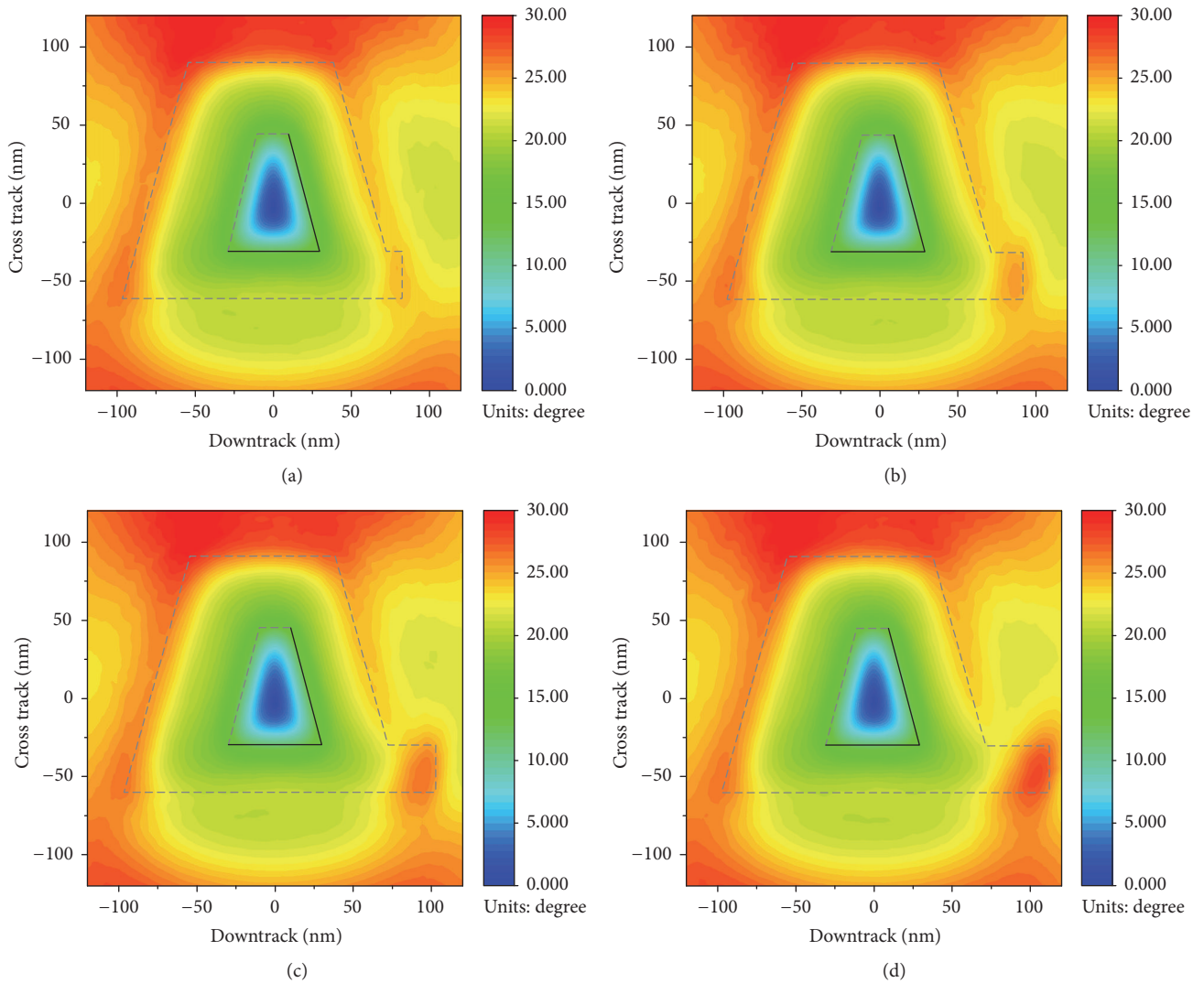


FIGURE 2: Writing field angle distribution in the media plane with SD varying from 10 nm (a) to 40 nm (d). The black solid line indicates the shingled writing corner of the main pole.

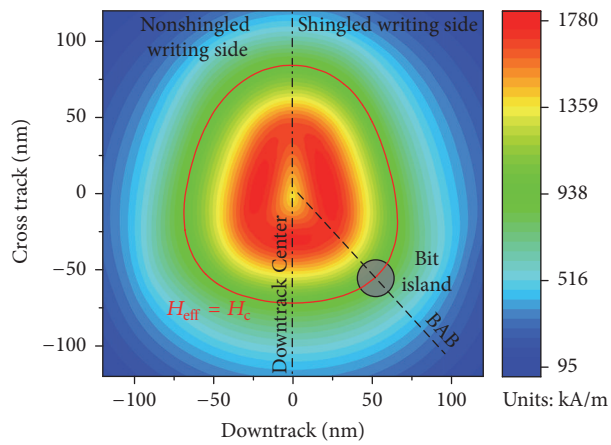


FIGURE 3: Effective writing field distribution in the media plane. The red solid line represents the field contour $H_{eff} = H_c$. The dashed black line is the bisector of the main pole base angle.

where y is the EWF gradient obtained by (1), x_i is the design parameter, ε is the fitting error, k is the number of parameters under investigation, and $\beta_0, \beta_i, \beta_{ii},$ and β_{ij} are the coefficients that need to be solved. A typical CCD includes 2^k factorial runs, $2k$ axial runs, and n_c center runs to identify all the coefficients in the polynomial. In this study, $n_c = 1$ because the pure error can be eliminated in the numerical simulation approach. Equation (2) can be expressed in matrix form as $\mathbf{y} = \mathbf{X}\boldsymbol{\beta} + \boldsymbol{\varepsilon}$, where

$$\mathbf{y} = \begin{bmatrix} y_1 \\ y_2 \\ \vdots \\ y_n \end{bmatrix},$$

$$\mathbf{X} = \begin{bmatrix} 1 & x_{11} \cdots x_{1k} & x_{11}^2 \cdots x_{1k}^2 & x_{11}x_{12} \cdots x_{1,(k-1)}x_{1k} \\ 1 & x_{21} \cdots x_{2k} & x_{21}^2 \cdots x_{2k}^2 & x_{21}x_{22} \cdots x_{2,(k-1)}x_{2k} \\ \vdots & \vdots & \vdots & \vdots \\ 1 & x_{n1} \cdots x_{nk} & x_{n1}^2 \cdots x_{nk}^2 & x_{n1}x_{n2} \cdots x_{n,(k-1)}x_{nk} \end{bmatrix},$$

$$\boldsymbol{\beta} = \begin{bmatrix} \beta_0 \\ \beta_1 \\ \vdots \\ \beta_k \\ \beta_{11} \\ \vdots \\ \beta_{kk} \\ \beta_{12} \\ \vdots \\ \beta_{(k-1)k} \end{bmatrix},$$

$$\boldsymbol{\varepsilon} = \begin{bmatrix} \varepsilon_1 \\ \varepsilon_2 \\ \vdots \\ \varepsilon_n \end{bmatrix},$$

where n is the total simulation runs. The least square estimation of $\boldsymbol{\beta}$ is

$$\boldsymbol{\beta} = (\mathbf{X}'\mathbf{X})^{-1} \mathbf{X}'\mathbf{y}. \quad (4)$$

The full RSM model can be further reduced by dropping insignificant terms, which are identified based on an analysis of variance (ANOVA), as discussed in Section 3.

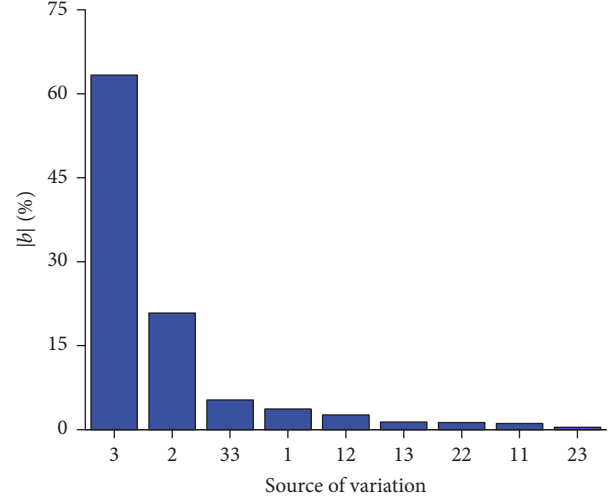


FIGURE 4: Percentagewise absolute value of coefficients indicating main, interaction, and quadratic effects in simulation design I. As shown on the horizontal axis, 1 indicates the main effect of X_1 , 11 indicates the quadratic effect of X_1 , and 12 indicates the interaction effect of X_1 and X_2 .

3. Results and Discussion

3.1. Simulation Design I. We constructed the EWF gradient response surface models related to SD, SG, and TG to investigate the influence of different head design parameters. The coded and natural levels and the EWF gradient responses are given in Table 1. The bit-patterned magnetic island with anisotropy energy density $K_u = 5.83 \times 10^5 \text{ J/m}^3$ and saturation magnetization $M_s = 1 \times 10^6 \text{ A/m}$ was used for angle dependence calculation.

The main effect and two-interaction effect of the design parameters can be evaluated based on the responses of factorial runs (1–8), and the quadratic effect can be evaluated based on the axial and center runs (9–15). Strength of each effect can be indicated by the percentagewise absolute value of the coefficient in RSM model, as shown in Figure 4. The EWF gradient is dominated by the main effect from X_3 , followed by the main effect from X_2 . A minor quadratic effect from X_3 can also be observed, and the remaining effects are almost negligible. Figure 5 shows the corresponding half-normal probability plot [25]. The significant effects are far from the reference line and are labeled on the plot.

The second-order response surface model was fitted by least square estimation. Table 2 shows the corresponding analysis of variance. We used the coefficient of determination to evaluate the fitting quality. For the full model, the adjusted coefficient of determination $R_{\text{adj}}^2 = 0.955$, indicating that the model explains 95.5% of the simulated variation, and the prediction coefficient of determination $R_{\text{pre}}^2 = 0.878$, indicating that the model is expected to explain 87.8% of the variability in new simulations. Notably, because the pure error can be neglected in the simulation approach, the residual is only due to lack of fit.

The individual significance of each term was investigated using a partial F -test, as shown in Table 2. Because we selected

TABLE I: Design details for simulation design I.

Variables	Level			Axial points		Units
	-1	0	1	-1.732	1.732	
SD (X_1)	40	50	60	32.68	67.32	nm
SG (X_2)	40	50	60	32.68	67.32	nm
TG (X_3)	30	40	50	22.68	57.32	nm
Run	X_1		X_2		X_3	Response
1	-1		-1		-1	17301.84
2	1		-1		-1	17126.69
3	-1		1		-1	16379.24
4	1		1		-1	16395.7
5	-1		-1		1	14825.9
6	1		-1		1	14377.82
7	-1		1		1	13916.55
8	1		1		1	13818.39
9	-1.732		0		0	15561.56
10	1.732		0		0	15184.61
11	0		-1.732		0	16109.32
12	0		1.732		0	14832.77
13	0		0		-1.732	17101.63
14	0		0		1.732	13672.73
15	0		0		0	15508.93

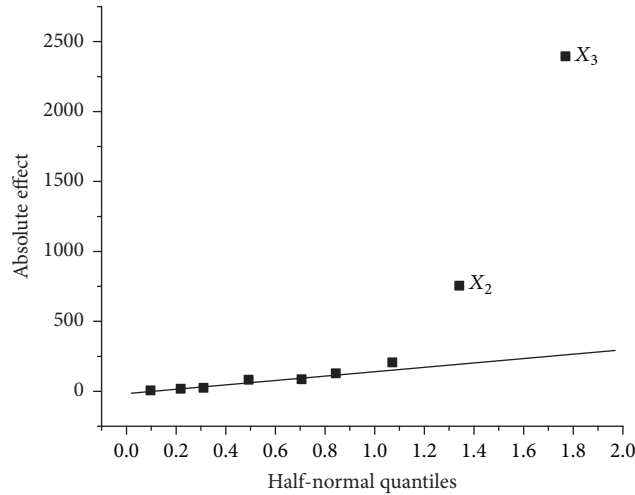


FIGURE 5: The half-normal probability plot for simulation design I.

a significance level of $\alpha = 0.05$, only the first-order terms of X_2 ($P = 0.0028$) and X_3 ($P = 0.000015$) were identified as significant in the model; thus, the reduced model can be expressed as

$$\text{Gradient} = \beta_0 + \beta_2 X_2 + \beta_3 X_3, \quad (5)$$

where $\beta_0 = 15474$, $\beta_2 = -381$, and $\beta_3 = -1157$, with coefficients of determination $R_{\text{adj}}^2 = 0.97$ and $R_{\text{pre}}^2 = 0.802$. The absence of second-order terms and interaction terms indicates a nearly linear influence of these head design parameters on the EWF gradients. Moreover, the negative coefficients for

X_2 and X_3 indicate that a reduction in either SG or TG will improve the field gradient. The EWF gradient is mainly affected by changes in TG, and a relatively small contribution from SG can be observed. Within the design region, optimal design leads to a 20% increase in the EWF gradient, and the maximum of 17012 A/m/nm can be reached at $X_2 = -1$ and $X_3 = -1$, corresponding to SG = 40 nm and TG = 30 nm. However, SD shows almost no influence under the current simulation settings. A possible reason may be that the magnetic island switching field is not affected by SD because it only modulates the field angle distribution underneath.

TABLE 2: ANOVA for simulation design I.

Source of variation	Sum of squares	DF ^a	Mean square	F_0	P value
Regression	20989736.79	9	2332192.98	34.25	0.00058
X_1	131689.24	1	131689.24	1.93	0.223
X_2	2031748.24	1	2031748.24	29.83	0.0028*
X_3	18754095.49	1	18754095.49	275.38	0.000015*
X_1^2	3952.64	1	3952.64	0.058	0.819
X_2^2	391.14	1	391.14	0.006	0.943
X_3^2	2598.20	1	2598.20	0.038	0.853
$X_1 \cdot X_2$	36655.99	1	36655.99	0.54	0.496
$X_1 \cdot X_3$	18772.56	1	18772.56	0.28	0.622
$X_2 \cdot X_3$	4269.09	1	4269.09	0.06	0.812
Residual	340512.37	5	68102.47		
Total	21330249.16	14			

$R^2 = 0.984$; $R_{\text{adj}}^2 = 0.955$; $R_{\text{pre}}^2 = 0.878$; $\alpha = 0.05$. ^aDegrees of freedom. *Significant terms, P value $< \alpha$.

TABLE 3: Design details for simulation design II.

Variables	Level			Axial points		Units
	-1	0	1	-1.732	1.732	
K_u (X_1)	5	5.5	6	4.634	6.366	10^5 J/m^3
SG (X_2)	40	50	60	32.68	67.32	nm
TG (X_3)	30	40	50	22.68	57.32	nm
Run	X_1		X_2		X_3	Response
1	-1		-1		-1	13315.31
2	1		-1		-1	15707.24
3	-1		1		-1	12264.27
4	1		1		-1	15017.47
5	-1		-1		1	12410.05
6	1		-1		1	13078.37
7	-1		1		1	11618.11
8	1		1		1	12580.4
9		-1.732	0		0	12182.75
10		1.732	0		0	14779.12
11		0	-1.732		0	14253.02
12		0	1.732		0	13278.11
13		0	0		-1.732	13612.56
14		0	0		1.732	11415.65
15		0	0		0	13594.28

3.2. *Simulation Design II.* To investigate the relationship between the writing head geometry and bit-patterned media property, another EWF gradient response surface model related to K_u , SG, and TG was constructed, and SD was fixed at 50 nm. If we assume that the diameter of the magnetic island is 10 nm and the height is 12 nm, $K_u > 3.1 \times 10^5 \text{ J/m}^3$ gives $K_u V / k_b T > 70$, which satisfies the thermal stability requirement at room temperature. The simulation design and results are shown in Table 3.

Figure 6 shows the effect strength in simulation design II. Variation of the EWF gradient is a relatively complex process in which the main, interaction, and quadratic effects all contribute considerably.

The ANOVA for simulation design II is shown in Table 4. The significant terms are the first-order terms X_1 ($P = 0.000021$), X_2 ($P = 0.0014$), and X_3 ($P = 0.000032$), second-order term X_3^2 ($P = 0.0056$), and interaction term $X_1 \cdot X_3$ ($P = 0.0015$). Thus, the reduced model is

$$\text{Gradient} = \beta_0 + \beta_1 X_1 + \beta_2 X_2 + \beta_3 X_3 + \beta_{33} X_3^2 + \beta_{13} X_1 X_3, \quad (6)$$

where $\beta_0 = 13617$, $\beta_1 = 805$, $\beta_2 = -337$, $\beta_3 = -744$, $\beta_{33} = -367$, and $\beta_{13} = -439$, with $R_{\text{adj}}^2 = 0.975$ and $R_{\text{pre}}^2 = 0.876$. The positive X_1 coefficient indicates that the increase in K_u improves the EWF gradient. The negative X_2 and

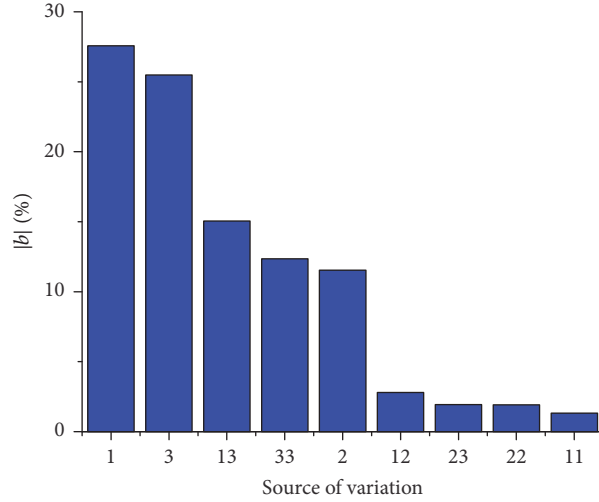


FIGURE 6: Percentagewise absolute value of coefficients indicating main, interaction, and quadratic effects in simulation design II. As shown on the horizontal axis, 1 indicates the main effect of X_1 , 11 indicates the quadratic effect of X_1 , and 12 indicates the interaction effect of X_1 and X_2 .

TABLE 4: ANOVA for simulation design II.

Source of variation	Sum of squares	DF	Mean square	F_0	P value
Regression	21881332.28	9	2431259.14	62.867	0.00013
X_1	9076848.13	1	9076848.13	234.709	0.000021*
X_2	1590855.66	1	1590855.66	41.136	0.0014*
X_3	7759224.55	1	7759224.55	200.638	0.000032*
X_1^2	9577.97	1	9577.97	0.248	0.64
X_2^2	20244.24	1	20244.24	0.523	0.502
X_3^2	834669.40	1	834669.40	21.583	0.0056*
$X_1 \cdot X_2$	53667.39	1	53667.39	1.388	0.292
$X_1 \cdot X_3$	1543974.18	1	1543974.18	39.924	0.0015*
$X_2 \cdot X_3$	25413.23	1	25413.23	0.657	0.454
Residual	193364.26	5	38672.85251		
Total	22074696.54	14			

$R^2 = 0.991$; $R_{adj}^2 = 0.975$; $R_{pre}^2 = 0.933$; $\alpha = 0.05$. * Significant terms, P value $< \alpha$.

X_3 coefficients are in accordance with (5), and a smaller absolute value of the X_3 coefficient indicates that its main effect decreases. More importantly, compared with the model in simulation design I, the model is complicated by two extra terms: (1) the second-order term X_3^2 , which implies that there is a response stationary point for TG within the design region, and (2) the interaction term for X_1 and X_3 , which indicates that the influences from K_u and TG on the EWF gradient are highly correlated.

Figure 7 shows the response surface of the EWF gradient related to SG and TG when K_u was fixed at different levels. The curvature of the surface increases as K_u decreases from $6 \times 10^5 \text{ J/m}^3$ (Figure 7(a)) to $5 \times 10^5 \text{ J/m}^3$ (Figure 7(c)). Moreover, the response maximum with $K_u = 5 \times 10^5 \text{ J/m}^3$ is reached within the design region at SG = 40 nm and TG = 35.2 nm, as shown in Figure 7(c), and a further decrease in TG deteriorates the EWF gradient. This indicates that the optimal TG varies with medium coercivity. Specifically, a medium

with lower K_u prefers a wider TG. One possible reason is the spatial dependence of the writing field gradient. For a writing head design such as that proposed in [13], the optimal field gradient is confined to a small area in the media plane; thus, the medium coercivity must be carefully designed to achieve improved writing performance.

4. Conclusion and Perspectives

In this paper, an EWF gradient model for shingled bit-patterned recording was constructed based on response surface methodology, and the influences from individual and combined parameter variation from the writing head and media were analyzed. Reduction in the trailing gap is more effective than that in the side gap to improve the EWF gradient. The slot between the trailing shield and side shield on the shingled writing side can be used to modulate the field angle distribution but does not show a clear effect on

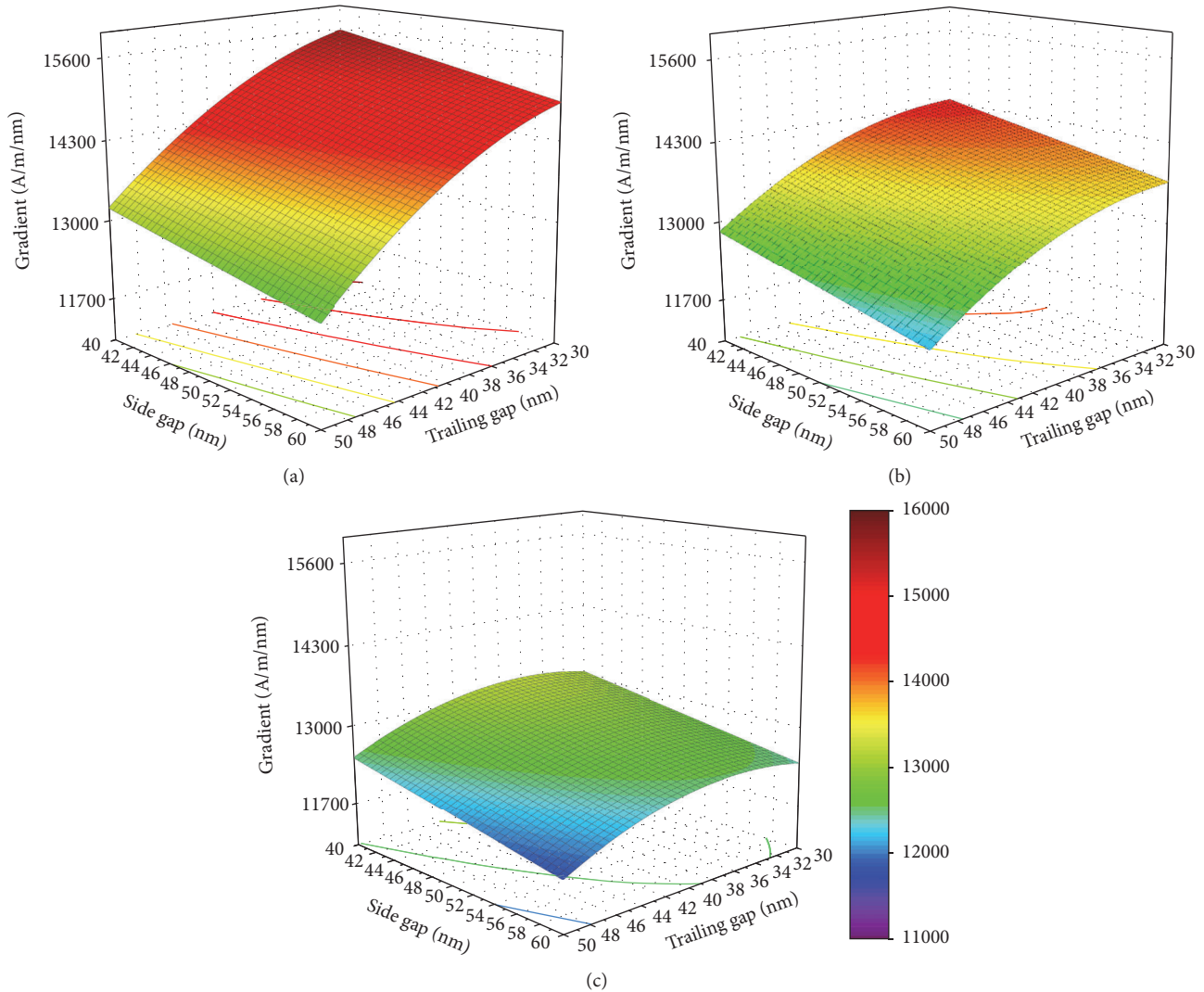


FIGURE 7: The response surface of the EWF gradient with respect to SG and TG with media $K_u = 6 \times 10^5 \text{ J/m}^3$ (a), $5.5 \times 10^5 \text{ J/m}^3$ (b), and $5 \times 10^5 \text{ J/m}^3$ (c).

the EWF gradient. Moreover, the gradient sensitivity to the shield's geometric design parameters is dependent on the coercivity of the medium. The proposed method is useful for evaluation of the bit error rate and SNR of shingled bit-patterned recording systems.

Conflicts of Interest

The authors declare that there are no conflicts of interest regarding the publication of this paper.

References

- [1] K. Z. Gao, O. Heinonen, and Y. Chen, "Read and write processes, and head technology for perpendicular recording," *Journal of Magnetism and Magnetic Materials*, vol. 321, no. 6, pp. 495–507, 2009.
- [2] M. H. Kryder, E. C. Gage, T. W. Mcdaniel et al., "Heat assisted magnetic recording," *Proceedings of the IEEE*, vol. 96, no. 11, pp. 1810–1835, 2008.
- [3] S. Okamoto, N. Kikuchi, M. Furuta, O. Kitakami, and T. Shimatsu, "Microwave assisted magnetic recording technologies and related physics," *Journal of Physics D: Applied Physics*, vol. 48, no. 35, Article ID 353001, 2015.
- [4] M. Zhang, T. Zhou, and Z. Yuan, "Analysis of switchable spin torque oscillator for microwave assisted magnetic recording," *Advances in Condensed Matter Physics*, vol. 2015, Article ID 457456, 6 pages, 2015.
- [5] R. Wood, M. Williams, A. Kavcic, and J. Miles, "The feasibility of magnetic recording at 10 terabits per square inch on conventional media," *IEEE Transactions on Magnetics*, vol. 45, no. 2, pp. 917–921, 2009.
- [6] A. Aghayev, M. Shafaei, and P. Desnoyers, "Skylight - a window on shingled disk operation," *ACM Transactions on Storage*, vol. 11, no. 4, article 16, 2015.

- [7] A. Kikitsu, "Prospects for bit patterned media for high-density magnetic recording," *Journal of Magnetism and Magnetic Materials*, vol. 321, no. 6, pp. 526–530, 2009.
- [8] T. R. Albrecht, H. Arora, V. Ayanoor-Vitikkate et al., "Bit-patterned magnetic recording: theory, media fabrication, and recording performance," *IEEE Transactions on Magnetics*, vol. 51, no. 5, 2015.
- [9] S. Wang, Y. Wang, and R. H. Victora, "Shingled magnetic recording on bit patterned media at 10 Tb/in²," *IEEE Transactions on Magnetics*, vol. 49, no. 7, pp. 3644–3647, 2013.
- [10] A. Kovacs, H. Oezelt, M. E. Schabes, and T. Schrefl, "Numerical optimization of writer and media for bit patterned magnetic recording," *Journal of Applied Physics*, vol. 120, no. 1, Article ID 013902, 2016.
- [11] C. Vogler, C. Abert, F. Bruckner, D. Suess, and D. Praetorius, "Heat-assisted magnetic recording of bit-patterned media beyond 10 Tb/in²," *Applied Physics Letters*, vol. 108, no. 10, Article ID 102406, 2016.
- [12] G. Yu and J. Chen, "Skew effect-induced track erasure of shingled magnetic recording system," *IEEE Transactions on Magnetics*, vol. 50, no. 11, pp. 1–4, 2014.
- [13] R. H. Victora, S. M. Morgan, K. Momsen, E. Cho, and M. F. Erden, "Two-dimensional magnetic recording at 10 Tbits/in²," *IEEE Transactions on Magnetics*, vol. 48, no. 5, pp. 1697–1703, 2012.
- [14] K. Keng Teo, M. R. Elidrissi, K. S. Chan, and Y. Kanai, "Analysis and design of shingled magnetic recording systems," *Journal of Applied Physics*, vol. 111, no. 7, Article ID 07B716, 2012.
- [15] Y. Kanai, Y. Jinbo, T. Tsukamoto, S. J. Greaves, K. Yoshida, and H. Muraoka, "Finite-element and micromagnetic modeling of write heads for shingled recording," *IEEE Transactions on Magnetics*, vol. 46, no. 3, pp. 715–721, 2010.
- [16] X. M. Yang, S. Xiao, Y. Hsu, M. Feldbaum, K. Lee, and D. Kuo, "Directed self-assembly of block copolymer for bit patterned media with areal density of 1.5 Teradot/Inch² and beyond," *Journal of Nanomaterials*, vol. 2013, Article ID 615896, 17 pages, 2013.
- [17] W. Tipcharoen, A. Kaewrawang, and A. Siritaratiwat, "Design and micromagnetic simulation of Fe/L1₀-FePt/Fe trilayer for exchange coupled composite bit patterned media at ultrahigh areal density," *Advances in Materials Science and Engineering*, vol. 2015, Article ID 504628, 5 pages, 2015.
- [18] H. Oezelt, A. Kovacs, P. Wohlhüter et al., "Micromagnetic simulation of exchange coupled ferri-/ferromagnetic composite in bit patterned media," *Journal of Applied Physics*, vol. 117, no. 17, Article ID 17E501, 2015.
- [19] R. H. Myers and D. C. Montgomery, *Response Surface Methodology: Process and Product Optimization Using Designed Experiments*, John Wiley & Sons Inc., Hoboken, NJ, USA, 2009.
- [20] T. Kagami, "An areal-density capability study of SMR by using improved write and read heads," in *Proceedings of the Intermag*, FA-01, April 2011.
- [21] M. Salo, T. Olson, R. Galbraith et al., "The structure of shingled magnetic recording tracks," *IEEE Transactions on Magnetics*, vol. 50, no. 3, pp. 18–23, 2014.
- [22] K. Miura, E. Yamamoto, H. Aoi, and H. Muraoka, "Skew angle effect in shingled writing magnetic recording," *Physics Procedia*, vol. 16, pp. 2–7, 2011.
- [23] E. C. Stoner and E. P. Wohlfarth, "A mechanism of magnetic hysteresis in heterogeneous alloys," *Philosophical Transactions of the Royal Society A: Mathematical, Physical and Engineering Sciences*, vol. 240, no. 826, pp. 599–642, 1948.
- [24] H. Oezelt, A. Kovacs, J. Fischbacher et al., "Switching field distribution of exchange coupled ferri-/ferromagnetic composite bit patterned media," *Journal of Applied Physics*, vol. 120, no. 9, Article ID 093904, 2016.
- [25] "Half-normal probability plot, NIST/SEMATECH e-handbook of statistical methods," 2012, <http://www.itl.nist.gov/div898/hand-book/>.

Research Article

Development of Stabilized Magnetite Nanoparticles for Medical Applications

Ioana Lavinia Ardelean, Luric Bogdan Nicolae Stoencea, Denisa Ficai, Anton Ficai, Roxana Trusca, Bogdan Stefan Vasile, Gheorghe Nechifor, and Ecaterina Andronescu

Faculty of Applied Chemistry and Material Science, Politehnica University of Bucharest, 1-7 Gh Polizu Street, 011061 Bucharest, Romania

Correspondence should be addressed to Denisa Ficai; denisaficai@yahoo.ro

Received 12 March 2017; Accepted 27 April 2017; Published 11 June 2017

Academic Editor: Vidyadhar Singh

Copyright © 2017 Ioana Lavinia Ardelean et al. This is an open access article distributed under the Creative Commons Attribution License, which permits unrestricted use, distribution, and reproduction in any medium, provided the original work is properly cited.

We report a facile method to synthesize magnetite nanoparticles with mesoporous structure by coprecipitation method using different stabilizing agents like salicylic acid, glutamic acid, and trichloroacetic acid. The stabilizing agents were used to prevent the aggregation of the magnetite nanocrystals and to obtain stable nanostructures even in the biological environment. The structure and morphology of magnetic nanocrystals were determined using X-ray diffraction (XRD), Fourier Transform Infrared (FTIR) spectroscopy, Brunauer-Emmett-Teller (BET) analysis, infrared (IR) spectra, scanning and transmission electron microscopy (SEM and TEM), high-resolution transmission electron microscopy (HRTEM), and selected area electron diffraction (SAED). The results reveal important differences between these magnetic nanoparticles (MNPs), which are mainly attributed to the stabilizing agents. The smallest nanoparticles were obtained in the presence of trichloroacetate ions. The mechanism of formation of these suprastructures is strongly correlated with the end functional groups of the stabilizing agent. Thus, the obtained nanoparticles are potential candidates for contrast agents as well as targeted carrier for specific diseases, especially cancer.

1. Introduction

Synthesis and characterization of porous materials have attracted considerable attention in recent years due to their industrial and biomedical applications: heavy metals removal, sensors, catalysis, magnetic recording and separation, photocatalysis, pigments, ferrofluids, magnetic resonance imaging, hyperthermia drug delivery, and so on [1–6]. Mesoporous iron oxides such as Fe_3O_4 and $\gamma\text{-Fe}_2\text{O}_3$ and CoFe_2O_4 are successfully used in the field of magnetic fluids, catalysis, biotechnology/biomedicine, magnetic resonance imaging, and magnetic recording devices because of their paramagnetism, biocompatibility, and safety [7–11]. Owing to their large surface area and well-defined pore structure and size, the lack of toxicity, and the possibility of targeted accumulation in the desired tissue, mesoporous Fe_3O_4 nanospheres are extensively used as targeted drug delivery systems [12].

Various techniques have been developed to synthesize some important transition metal oxides (such as Fe_3O_4 and

CoFe_2O_4) with various interior porous architecture (simple hollow spheres, core-shell and mesoporous structures [13–15]) using coprecipitation method [16], pyrolysis, hydrothermal reaction [17], microwave-assisted synthesis [18], and the thermal decomposition of organometallic compounds [19–22].

Liu et al. [23] prepared Palladium- (Pd-) loaded amino-group functionalized mesoporous Fe_3O_4 nanoparticles ($\text{Pd}@Fe_3O_4$) by a simple solvothermal method using ethanol as solvent. They show that the $\text{Pd}@Fe_3O_4$ modified the glassy carbon electrode (GCE) which then exhibited excellent electrochemical catalytic activities towards dopamine (DA) due to the synergetic effect between Pd and Fe_3O_4 .

Kumari et al. [24] synthesized magnetite nanospheres with hollow interiors using a simple, one-pot, and template-free solvothermal method with ferric chloride as the iron precursor, for the purpose of using this mesoporous nanosphere to remove heavy metals from waste water. The Langmuir adsorption capacities of the magnetic nanospheres were 9 and 19 mg/g for Cr^{6+} and Pb^{2+} , respectively.

Xia et al. [25] synthesized high-quality mesoporous Fe_3O_4 nanocages (MFONs) with a mesoporous structure and highly uniform dispersion by a facile complex-coprecipitation method at 100°C with addition of triethanolamine and ethylene glycol. They show that when used as an anode material for rechargeable lithium-ion batteries, MFONs anode presents high specific capacities and excellent cycling performance at high and low current rates thanks to the unique mesoporous cage-like structure and high specific surface area ($133\text{ m}^2/\text{g}$), which may offer large electrode/electrolyte contact area for the electron conduction and Li^+ storage.

The surface modification of the magnetic materials is essential for most of the chemical and biological applications and the performances of these materials can be designed by proper surface modification. Among the properties of interest, biocompatibility, biostability, and internalization are especially studied in the literature. It is well known that magnetite dispersibility and chemical stability in biological media are improved by functionalization with PEG (polyethylene glycol), dextran, albumin, chitosan, PVA (polyvinyl alcohol), PLGA (poly(lactic-co-glycolic acid)), and so on [26], but only a very limited number of studies present the functionalization of these nanoparticles with bifunctional small molecules like aminoacids, hydroxyacids, or haloacids [27, 28]. These bifunctional stabilizing small agents can be essential in allowing a better internalization of the nanoparticles inside the cells (especially when using aminoacids as functionalization agents), but they do not improve the dispersibility (because dispersability is ensured by the existence of highly charged groups such as citrate where three carboxylic groups are available for repulsive purposes). At this moment, a special attention is paid to folic acid (vitamin 12), a specific aminoacid, which proved to have a good internalization capacity for the magnetic nanoparticles, and it even allows a targeted delivery inside the tumoral cells [29–32].

The aminoacid or hydroxyacid based coating over the magnetic core offers the premises of high biocompatibility and an improvement in the capacity of internalization of these nanoparticles. In this study we report a facile method to synthesize magnetite nanoparticles with mesoporous structure by coprecipitation method using different stabilizing agents: salicylic acid, glutamic acid, and trichloroacetic acid. The very different structure and potential biological activity of the three stabilizing agents is important in designing new magnetic agents with desired properties. After the coating of the magnetic core, glutamic acid still has a free carboxyl group while salicylic acid has a hydroxyl group, each group being able to further bind molecules onto the surface [33]. Glutamic acid also acts as a powerful dispersing agent (like citrate) because of the net negative surface charge of the resulting nanostructures. The role of different stabilizing agents from the point of view of crystallinity, pore diameter, and surface area was analyzed. In order to determine the structure and morphology, the as-synthesized mesoporous Fe_3O_4 was characterized by powder X-ray diffraction (XRD), Fourier Transform Infrared (FTIR) spectroscopy, Brunauer-Emmett-Teller (BET), infrared (IR) spectra, scanning and

transmission electron microscopy (SEM and TEM), high-resolution transmission electron microscopy (HRTEM), and selected area electron diffraction (SAED).

2. Experimental Details

2.1. Materials and Methods. The main precursors used for the preparation of mesoporous magnetite are iron (III) chloride (FeCl_3) (Sigma-Aldrich), ammonium iron (II) sulfate hexahydrate ($\text{Fe}(\text{NH}_4)_2(\text{SO}_4)_2 \cdot 6\text{H}_2\text{O}$) (Silal Trading), sodium hydroxide (NaOH) (Silal Trading), salicylic acid ($\text{C}_6\text{H}_7\text{O}_3$) (Chimactiv), glutamic acid (Sigma-Aldrich), trichloroacetic acid (Carlo Erba RP ACS), and distilled water.

Mesoporous magnetite nanoparticles were prepared by precipitation method [34] with different stabilizing agents: salicylic acid, glutamic acid, and trichloroacetic acid. The precipitation bath was obtained as follows. First of all, the sodium hydroxide solution (10 g $\text{NaOH}/250\text{ mL}$ solution) was obtained and then mixed with further 2.5 g of the stabilizing agent, under vigorous mechanical stirring at room temperature. The pH of the precipitation bath was set at 10–11 with hydroxide solution. The precursors solution (8.4520 g $\text{Fe}(\text{NH}_4)_2(\text{SO}_4)_2 \cdot 6\text{H}_2\text{O}$ and 6.9920 g FeCl_3 in 100 ml distilled water) was sprayed into the obtained precipitation bath, under continuous mechanical stirring. The spraying rate was set at about 2–3 mL/min. After precipitation, the mixture was placed in the ultrasonic bath for 30 minutes; then the mesoporous magnetite was filtered and washed, whenever needed, with distilled water until neutral pH and chloride-free filtrate were obtained. Finally, the synthesized mesoporous magnetite was dried in a vacuum oven at a temperature of 60°C (Figure 1) [34]. Based on the above presented procedure, magnetite (Fe_3O_4), magnetite with salicylic acid ($\text{Fe}_3\text{O}_4@\text{SAL}$), magnetite with glutamic acid ($\text{Fe}_3\text{O}_4@\text{GLU}$), and magnetite with trichloroacetic acid ($\text{Fe}_3\text{O}_4@\text{TCA}$) have been obtained.

The mesoporous magnetite nanoparticles were characterized by XRD, FTIR, SEM, TEM, and BET.

IR spectroscopy was performed on a Nicolet iS 50 FTIR spectrometer equipped with a broad range DTGS detector providing high-sensitivity infrared information from 4000 cm^{-1} to 100 cm^{-1} and an integral diamond ATR unit. The system is configured with the built-in iS50 ATR module and an iS50 ABX Automated Beamsplitter Exchanger. The spectra were recorded in ATR mode over the wave number range of $400\text{--}4000\text{ cm}^{-1}$, with a resolution of 4 cm^{-1} coadding 64 spectra for improving the quality of the spectra. For a better identification of the peaks, the obtained spectra were resolved using a Gaussian-Lorentzian peak resolve procedure assuming a linear baseline.

Morphological information was obtained by scanning electron microscopy of the gold-coated specimens. The analysis has been performed using a QUANTA INSPECT F SEM device equipped with a field emission gun (FEG) with a resolution of 1.2 nm and with an X-ray energy dispersive spectrometer (EDS).

X-ray diffraction analysis was carried out on a Panalytical X'Pert Pro MPD equipment, with a CuK_α radiation, over a scan range of 2θ of $10\text{--}90^\circ$.

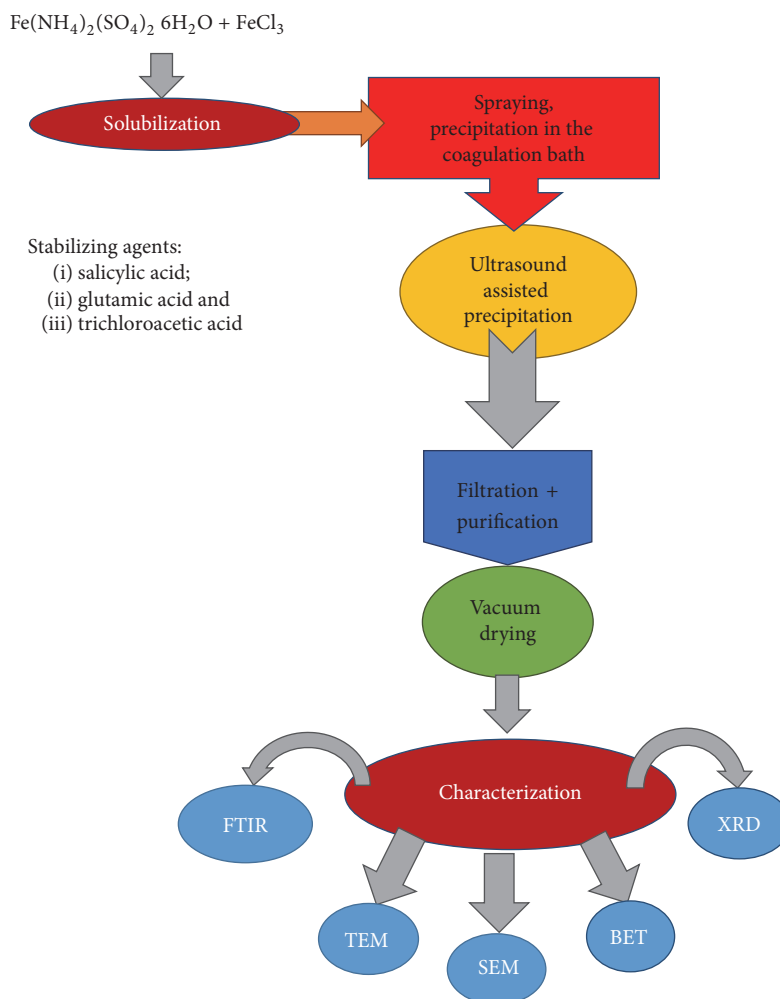


FIGURE 1: Preparation flowchart of magnetic nanoparticles.

TEM analyses were performed on a Tecnai G2 F30 S-TWIN high-resolution transmission electron microscope (HR-TEM) equipped with energy dispersive spectroscopy (EDS) as well as a selected area electron diffraction detector (SAED). The microscope was operated in transmission mode at 300 kV; TEM point resolution was 2 Å and line resolution was 1 Å.

The Brunauer-Emmett-Teller (BET) analysis was performed on a Micrometrics Gemini V surface area and pore size analyzer.

3. Results and Discussion

3.1. Complex Thermal Analysis. The complex thermal analysis (Figure 2) was recorded in order to quantify the amount of stabilizing agent retained on the magnetic nanostructures. It can be seen that, among the three stabilizing agents, the lowest affinity to the magnetic core belongs to GLU (0.54%) and the highest belongs to TCA (7.28%) while SAL exhibits intermediary affinity (2.50%). Based on the TG data, the strong flattening of the XRD peaks of the Fe_3O_4 @TCA can be explained because of the high content of the stabilizing agent

(7.28%) while in the case of Fe_3O_4 @SAL (containing 2.50% stabilizing agent) the flattening is less significant (plane 422 disappears while plane 220 is strongly flattened). In the case of GLU stabilized magnetic nanostructures, the peaks are even stronger which can mean that the crystallization process was even better compared with the pure Fe_3O_4 sample. All these masses were determined at 600°C.

The differential thermal analysis reveals a stabilization effect of the salicylic acid, the most intense exothermic peak of pure magnetite (538.7 being shifted to 549.5°C) while in both the other cases this peak is shifted to lower temperature (498.0 and 525.2°C).

3.2. X-Ray Diffraction. X-ray diffraction was used in order to establish the formation of magnetite as a pure phase. The XRD patterns (Figure 3) of the synthesized mesoporous MNPs present only the characteristic peaks of magnetite [34] even if the crystallinity and the crystallite size depend on the used stabilizing agent. The main crystallization planes of inverse spinel magnetic crystals can be clearly identified by XRD ((111), (9220), (311), (400), (422), (511), and (440)), their relative intensity indicating a nonpreferential crystallization

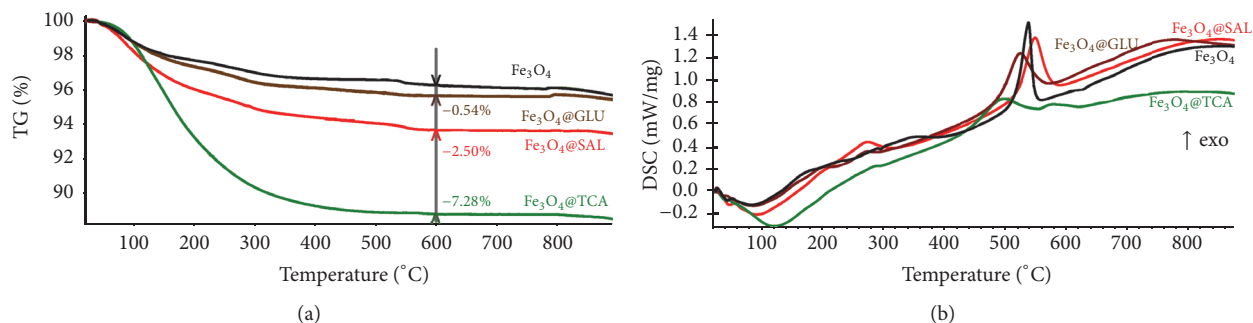


FIGURE 2: Complex thermal analysis of Fe_3O_4 , $\text{Fe}_3\text{O}_4@GLU$, $\text{Fe}_3\text{O}_4@SAL$, and $\text{Fe}_3\text{O}_4@TCA$: (a) thermogravimetric analysis and (b) differential thermal analysis.

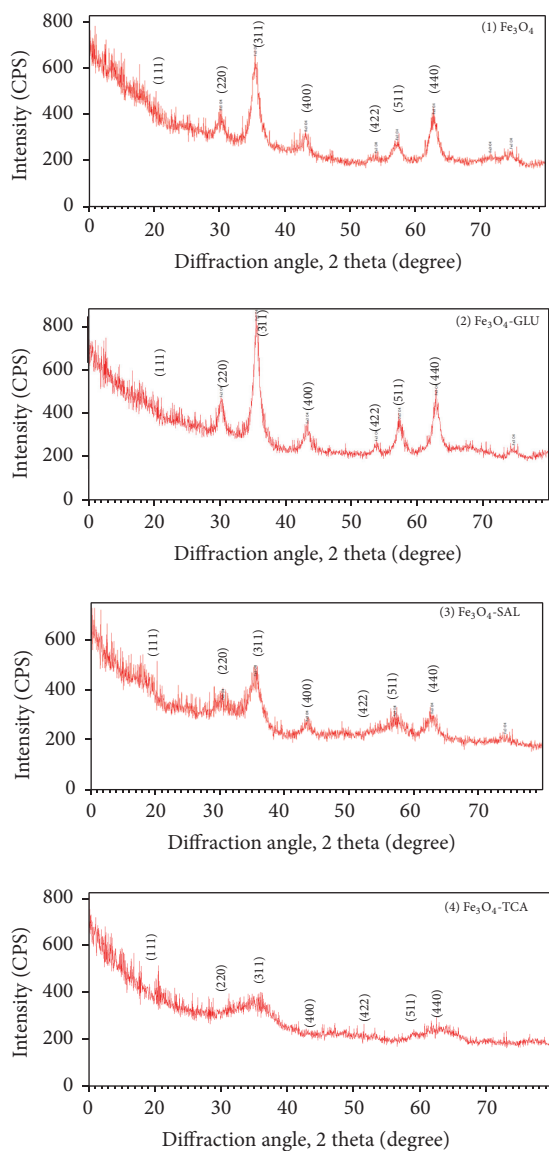


FIGURE 3: XRD patterns of the synthesized nanoparticles: (1) Fe_3O_4 , (2) $\text{Fe}_3\text{O}_4@GLU$, (3) $\text{Fe}_3\text{O}_4@SAL$, and (4) $\text{Fe}_3\text{O}_4@TCA$.

according to the literature [35] and ASTM 0075-1609. The average crystallite size is calculated using the Debye-Scherrer equation: $D = k\lambda/\beta \cos \theta$, where $k = 0.95$ is Scherrer's constant, λ is the X-ray wavelength, β is the full width at half-maximum, and θ is the Bragg diffraction angle. Based on this equation, the crystallite size (using the reflection plane (311), which can be measured for all the samples) was found to be 8.8, 11.3, 6.1, and 2.5 nm (Fe_3O_4 , $\text{Fe}_3\text{O}_4@GLU$, $\text{Fe}_3\text{O}_4@SAL$, and $\text{Fe}_3\text{O}_4@TCA$, resp.). The XRD patterns of Fe_3O_4 and $\text{Fe}_3\text{O}_4@GLU$ are similar, with almost the same shape and comparative peaks intensity which means that comparative crystallinity and crystallite size are obtained. In the case of $\text{Fe}_3\text{O}_4@SAL$, the characteristic diffraction peaks decrease as intensity, while, in the case of $\text{Fe}_3\text{O}_4@TCA$, even the main peak of magnetite could not be clearly identified.

3.3. FTIR. The FTIR data reveal some differences between the spectra of the samples, especially compared with pure magnetite (Figure 4). Based on the literature data [35], the main bands of magnetite corresponding to the vibration of $\text{Fe}^{3+}/\text{Fe}^{2+}-\text{O}^{2-}$ in tetrahedral and octahedral sites in the magnetite appear at ~ 400 and 568 cm^{-1} . It can be seen that both $\text{Fe}_3\text{O}_4@SAL$ and $\text{Fe}_3\text{O}_4@GLU$ exhibit high similitude with the pure magnetite, most probably because of the low content of the stabilizing agent (0.54 and 2.50 for GLU and SAL, resp.). In the case of the sample obtained in the presence of trichloroacetate, the strong band from $\sim 540 \text{ cm}^{-1}$ is only visible as a shoulder. The explanation is related to the presence of a high amount of trichloroacetate (7.28% based on the thermogravimetric data), as stabilizing agent covering the magnetite core. The presence of the trichloroacetate can be clearly identified after deconvolution between 400 and 1700 cm^{-1} , based on its main bands centered close to that of sodium trichloroacetate (based on the HR Aldrich FTIR Collection Edition II library): 685 (new peak), 710 (new peak), 723, 738 (new peak), and 845 cm^{-1} (Figure 4, insert). The shifting of these peaks is a proof of the strong interaction between magnetite core and trichloroacetate shell, along with the strong decrease of the strong peak of magnetite

TABLE 1: BET data of the synthesized MNPs samples.

Sample code	Samples name	Specific surface area S_{BET} (m^2/g)	Average pore size D_{BET} (nm)
Fe_3O_4 reference*	Fe_3O_4	156.0278 m^2/g	5.7466 nm
Fe_3O_4 @citrate*	Fe_3O_4 @citrate	257.15 m^2/g	2.8075 nm
Fe_3O_4 @SAL	Fe_3O_4 @salicylic acid	204.7198 m^2/g	5.2712 nm
Fe_3O_4 @GLU	Fe_3O_4 @glutamic acid	129.5527 m^2/g	8.3597 nm
Fe_3O_4 @TCA	Fe_3O_4 @trichloroacetic acid	287.7533 m^2/g	3.4475 nm

* Data published in [34].

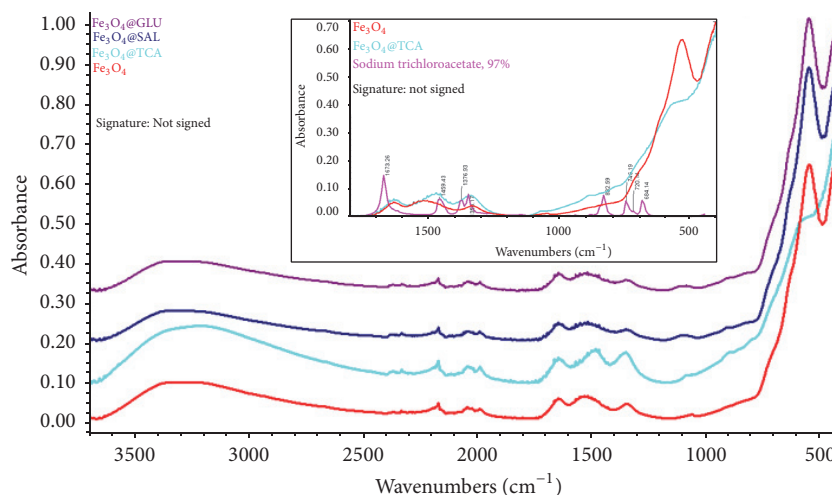


FIGURE 4: FTIR spectra of the magnetic samples: Fe_3O_4 , Fe_3O_4 @TCA, Fe_3O_4 @SAL, and Fe_3O_4 @GLU; insert represents an overlay of Fe_3O_4 , Fe_3O_4 @TCA, and sodium trichloroacetate, over the region of $400\text{--}1800\text{ cm}^{-1}$.

from $\sim 532\text{ cm}^{-1}$ and the strong decrease of the Roentgen interferences characteristic for magnetite.

The most representative SEM images recorded at 50 (100) kx and 400 kx are presented in Figure 5. At high magnification, the nanostructured nature of these materials can be visualized. The morphology of Fe_3O_4 @GLU and Fe_3O_4 @SAL is similar to that of bare Fe_3O_4 while the Fe_3O_4 @TCA exhibits different morphology, perhaps due to the increasing content of the organic stabilizing agent and smaller particle size. These differences will be further resolved by (HR)TEM.

The TEM images were used to determine the size and morphology of the synthesized MNPs (Figure 6). The TEM images of the samples reveal some particularities. First of all, in all cases, the fine particles are strongly agglomerated because of the attractive forces between the magnetic nanoparticles. Based on the HRTEM images, the size and shapes of the nanoparticles can be evaluated. In the case of bare magnetite, spherical nanoparticles can be identified, the diameter of these nanoparticles being between 3 and 20 nm. In the case of Fe_3O_4 @GLU, two kinds of nanoparticles can be identified. The spherical nanoparticles have similar characteristics with those of pure magnetite but some rod-like nanoparticles can be also identified, their length reaching up to 50 nm, while the diameter is less than 10 nm. Based on the crystallite size determined by Debye-Scherrer equation, a good consistency between the TEM and XRD data can be concluded if considering also the capping effect induced

by the stabilizing agent [36] except for the case of the rod-like structures identified in Fe_3O_4 @GLU where these particles contain tens of crystallites. In the case of Fe_3O_4 @SAL and Fe_3O_4 @TCA, the size of the spherical nanoparticles is decreasing dramatically compared with the previous MNPs; the use of TCA as stabilizing agent induces the most important size reduction and, thus, has the best ability to stabilize the magnetite and can be correlated with the higher amount of stabilizing agent linked onto the magnetite core (7.28%). This conclusion is also supported by the SAED patterns of the four MNPs. In all cases, the selected area electron diffraction shapes confirm the formation of very fine nanoparticles, especially when TCA is used, the polycrystalline structure of the cubic spinel magnetic crystals being clearly highlighted, being in good accordance with the XRD data [37].

BET analysis was used to characterize the obtained mesoporous MNPs from the point of view of surface area. From the point of view of the average pore size and specific surface area, the stabilizing agents play an important role. According to Table 1, the pure magnetite has a specific surface area of $\sim 156\text{ m}^2/\text{g}$ and an average pore size of 5.75 nm while the use of salicylic acid leads to an increased specific surface area and practically no change of the pore size; the use of glutamic acid leads to an important decrease of the specific surface area and an increase of the pore size while the use of trichloroacetic acid leads to a strong increase of the specific surface area (almost two times higher specific surface area

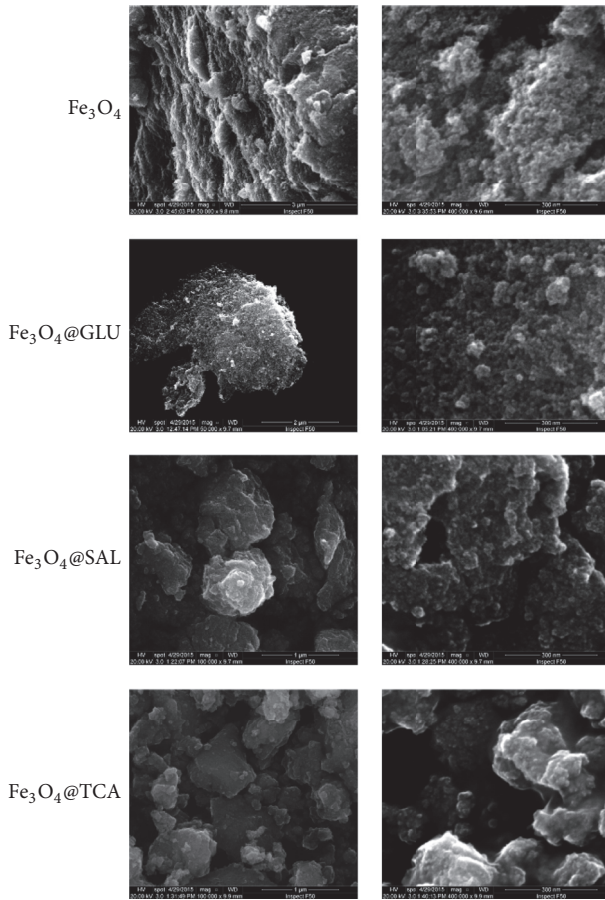


FIGURE 5: SEM images of the stabilized and nonstabilized magnetic nanoparticles obtained by coprecipitation.

compared with reference magnetite) and a corresponding decrease of the average pore size, down to 3.45 nm. The different behaviors are explained based on the different chemical structure of the three stabilizing agents and different amount of stabilizing agent adsorption onto the magnetic crystals. The strongest stabilization effect is ensured by TCA which conducts to a higher specific surface area being in good agreement with the TEM images (especially visible at low magnification, the first image of each sample). Compared with the well-established Fe₃O₄@citrate superparamagnetic iron oxide nanoparticles, it can be concluded that TCA can ensure even better stabilization effect and the specific surface area can be improved by ~10% [34].

The mechanisms of the formation of the Fe₃O₄@stabilizing agent is strongly dependent on some factors, the most important being the nature of the stabilizing agent and its concentration and pH. When the stabilizing agent is TCA, the single possibility of self-assembling is presented in Figure 7(a), carboxylate group being absorbed onto the magnetite core surface, while the trichloromethyl groups are oriented to the outer region of the core@shell structure. Between these core@shell individual structures hydrophobic interactions occur, thus leading to agglomerates. In the case of glutamic acid, as well as salicylic acid, the formation

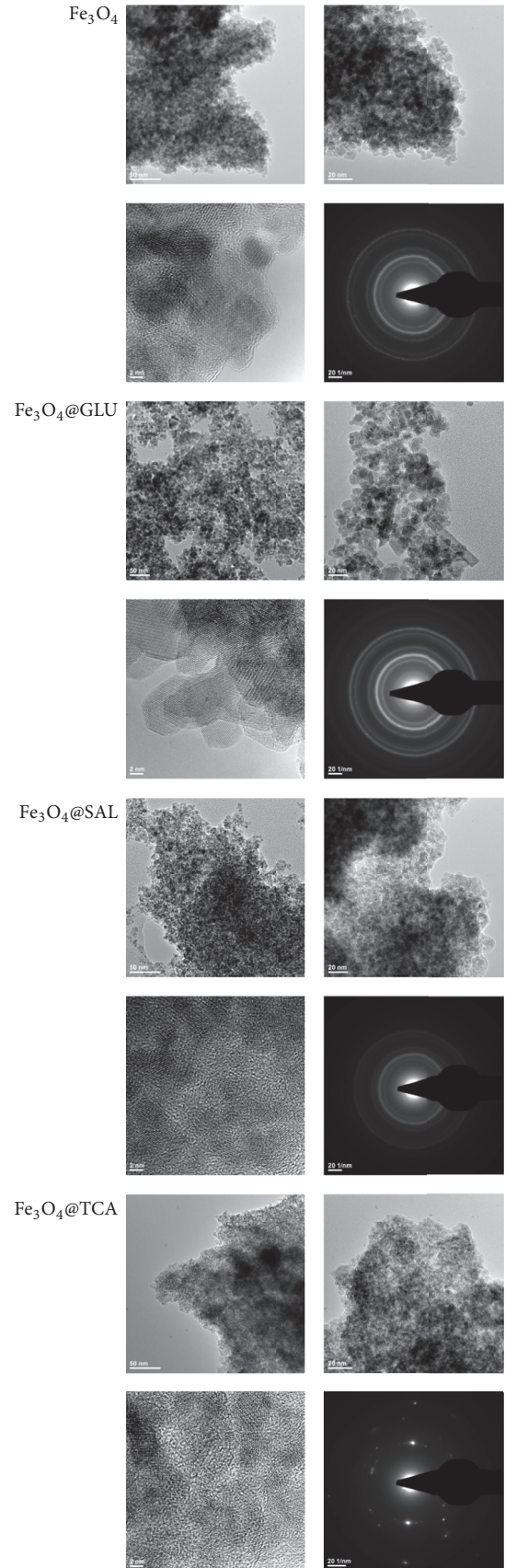


FIGURE 6: TEM, HRTEM, and SAED patterns of the bare magnetite and stabilized MNPs.

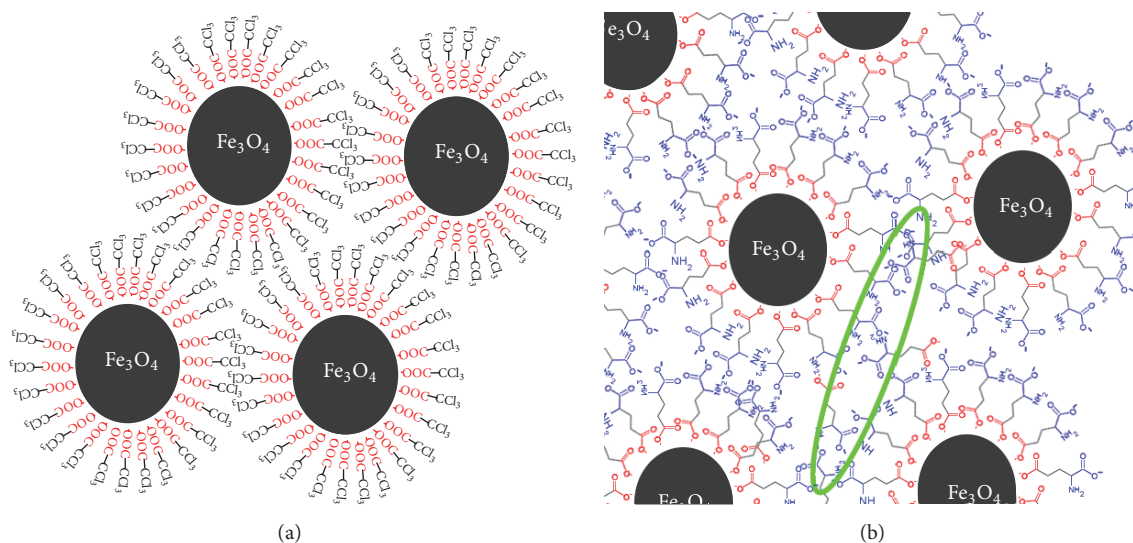


FIGURE 7: Magnetite based suprastructures induced by stabilizing agents.

of Fe_3O_4 @GLU and Fe_3O_4 @SAL leads to the existence of multiple functional groups of the stabilizing agent, therefore allowing additional interactions between these moieties. So, along with the formation of the similar core@shell structures and agglomerates (assuming that COOH is in its anionic form and ammonium in its zero-valent form, namely, NH_2), as presented in the case of TCA, the additional interactions between different groups of the stabilizing agents also allow new stabilizing agent-stabilizing agent interactions (Figure 7(b), region delimited by green ellipse), leading to an increasing size of the core@shell structures and consequently lower specific surface area compared with Fe_3O_4 @TCA. Even double layered shells can be imagined partly because the amino groups are in their cationic form and also water molecules can facilitate these interactions.

The as-obtained core@shell nanostructures can be imagined as potential carriers of a wide variety of biological active agents; the loading efficiency and the delivery behavior are controlled and induced due to the shell characteristics. The active agents can be attached to the shell, adsorbed into the magnetic core, or even distributed between the two components of the core@shell structures. These active agents will interact with the shell via hydrophobic or hydrophilic interactions. The use of salicylic acid as capping agent will allow the formation of strong hydrogen bonds with these nanostructures, while in the case of glutamic acid hydrogen bonds as well as electrostatic interactions will be possible, depending on the pH. In both cases covalent bonding of the active agent is possible via the reactive phenolic and carboxylic groups. In the case of trichloroacetic acid, especially hydrophobic and dipole based interactions will appear, but also more complex mechanisms of bonding are possible involving partial/full hydrolysis of the trichloro groups followed by covalent bonding. The main interactions between

the shell and the biological active agents are presented in Figure 8. The overall properties of the drug delivery systems are strongly dependent on many factors including the loading procedures, not only the nature and proportions of the components.

4. Conclusion

Three new magnetic nanoparticles were obtained starting from magnetite precursors and adequate stabilizing agents (salicylic acid, glutamic acid, and trichloroacetic acid) by spraying the magnetite precursors into the basic stabilizing agent solution. The results reveal important difference between these MNPs, these differences being induced by the used stabilizing agent. The smallest nanoparticles were obtained in the presence of trichloroacetate ions. The mechanism of formation of these suprastructures is strongly correlated with the end functional groups of the stabilizing agent. Comparing the glutamate and trichloroacetate, from both size and free functional groups, significant differences can be identified. In fact, the entire molecule excepting the carboxylate groups (highlighted with red) ensures the interaction of the stabilizing agent with the magnetic core as represented in Figure 7. It can be concluded that the agglomeration of the stabilized core@shell suprastructure is different because of the very different affinity of these end groups. In the case of glutamic acid, the ammonium and carboxylate groups can further interact and thus lead to larger particles and smaller core@shell structure as highlighted by TEM and HRTEM. The as-obtained nanoparticles are potential contrast agents as well as magnetic carriers of specific drugs for cancer diagnosis and treatments. Further works will be conducted in order to study the biocompatibility, cell internalization, and ability for targeted transport and delivery of various biological active agents including cytostatic drugs.

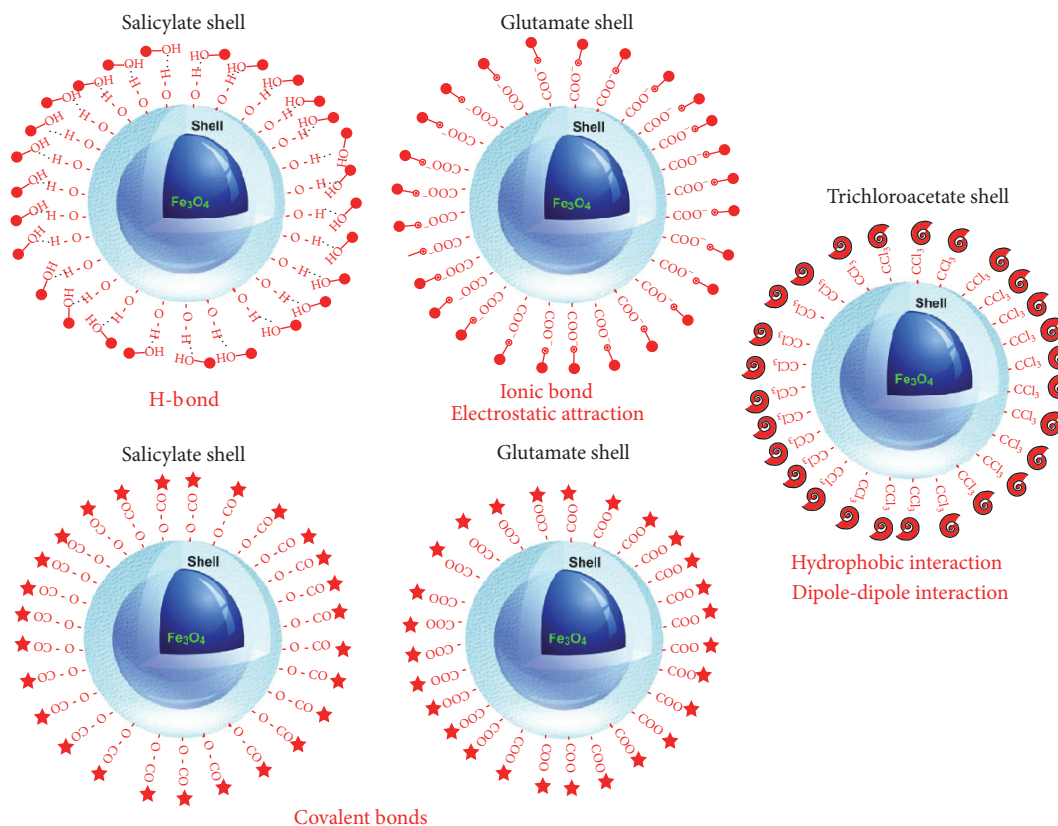


FIGURE 8: Potential interactions between the nanostructured core@shell structures and different biological active agents.

Conflicts of Interest

The authors declare that they have no conflicts of interest.

Acknowledgments

The present work was possible due to the EU-Funding Grant POSCCE-A2O2.2.1-2013-1, Project no. 638/12.03.2014, Code SMIS-CSNR 48652. The financial contribution received from the national project "New Nanostructured Polymeric Composites for Centre Pivot Liners, Centre Plate and Other Components for the Railway Industry (RONERANANOS-TRUCT)", no. 18 PTE (PN-III-P2-2.1-PTE-2016-0146), is also acknowledged.

References

- [1] X. W. Lou, L. A. Archer, and Z. Yang, "Hollow micro-/nanostructures: synthesis and applications," *Advanced Materials*, vol. 20, no. 21, pp. 3987–4019, 2008.
- [2] H. C. Zeng, "Synthetic architecture of interior space for inorganic nanostructures," *Journal of Materials Chemistry*, vol. 16, no. 7, pp. 649–662, 2006.
- [3] G. Zhang, Y. Liu, C. Zhang et al., "Aqueous immune magnetite nanoparticles for immunoassay," *Journal of Nanoparticle Research*, vol. 11, no. 2, pp. 441–448, 2009.
- [4] M. Tiemann, "Porous metal oxides as gas sensors," *Chemistry: A European Journal*, vol. 13, no. 30, pp. 8376–8388, 2007.
- [5] B. G. Trewyn, S. Giri, I. I. Slowing, and V. S.-Y. Lin, "Mesoporous silica nanoparticle based controlled release, drug delivery, and biosensor systems," *Chemical Communications*, no. 31, pp. 3236–3245, 2007.
- [6] F. Dong, W. Guo, and C.-S. Ha, "Monodisperse single-crystal mesoporous magnetite nanoparticles induced by nanoscale gas bubbles," *Journal of Nanoparticle Research*, vol. 14, no. 12, article no. 1303, 2012.
- [7] H.-M. Fan, M. Olivo, B. Shuter et al., "Quantum dot capped magnetite nanorings as high performance nanoprobe for multiphoton fluorescence and magnetic resonance imaging," *Journal of the American Chemical Society*, vol. 132, no. 42, pp. 14803–14811, 2010.
- [8] S. P. Foy, R. L. Manthe, S. T. Foy, S. Dimitrijevic, N. Krishnamurthy, and V. Labhasetwar, "Optical imaging and magnetic field targeting of magnetic nanoparticles in tumors," *ACS Nano*, vol. 4, no. 9, pp. 5217–5224, 2010.
- [9] H. Gupta, P. Paul, N. Kumar, S. Baxi, and D. P. Das, "One pot synthesis of water-dispersible dehydroascorbic acid coated Fe_3O_4 nanoparticles under atmospheric air: blood cell compatibility and enhanced magnetic resonance imaging," *Journal of Colloid and Interface Science*, vol. 430, pp. 221–228, 2014.
- [10] S. Gustafsson, A. Fornara, K. Petersson, C. Johansson, M. Muhammed, and E. Olsson, "Evolution of structural and magnetic properties of magnetite nanoparticles for biomedical applications," *Crystal Growth and Design*, vol. 10, no. 5, pp. 2278–2284, 2010.

- [11] A. H. Lu, E. L. Salabas, and F. Schüth, "Magnetic nanoparticles: synthesis, protection, functionalization, and application," *Angewandte Chemie—International Edition*, vol. 46, no. 8, pp. 1222–1244, 2007.
- [12] J. Gao, Z. Guo, S. Yu et al., "A novel controlled release system-based homogeneous immunoassay protocol for SCCA using magnetic mesoporous Fe₃O₄ as a nanocontainer and aminated polystyrene microspheres as a molecular gate," *Biosensors and Bioelectronics*, vol. 66, pp. 141–145, 2015.
- [13] J. Liu, F. Liu, K. Gao, J. Wu, and D. Xue, "Recent developments in the chemical synthesis of inorganic porous capsules," *Journal of Materials Chemistry*, vol. 19, no. 34, pp. 6073–6084, 2009.
- [14] W. H. Suh, A. R. Jang, Y.-H. Suh, and K. S. Suslick, "Porous, hollow, and ball-in-ball metal oxide microspheres: preparation, endocytosis, and cytotoxicity," *Advanced Materials*, vol. 18, no. 14, pp. 1832–1837, 2006.
- [15] Q. Sun, Z. Ren, R. Wang, W. Chen, and C. Chen, "Magnetite hollow spheres: Solution synthesis, phase formation and magnetic property," *Journal of Nanoparticle Research*, vol. 13, no. 1, pp. 213–220, 2011.
- [16] D. Caruntu, B. L. Cushing, G. Caruntu, and C. J. O'Connor, "Attachment of gold nanograins onto colloidal magnetite nanocrystals," *Chemistry of Materials*, vol. 17, no. 13, pp. 3398–3402, 2005.
- [17] Y. Li, H. Liao, and Y. Qian, "Hydrothermal synthesis of ultrafine α -Fe₂O₃ and Fe₃O₄ powders," *Materials Research Bulletin*, vol. 33, no. 6, pp. 841–844, 1998.
- [18] W.-W. Wang and Y.-J. Zhu, "Microwave-assisted synthesis of magnetite nanosheets in mixed solvents of ethylene glycol and water," *Current Nanoscience*, vol. 3, no. 2, pp. 171–176, 2007.
- [19] J. Matutes-Aquino, P. García-Casillas, O. Ayala-Valenzuela, and S. García-García, "Study of iron oxides obtained by decomposition of an organic precursor," *Materials Letters*, vol. 38, no. 3, pp. 173–177, 1999.
- [20] S. Sun and H. Zeng, "Size-controlled synthesis of magnetite nanoparticles," *Journal of the American Chemical Society*, vol. 124, no. 28, pp. 8204–8205, 2002.
- [21] J. Toniolo, A. S. Takimi, M. J. Andrade, R. Bonadiman, and C. P. Bergmann, "Synthesis by the solution combustion process and magnetic properties of iron oxide (Fe₃O₄ and α -Fe₂O₃) particles," *Journal of Materials Science*, vol. 42, no. 13, pp. 4785–4791, 2007.
- [22] D. Maity, S.-G. Choo, J. Yi, J. Ding, and J. M. Xue, "Synthesis of magnetite nanoparticles via a solvent-free thermal decomposition route," *Journal of Magnetism and Magnetic Materials*, vol. 321, no. 9, pp. 1256–1259, 2009.
- [23] Y. Liu, W. Zhu, D. Wu, and Q. Wei, "Electrochemical determination of dopamine in the presence of uric acid using palladium-loaded mesoporous Fe₃O₄ nanoparticles," *Measurement: Journal of the International Measurement Confederation*, vol. 60, pp. 1–5, 2014.
- [24] M. Kumari, C. U. Pittman, and D. Mohan, "Heavy metals [chromium (VI) and lead (II)] removal from water using mesoporous magnetite (Fe₃O₄) nanospheres," *Journal of Colloid and Interface Science*, vol. 442, pp. 120–132, 2015.
- [25] T. Xia, X. Xu, J. Wang et al., "Facile complex-coprecipitation synthesis of mesoporous Fe₃O₄ nanocages and their high lithium storage capacity as anode material for lithium-ion batteries," *Electrochimica Acta*, vol. 160, pp. 114–122, 2015.
- [26] E. Cheraghpour, A. M. Tamaddon, S. Javadpour, and I. J. Bruce, "PEG conjugated citrate-capped magnetite nanoparticles for biomedical applications," *Journal of Magnetism and Magnetic Materials*, vol. 328, pp. 91–95, 2013.
- [27] D. C. Culita, G. Marinescu, L. Patron, O. Carp, C. B. Cizmas, and L. Diamandescu, "Superparamagnetic nanomagnetites modified with histidine and tyrosine," *Materials Chemistry and Physics*, vol. 111, no. 2-3, pp. 381–385, 2008.
- [28] G. Goloverda, B. Jackson, C. Kidd, and V. Kolesnichenko, "Synthesis of ultrasmall magnetic iron oxide nanoparticles and study of their colloid and surface chemistry," *Journal of Magnetism and Magnetic Materials*, vol. 321, no. 10, pp. 1372–1376, 2009.
- [29] J. Razjouyan, H. Zolata, O. Khayat, F. Nowshiravan, N. Shadapour, and M. Mohammadnia, "Synthesis and evaluation of radiolabeled, folic acid-PEG conjugated, amino silane coated magnetic nanoparticles in tumor bearing Balb/C mice," *Nukleonika*, vol. 60, no. 3, pp. 479–502, 2015.
- [30] C. Tudisco, M. T. Cambria, F. Sinatra et al., "Multifunctional magnetic nanoparticles for enhanced intracellular drug transport," *Journal of Materials Chemistry B*, vol. 3, no. 20, pp. 4134–4145, 2015.
- [31] U. Gunduz, T. Keskin, G. Tansik et al., "Idarubicin-loaded folic acid conjugated magnetic nanoparticles as a targetable drug delivery system for breast cancer," *Biomedicine and Pharmacotherapy*, vol. 68, no. 6, pp. 729–736, 2014.
- [32] M. Licciardi, C. Scialabba, G. Cavallaro, C. Sangregorio, E. Fantechi, and G. Giammona, "Cell uptake enhancement of folate targeted polymer coated magnetic nanoparticles," *Journal of Biomedical Nanotechnology*, vol. 9, no. 6, pp. 949–964, 2013.
- [33] D. Rehana, A. K. Haleel, and A. K. Rahiman, "Hydroxy, carboxylic and amino acid functionalized superparamagnetic iron oxide nanoparticles: Synthesis, characterization and in vitro anti-cancer studies," *Journal of Chemical Sciences*, vol. 127, no. 7, pp. 1155–1166, 2015.
- [34] D. Fikai, E. Andronesco, A. Fikai et al., "Synthesis and Characterization of Mesoporous Magnetite Based Nanoparticles," *Current Nanoscience*, vol. 8, no. 6, pp. 875–879, 2012.
- [35] M. Abboud, S. Youssef, J. Podlecki, R. Habchi, G. Germanos, and A. Foucaran, "Superparamagnetic Fe₃O₄ nanoparticles, synthesis and surface modification," *Materials Science in Semiconductor Processing*, vol. 39, pp. 641–648, 2015.
- [36] E. Karaoğlu, A. Baykal, H. Erdemi, L. Alpsoy, and H. Sozeri, "Synthesis and characterization of dl-thioctic acid (DLTA)-Fe₃O₄ nanocomposite," *Journal of Alloys and Compounds*, vol. 509, no. 37, pp. 9218–9225, 2011.
- [37] M. Anbarasu, M. Anandan, E. Chinnasamy, V. Gopinath, and K. Balamurugan, "Synthesis and characterization of polyethylene glycol (PEG) coated Fe₃O₄ nanoparticles by chemical coprecipitation method for biomedical applications," *Spectrochimica Acta—Part A: Molecular and Biomolecular Spectroscopy*, vol. 135, pp. 536–539, 2015.

Research Article

Magnetic Mineral Nanocomposite Sorbents for Wastewater Treatment

Oksana Makarchuk,¹ Tetiana Dontsova,¹ Anatolii Perekos,²
Alexander Skoblik,² and Yevhen Svystunov²

¹Chemical Technology Department, National Technical University of Ukraine "Igor Sikorsky Kyiv Polytechnic Institute",
Victory Avenue 37, Kyiv 03056, Ukraine

²G. V. Kurdyumov Institute for Metal Physics National Academy of Sciences of the Ukraine, Academician Vernadsky Blvd. 36,
Kyiv 03680, Ukraine

Correspondence should be addressed to Oksana Makarchuk; xtfhn9207@ukr.net

Received 23 February 2017; Accepted 30 April 2017; Published 29 May 2017

Academic Editor: Vidyadhar Singh

Copyright © 2017 Oksana Makarchuk et al. This is an open access article distributed under the Creative Commons Attribution License, which permits unrestricted use, distribution, and reproduction in any medium, provided the original work is properly cited.

Magnetic nanocomposite sorbents for disposal of synthetic detergents from wastewater were synthesized. Obtained sorbents based on clay minerals (saponite, palygorskite, and spondyle clay) and magnetite were characterized by X-ray powder diffraction, Mössbauer spectroscopy, and ballistic method with Steinberg magnetometer. As a result, the average crystallite sizes of Fe₃O₄ nanoparticles in magnetic nanocomposites were 2–10 nm. Magnetic nanocomposites had superparamagnetic properties and were classified as soft magnetic materials. Comparison of sorption properties showed that magnetic composite sorbents had efficiency of adsorption removal of anionic surfactants and polyphosphates from aqueous solution 2–8 times higher compared to native clay minerals. Spent magnetic nanocomposites were effectively removed from the aqueous solution by magnetic separation. So, the efficiency of magnetic composites application and implementing of magnetic separation in adsorption purification was confirmed.

1. Introduction

Currently there is a shortage, depletion, and quality deterioration of water resources as a result of their growing contamination. Synthetic surfactants (SAs) and polyphosphates have occupied special place among water pollutants. SDs are widely used in household, industry, and agriculture. Although aquatic ecosystems are capable of self-regulation and biological purification, they are unable to cope with the toxic compounds of the SDs that are extremely stable and are stored in the water for years [1, 2].

As strong carcinogenic agents SAs and their degradation products are toxic and can accumulate in the body and cause irreversible pathological changes. Furthermore, SAs slow the decay of other carcinogens and inhibit the process of biochemical oxidation and nitrification [3, 4].

Soluble phosphorus causes eutrophication of water bodies. Polyphosphates also bring a great harm to the human

body; penetrating to skin capillaries they change the percentage of hemoglobin structure and density of the plasma. Besides this, polyphosphate impurities create conditions for more intensive penetration of anionic surfactant through the skin and provoke dermatological diseases [5].

Adsorption purification with a large diversity of sorption materials is a universal method for treatment of both highly concentrated and low concentrated waste water [6]. Activated carbon is the traditional and most commonly used sorbent for water treatment. However, the high cost of activated carbon calls into question the prospects of its use for the treatment of sewage [7].

Cheap clay minerals show a large sorption activity against pollutants of various nature. Mixture of layered and not layered clay minerals is recommended for disposal of wastewater contaminated by SAs [8]. Composite sorbents based clay minerals have high sorption capacity relative polyphosphates [9]. However, the high sorption activity of mineral sorbents

is provided in the case of colloidal degree of their dispersion. But, in wastewater treatment, a problem of removing of spent sorbent particulate from water occurs.

The solution of this problem is providing magnetic properties for cheap natural clay minerals [10]. As a magnetic modifier magnetic iron oxides Fe_3O_4 , $\gamma\text{-Fe}_2\text{O}_3$, and $\alpha\text{-Fe}_2\text{O}_3$ are usually used. Magnetic support of sorption treatment of wastewater by cheap natural sorbents, which provides rapid separation of the spent sorbent from purified water in a magnetic field, is beneficial from a technological and economic standpoint [11].

The paper considers the synthesis and characterization of magnetic nanocomposite sorbents based on clay minerals and magnetite; the efficiency of the magnetic composites for wastewater treatment from the anion surfactant and polyphosphates is estimated.

2. Experimental

2.1. Synthesis of Composites. Clay minerals, saponite, palygorskite, and spondyle clay (Ukraine) were selected for the creation of the magnetic composites sorbents (MC). These materials have paramagnetic properties. It makes them suitable for creation on their basis of magnetic sorbents. For synthesis of MC, the magnetic modifier Fe_3O_4 was used in the form of magnetic fluid obtained by Elmore method [12]. Clay minerals have affinity to multicharged cations (particularly iron ions Fe^{2+} and Fe^{3+}) that determined by morphological, crystal, and chemistry features of clays [13]. Therefore, magnetic composite sorbents based on magnetite in an amount of 7% wt. and saponite (MCSp-7), palygorskite (MCP-7), and spondyle clay (MCSd-7) were synthesized by simple impregnation method.

2.2. X-Ray Analysis. Powder X-ray diffraction (XRD) analysis of natural clays, magnetite, and composites on their base was performed on Rigaku Ultima IV X-ray powder diffractometer with $\text{Cu K}\alpha$ radiation (40 kV, 30 mA). Crystallographic Open Database (COD) was applied for phase composition definition of sorbents. The crystallite sizes and the unit cell parameters of magnetite and magnetite in magnetic composites were calculated by software package PDXL.

2.3. Mössbauer Spectroscopy. Mössbauer spectra were recorded on MS1101E spectrometer in a mode with constant acceleration employing $^{57}\text{Co}(\text{Cr})$ source. Calibration of isomeric shift (δ) values was carried out relative to $\alpha\text{-Fe}$ at room temperature.

2.4. Magnetic Characteristics. Magnetic properties of nanocomposites (specific magnetization σ_s ($\text{A}\cdot\text{m}^2/\text{kg}$); magnetic field strength H_c (A/m); magnetic induction B_r (mT)) were determined by ballistic magnetometer of Steinberg.

2.5. Adsorption Procedure. Comparative analysis of MC sorption properties and natural clays was carried by constructing of adsorption isotherms of main components of synthetic detergents removal such as anionic surfactants

(sodium dodecyl benzenesulfonate (SDBS), sodium lauryl sulfate (SLS)) and polyphosphates (tripolyphosphate (TPP) and hexametaphosphate (HMP)). Adsorption properties of magnetite were not studied since Fe_3O_4 is a not porous material.

For sorption studies, a series of 250-mL glass flasks were filled with 100 mL of model wastewater solution of different initial contaminant concentrations (50–1000 $\text{mg}\cdot\text{L}^{-1}$). A fixed amount of sorbent material (1 g) was added to each flask and stirred (350 rpm) for 1 hour at thermostatic water bath shaker ($20 \pm 2^\circ\text{C}$) to ensure complete sorption equilibrium. After adsorption, spent magnetic composites MCSp-7, MCP-7, and MCSd-7 were separated by the external magnetic field, while clays adsorbents saponite, palygorskite, and spondyle clay were separated with centrifugal separation. The residual (equilibrium) concentration of anionic SAs in the sample was measured by direct two-phase (2P) titration of cationic surfactant in the layer of chloroform [14]. The equilibrium concentrations of phosphate in the solutions after adsorption treatment were determined by photometric method of molybdophosphate blue complex using UV-5800PC Spectrophotometer [15]. The equilibrium adsorption capacities (Q_e) were calculated according to the following formula:

$$Q_e = \frac{(C_e - C_0) \cdot V}{m}, \quad (1)$$

where C_0 and C_e are initial and equilibrium concentration of pollutant in solution, respectively, $\text{mg}\cdot\text{L}^{-1}$; V is model solution volume, L; m is mass of sorbent sample, g.

2.6. Magnetic Separation. The magnetic separation process was investigated in an aqueous medium in magnetic filter equipped with permanent magnets with an intensity of external magnetic field 66 mT and in the absence of permanent external magnetic field. The efficiency of magnetic separation was determined by the residual concentration of suspended sorbent particles in aqueous medium through 5, 30, and 60 min of magnetic separation by turbidimetric method [16].

3. Results and Discussion

3.1. XRD Analysis. Results of powder X-ray diffractions of magnetite, MC, and natural clays were recorded using a Rigaku Ultima IV diffractometer. The corresponding diffraction patterns are presented in Figure 1 (magnetite), Figure 2 (MCSp-7 and saponite), Figure 3 (MCP-7 and palygorskite), and Figure 4 (MCSd-7 and spondyle clay).

From the XRD pattern of Fe_3O_4 (Figure 1), the strong characteristic peaks of Fe_3O_4 were detected at 2θ (hkl) = 30.72° (220), 35.58° (311), 43.72° (400), 53.64° (422), 57.24° (511), and 62.86° (440) (card number 01-071-6336). The XRD results do not show the presence of impurities or of other phases. So, the method of Elmore provides obtaining the pure magnetic modifying agent.

The XRD pattern of the native saponite (Figure 2(a)) indicated peaks that correspond to saponite (card number 00-013-0305), montmorillonite (card number 00-002-0014), quartz (card number 00-001-0649), and calcite (card number

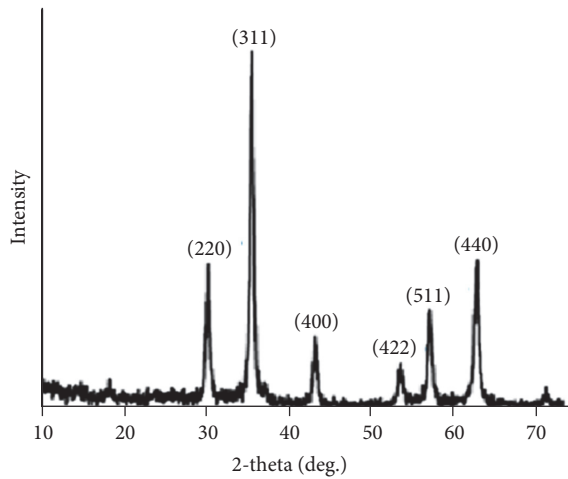


FIGURE 1: The XRD patterns of magnetite Fe_3O_4 .

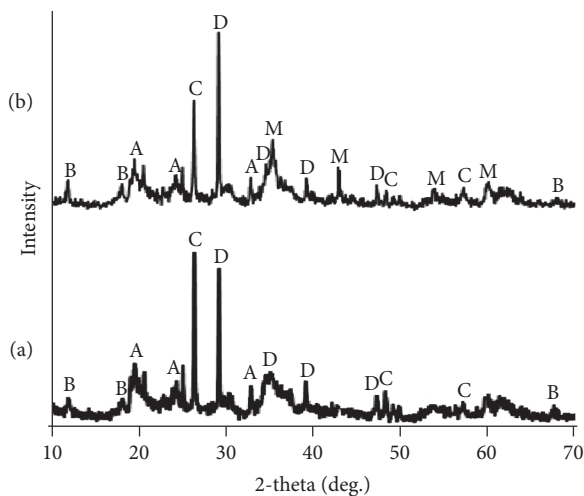


FIGURE 2: The XRD patterns of saponite (a) and MCSp-7 (b): A, saponite $\text{NaMg}_3[\text{AlSi}_3\text{O}_{10}](\text{OH})_2 \cdot 4\text{H}_2\text{O}$; B, montmorillonite $\text{NaMgAlSi}_2\text{O}_7(\text{OH}) \cdot \text{H}_2\text{O}$; C, quartz SiO_2 ; D, calcite CaCO_3 ; M, magnetite Fe_3O_4 .

00-002-0623). The X-ray diffraction pattern of composite sorbent MCSp-7 (Figure 2(b)) showed well-developed diffraction lines assigned to inherent phases of native saponite clay, with all major peaks matching the standard pattern of Fe_3O_4 (card number 01-071-6336).

Broad diffraction peaks attributed to peaks of pure palygorskite (card number 01-082-1872) and quartz (card number 00-001-0649) were demonstrated on the XRD pattern of palygorskite (Figure 3(a)). The characteristic diffraction peaks of sets of these two main phases were observed in diffraction pattern of magnetic composite MCP-7 (Figure 3(b)). The position of the rest diffraction peaks of MCP-7 diffraction pattern was well matched with data from the COD card for Fe_3O_4 .

According to the X-ray diffraction analysis presented in Figure 4, a spondyle clay consists of two minerals such

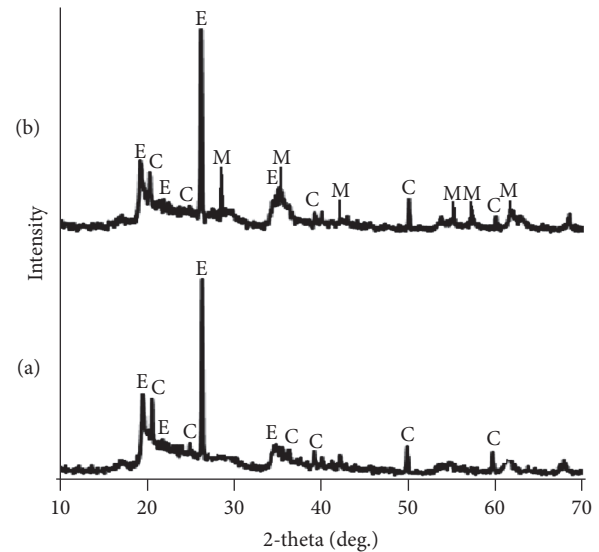


FIGURE 3: The XRD patterns of palygorskite (a) and MCP-7 (b): E, palygorskite $(\text{Mg}_{0.669}, \text{Al}_{0.331})_4(\text{Si}_4\text{O}_{10})_2(\text{OH})_2 \cdot 8\text{H}_2\text{O}$; C, quartz SiO_2 ; M, magnetite Fe_3O_4 .

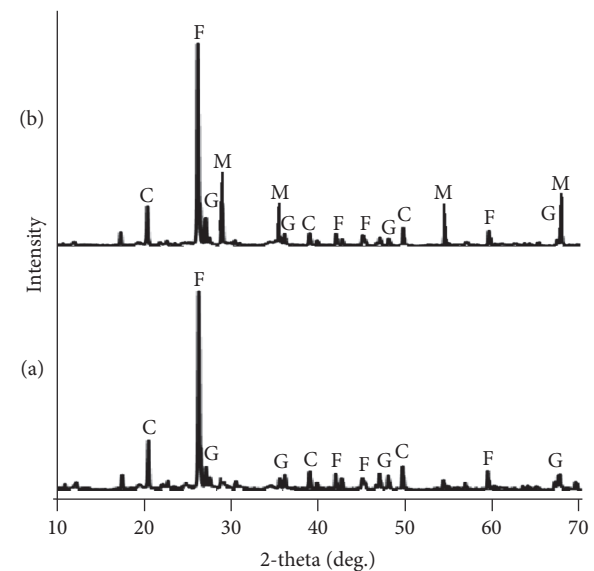


FIGURE 4: The XRD patterns of spondyle clay (a) and MCSd-7 (b): F, augite $\text{Ca}(\text{Mg}, \text{Fe}, \text{Al})[(\text{Si}, \text{Al})_2\text{O}_6]$; G, pigeonite $(\text{Ca}, \text{Mg}, \text{Fe})(\text{Mg}, \text{Fe})\text{Si}_2\text{O}_6$; C, quartz SiO_2 ; M, magnetite Fe_3O_4 .

as augite (card number 01-088-0831) and pigeonite (card number 01-087-0693). Phase composition of sample MCSd-7 differs from native spondyle clays by the presence of magnetite peaks (card number 01-071-6336).

Thus, the synthesis of composite magnetic sorbents impregnation method did not lead to changes in the phase composition of clay minerals.

The XRD patterns of MC and magnetite were automatically analyzed by software package PDXL. The crystallite sizes and the unit cell parameters of magnetite and magnetite in magnetic composites were calculated and reported in Table 1.

TABLE 1: X-ray analysis of magnetic sorbents on the base of saponite, palygorskite, spondyle clay, and magnetite.

Sample	Average size of Fe_3O_4 crystallites, nm	Cell parameters, nm		
		a	b	c
MCSp-7	9.6	0.833	0.833	0.833
MCP-7	2.5	0.844	0.844	0.844
MCSd-7	9.2	0.831	0.831	0.831
Fe_3O_4	17.9	0.835	0.835	0.835

As stated in Table 1 magnetite in composite sorbents were obtained in the nanorange. The average crystallite size of Fe_3O_4 nanoparticles was 2–10 nm. So, magnetic nanocomposites are received, where nanosized magnetic modifier stabilized in the clay mineral matrix.

3.2. Mössbauer Spectroscopy. Mössbauer spectrums of native saponite clay (Figure 5(a)) and magnetic composite based on its MCSp-7 (Figure 5(b)) were similar to each other. Both spectrums were characterized by the presence of doublets with parameters corresponding to bivalent Fe^{2+} and trivalent Fe^{3+} iron ions. Spectrum of saponite included the sextet of low intensity, which showed the presence of magnetite in the composition of native natural clay in small quantities. Sextet of great intensity that according to work [17] corresponds to Fe_3O_4 particles with sizes less than 10 nm [17] was found in the spectrum of MCSp-7.

In the Mössbauer spectrums of MCP-7 (Figure 5(d)) and MCSd-7 (Figure 5(f)) the superposition of two components such as poorly intensive extended sextet that according to work [17] corresponds to Fe_3O_4 particles with dimensions less than 10 nm and doublet that meets parameters of trivalent iron ions Fe^{3+} occurred. Parameters of doublet shown in Figure 5(d) coincided with doublet of iron ions Fe^{3+} of the native palygorskite (Figure 5(c)). As shown in Figure 5(e) in the initial state for spondyle clay the existence of two doublets was discovered. In addition to intense doublet parameters which well coincided with doublets for iron ions Fe^{3+} of MCSd-7 (Figure 5(f)) the doublet of weak intensity with parameters corresponding to bivalent iron ions Fe^{2+} was detected.

Thus, Mössbauer spectrums of all MC samples except sextets were characterized by presence of doublets. This confirms that the magnetic modifier particles of magnetic composite sorbents are in nanoscale range (less than 10 nm) and have superparamagnetic properties [17]. Thereby, the magnetic properties of nanosized magnetite stabilized by mineral matrix are primarily determined by the size of its particles.

3.3. Characteristics of the Magnetic Properties. The specific saturation magnetization, magnetic field strength, and magnetic induction of saponite, palygorskite, spondyle clay, Fe_3O_4 , and synthesized MC samples are summarized in Table 2. Natural clays were characterized by specific saturation zero magnetization; therefore these minerals were

TABLE 2: Magnetic characteristics of sorbent samples.

Sample	$\sigma_{s(10)}$, $\text{A}\cdot\text{m}^2/\text{kg}$	H_c , A/m	B_r , mT
Saponite	0	0	0
MCSp-7	4.5	954.9	0.16
Palygorskite	0	0	0
MCP-7	3.9	954.9	0.10
Spondyle clay	0	0	0
MCSd-7	6.3	1909.9	0.20
Fe_3O_4	90.0	501.3	3.50

classified as paramagnetic materials. When paramagnetic mineral matrix of composite enters to the magnetic separator, it is magnetized in the direction of the external magnetic field. Therefore, controllability of magnetic separation process is determined by the properties of ferromagnetic particles of modifier.

In the synthesis of MCSp-7, MCP-7, and MCSd-7 in the clay matrix, the Fe_3O_4 crystallites were formed about the same size of 2–10 nm (Table 1); based on this, the specific saturation magnetization of MC samples was approximately the same. Hence, the nanoscale magnetite particles of composite sorbents were formed with the low residual magnetization; therefore MC are classified as soft magnetic materials.

According to the results presented in Table 2, the values of magnetic field strength H_c and magnetic induction B_r are growing with the increasing of size of Fe_3O_4 crystallites. However, for nanosized magnetite with size of crystallites 17.9 nm, the H_c value was found relatively low. This regularity is typical for nanoscale particles of magnetic oxides. The maximum value H_c is characteristic for magnetite nanoparticles with size of about 30 nanometers. Since the magnetite change of reversal mechanism from reorientation of magnetic moments (single-domain state) to displacement of domain walls (poly-domain state) for magnetite particles occurred at about 30 nm [18], consequently, for single-domain nanoparticles of Fe_3O_4 less than 30 nm is inherent in the increase of magnetic field strength with increasing in size. For magnetite nanoparticles larger than 30 nm the descending dependency of H_c versus particle size was discovered. Thereby, nanoscale particles of magnetic modifier in the composition of magnetic sorbents were characterized by superparamagnetic properties.

3.4. Adsorption Experiment. The maximum sorption capacity of MCSp-7, MCSd-7, and MCP-7 in relation to the anionic SAs was in the range of 35–47 mg SDBS/g and 30–36 mg SLS/g (Figures 6(a) and 6(b)). The sorption capacities of native saponite, spondyle clay, and palygorskite for SDBS and SLS obtained from the sorption isotherms were 2–4 and 2–8 times lower. As we can see from Figures 6(c) and 6(d), the maximum sorption capacities of magnetic composites towards TPP and HMP were 3 and 4 times higher, respectively, compared to the native clay minerals and amounted to 550–570 mg TPP/g and 790–810 mg HMP/g.

Thus, modification of clay minerals using nanoscale magnetite in an amount of 7 wt.% has enhanced adsorption capacity of natural clays. In our view, it was related to

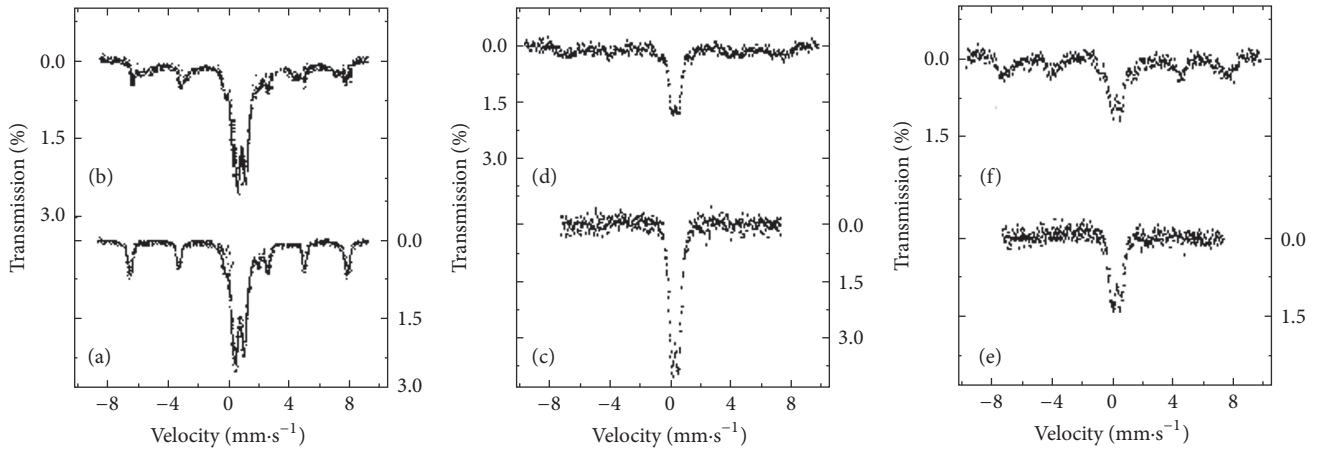


FIGURE 5: Mössbauer spectra for the pure saponite (a), palygorskite (c), and spondyle clay (e) and magnetic composites MCSp-7 (b), MCP-7 (d), and MCSd-7 (f).

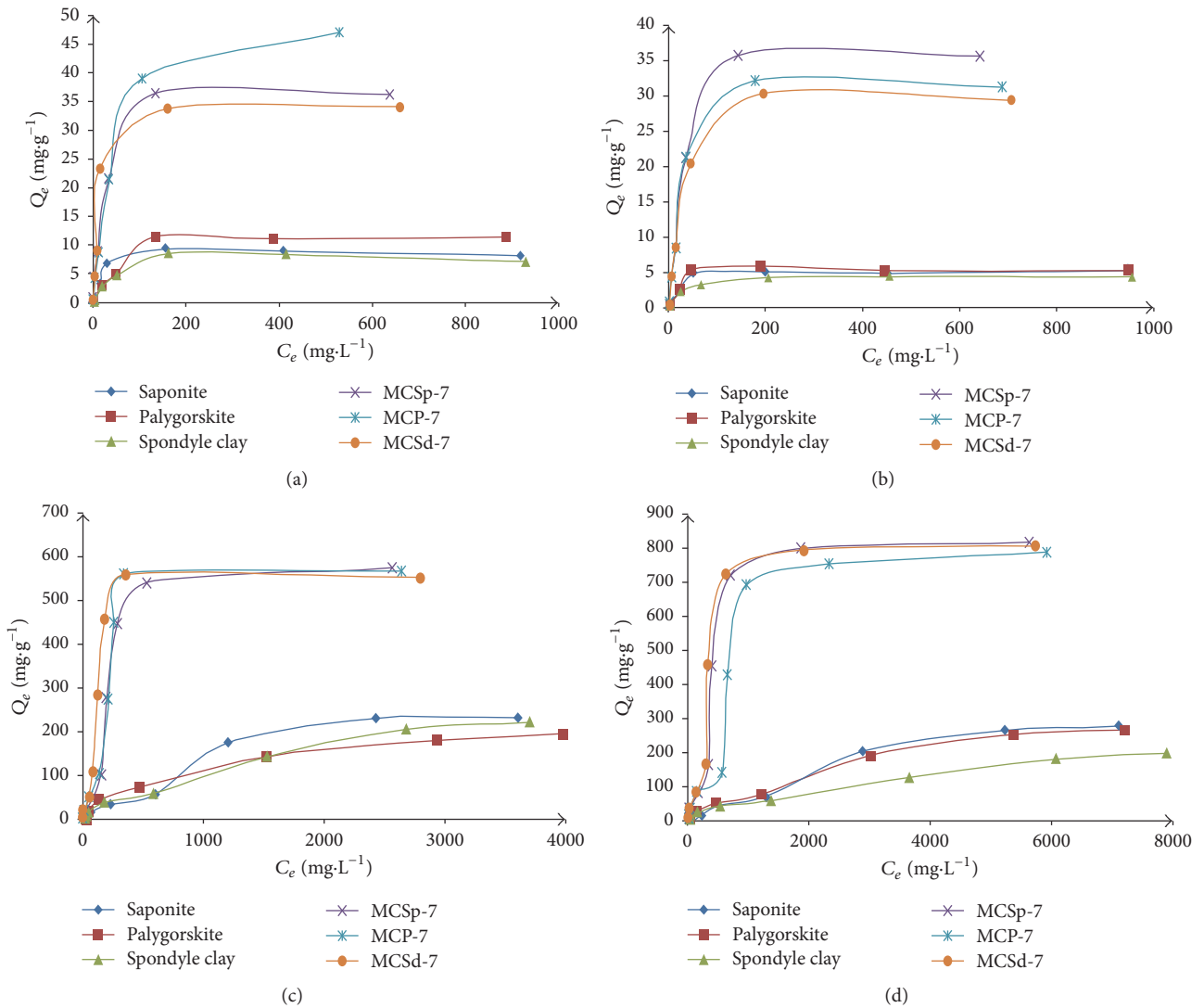


FIGURE 6: Adsorption isotherm of SDBS (a), SLS (b), TPP (c), and HMP (d) on sorbents samples.

TABLE 3: Characteristics of the magnetic separation process of spent sorbents.

Sample	66 mT			0 mT		
	5 min	30 min	60 min	5 min	30 min	60 min
Saponite	558.8	387.7	327.1	555.7	384.2	326.0
MCSp-7	32.7	1.0	<0.5	501.0	236.6	150.4
Palygorskite	662.7	418.2	351.6	664.8	421.3	355.3
MCP-7	26.6	<0.5	<0.5	506.6	245.4	148.2
Spondyle clay	713.8	526.0	464.9	712.4	523.7	466.5
MCSd-7	14.9	5.4	<0.5	491.0	249.9	179.3

change of porous structure of natural clay minerals caused by the formation of micropores and mesopores sorbent structure and stabilization of Fe_3O_4 nanoparticles on their pores surface. The comparative analysis of porous structures saponite clays and magnetic composites based on it are given in the work [13].

3.5. Magnetic Separation Process. Table 3 shows the kinetic of separation of clay minerals and magnetic composites in external magnetic field 66 mT and in absence of permanent external magnetic field. Separation of magnetic sorbents from the purified solution in a filter equipped with permanent magnets was held 36 times faster. 98% of spent magnetic sorbent mass was precipitated for the first 5 minutes by magnetic separation. Application of magnetic composites has ensured the achievement of the residual concentration of suspended solids ≤ 0.02 mg/L for 30 minutes of magnetic separation.

The residual concentration of magnetic composites was 2.5 times less than native clay sorbents at the separation in the absence of a magnetic field (0 mT). Therefore, magnetic composites are ferromagnetic materials for which macroscopic magnetic moment, which exists even without external magnetic field, is available. As follows, efficiency of application of magnetic composites and implementing of magnetic separation in adsorption purification is obvious.

4. Conclusions

Magnetic nanocomposite sorbents on mineral base (saponite, palygorskite, and spondyle clay) were synthesized by impregnation method. The pure magnetic modifying agent Fe_3O_4 was obtained by method of Elmore.

The magnetic properties of nanosized magnetite stabilized by mineral matrix are primarily determined by the size of its particles. In the synthesis of MCSp-7, MCP-7, and MCSd-7 in the clay matrix the magnetite crystallites were formed approximately in the same range (2–10 nm). Magnetite particles in magnetic composites were in single-domain state and characterized by specific superparamagnetic properties. MC were classified to the soft magnetic materials.

The sorption capacities of obtained magnetic composites towards anionic surfactants and polyphosphates exceeded the sorption capacity of clay minerals by 2–8 times. The detected

effect was caused by stabilization of magnetite nanoparticles on the surface of clay pores and by the formation of micropores and mesopores sorbent structure.

Spent magnetic sorbents were removed from purified water by magnetic separation 36 times faster compared to the native clays. Thus, the use of magnetic nanocomposites based on natural clays and magnetite for the removal of organic pollutants is technologically and economically advantageous solution in water purification.

Conflicts of Interest

The authors declare that there are no conflicts of interest regarding the publication of this paper.

References

- [1] L. Harutyunyan and G. Pirumyan, "Purification of waters from anionic and cationic surfactants by natural zeolites," *Chemistry and Biology*, vol. 1, pp. 21–28, 2015.
- [2] O. Makarchuk and T. Dontsova, "Removal of polyphosphates from wastewater by magnetic composite mineral sorbents," *European Chemical Bulletin*, vol. 5, no. 12, pp. 515–523, 2016.
- [3] R. Priti and D. Hemangi, "Removal of anionic surfactant sodium dodecyl sulphate (SDS) from aqueous solution by using alumina," *J. Environ. Res. Develop.*, vol. 7, pp. 851–862, 2012.
- [4] O. Vladimirovna Makarchuk and T. Anatolievna Dontsova, "Removal of anionic surfactants from wastewater by magnetic mineral sorbents," *Journal of Water Security*, vol. 2, no. 1, 2016.
- [5] T. Osalo, E. Merufinia, and M. Saatlo, "Phosphorus removal from aqueous solutions by bentonite: effect of Al_2O_3 ," *Journal of Civil Engineering and Urbanism*, vol. 3, no. 5, pp. 317–322, 2013.
- [6] A. Bhatnagar and M. Sillanpää, "Utilization of agro-industrial and municipal waste materials as potential adsorbents for water treatment—a review," *Chemical Engineering Journal*, vol. 157, no. 2–3, pp. 277–296, 2010.
- [7] D. Kaušpediene, E. Kazlauskienė, A. Gefeniene, and R. Binkienė, "Comparison of the efficiency of activated carbon and neutral polymeric adsorbent in removal of chromium complex dye from aqueous solutions," *Journal of Hazardous Materials*, vol. 179, no. 1–3, pp. 933–939, 2010.
- [8] M. J. Sánchez-Martín, M. C. Dorado, C. del Hoyo, and M. S. Rodríguez-Cruz, "Influence of clay mineral structure and surfactant nature on the adsorption capacity of surfactants by clays," *Journal of Hazardous Materials*, vol. 150, no. 1, pp. 115–123, 2008.

- [9] Y. Gao, N. Chen, W. Hu et al., "Phosphate removal from aqueous solution by an effective clay composite material," *Journal of Solution Chemistry*, vol. 42, no. 4, pp. 691–704, 2013.
- [10] N. Mykhailenko, O. Makarchuk, T. Dontsova, S. Gorobets, and I. Astrelin, "Purification of aqueous media by magnetically operated saponite sorbents," *Eastern European Journal of Enterprise Technologies*, vol. 4, no. 10, pp. 13–20, 2015.
- [11] O. V. Makarchuk, T. A. Dontsova, and I. M. Astrelin, "Magnetic clay sorbent for the removal of dyes from aqueous solutions," *Research Bulletin of the National Technical University of Ukraine "Kyiv Polytechnic Institute"*, vol. 6, pp. 109–114, 2015.
- [12] C. V. Thach, N. H. Hai, and N. Chau, "Size controlled magnetite nanoparticles and their drug loading ability," *Journal of the Korean Physical Society*, vol. 52, no. 5, pp. 1332–1335, 2008.
- [13] O. V. Makarchuk, T. A. Dontsova, and I. M. Astrelin, "Magnetic nanocomposites as efficient sorption materials for removing dyes from aqueous solutions," *Nanoscale Research Letters*, vol. 11, article 161, 2016.
- [14] T. M. Schmitt, *Analysis of Surfactants*, Marcel Dekker, New York, NY, USA, 2001.
- [15] H. Waldhoff and R. Spilker, *Handbook of Detergents. Part C: Analysis*, CRC Press, Taylor & Francis Group, Boca Raton, Fla, USA, 2004.
- [16] R. D. Kos'yan, I. S. Podymov, and S. Y. Kuznetsov, "Turbidimetric measuring of the suspended sediment concentration in the coastal zone," in *Proceedings of the 1998 26th International Conference on Coastal Engineering, ICCE-98*, vol. 26, pp. 2303–2316, 1998.
- [17] G. F. Goya, T. S. Berquó, F. C. Fonseca, and M. P. Morales, "Static and dynamic magnetic properties of spherical magnetite nanoparticles," *Journal of Applied Physics*, vol. 94, no. 5, pp. 3520–3528, 2003.
- [18] A. Doroshenko and I. Chekman, "Magnetic nanoparticles: properties and biomedical applications," *Ukrainian Medical Journal*, vol. 4, no. 102, pp. 10–13, 2014.

Research Article

Investigation of Various Cross-Linking Methods for the Immobilization of Cytosine Arabinoside on Bacterial Magnetosomes

Qinglei Dai,¹ Yiming Ma,¹ Shibin Wang,^{1,2,3}
Ranjith Kumar Kankala,^{1,3} and Yuangang Liu^{1,2,3}

¹College of Chemical Engineering, Huaqiao University, Xiamen 361021, China

²Institute of Pharmaceutical Engineering, Huaqiao University, Xiamen 361021, China

³Fujian Provincial Key Laboratory of Biochemical Technology, Xiamen 361021, China

Correspondence should be addressed to Yuangang Liu; ygliu@hqu.edu.cn

Received 16 March 2017; Revised 26 April 2017; Accepted 27 April 2017; Published 22 May 2017

Academic Editor: Vidyadhar Singh

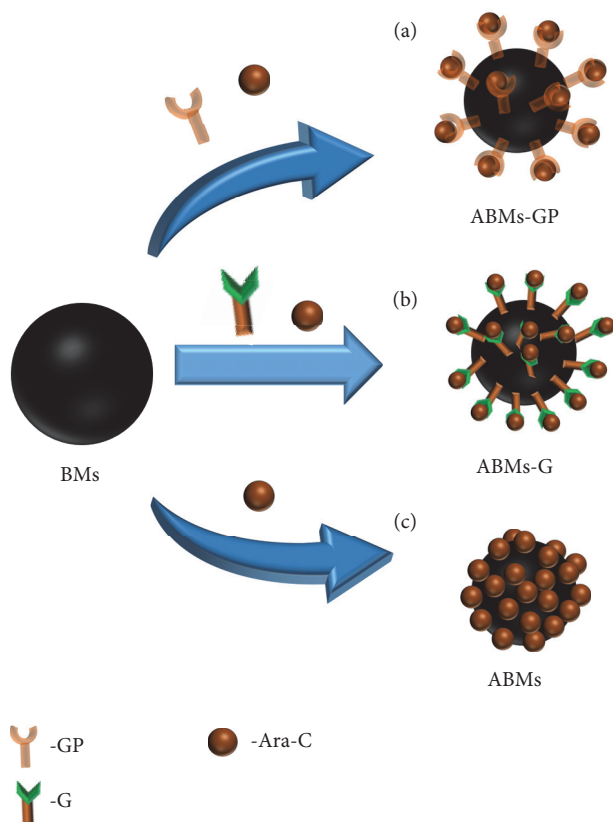
Copyright © 2017 Qinglei Dai et al. This is an open access article distributed under the Creative Commons Attribution License, which permits unrestricted use, distribution, and reproduction in any medium, provided the original work is properly cited.

Bacterial magnetosomes (BMs) have emerged as potential drug delivery vehicles, possessing an iron oxide or iron sulfide core surrounded by a natural lipid membrane shell. In this study, we immobilized cytosine arabinoside (Ara-C) effectively on BMs by using various methods such as direct absorption (ABMs), and others include different cross-linkers such as genipin (GP) and glutaraldehyde (G). A well-dispersed Ara-C coupled bacterial magnetosomes resulted in significantly higher negative charge than that of naked BMs (-11.5 ± 0.3 mV) confirming the drug loading. Out of all methods, direct absorption process led to the highest encapsulation efficiency and drug loading of $88.2 \pm 4.3\%$ and $46.9 \pm 1.2\%$, respectively. These designs have shown the long-term drug release behavior without an initial burst release. Our results indicate that BMs-based nanoconjugates will potentially find widespread applications in pharmaceutical field.

1. Introduction

Recently, the explosive growth of utilization of nanotechnology for the preparation of delivery systems has led to the great progress in the field of medicine [1]. This technology provides an efficient alternative strategy to conventional delivery systems in not only for delivering drugs and genes to various therapeutic sites but also for bioimaging, tissue engineering, and others [2, 3]. The efficient therapeutic strategies from this technology include, but are not limited to, polymer nanoparticles [4, 5], lipid-based nanoparticles [6, 7], and inorganic nanomaterials based on iron oxide [8], gold [9], and quantum dots and others [10]. Amongst inorganic nanomaterials, magnetic nanoparticles have drawn much attention in biomedical, medical diagnosis, and medical fields because of their tunable size, narrow size distribution, and unique optoelectronic features [11–13]. They have shown remarkable potential in biomedical research, especially their

ability in combining therapeutic moieties with diagnostic agents [14, 15], which attributes to their inherent biocompatibility, magnetic properties, and high surface-area-to-volume ratio. Negatively charged bacterial magnetosomes (BMs) are one of the most efficient magnetic nanoparticles intended for the delivery of various bioactive moieties [16, 17]. In regard of designing the drug delivery carrier, BMs do not require any external modification/surface functionalization to improve the drug loading efficiency unlike that required for other magnetic nanoparticles. In general, BMs are biogenic magnetite derived from magnetotactic bacteria. These are composed of iron oxide or iron sulfide minerals enveloped by lipid membrane rich in amino groups [18, 19]. In addition, previous literatures have evidenced that BMs are used to deliver various therapeutic agents such as drugs [20, 21], enzyme [22], and DNA [23]. In a case, the activity of glucose oxidase immobilized BMs is 40 times effective than those immobilized on artificial magnetite particles [24]. In



SCHEME 1: Graphical illustration showing the Ara-C immobilization on BMs through various methods and their resultant end products, (a) genipin (GP) cross-linker (ABMs-GP), (b) glutaraldehyde (G) cross-linker (ABMs-G), and (c) direct absorption method (ABMs).

another instance, BMs have been used as vectors for the chemotherapeutic drug conjugation, that is, methotrexate (MTX), which has shown exceptional loading and in vitro release behavior of MTX [25]. Moreover, after modifying with poly-L-glutamic acid, the drug loading amount was significantly increased in BMs [26].

In this paper, we designed a delivery system possessing BMs loaded with Ara-C effectively by using different methods such as direct absorption (ABMs), and others include different cross-linkers (GP and G) which resulted in different ABMs (ABMs-GP, ABMs-G), respectively (Scheme 1). Further, we investigate the release behavior of antitumor drug Ara-C from BMs nanoconjugates.

2. Materials and Methods

2.1. Materials. Bacterial magnetosomes derived from *Magnetospirillum* sp. ME-1 were provided by Wuhan Institute of Virology, Chinese Academy of Sciences. Ara-C was purchased from Sunray Pharmaceutical Co., Ltd. (Suzhou, China). Genipin (GP) was obtained from Zhixin Biotechnology Company (Fuzhou, China). Glutaraldehyde (G) was purchased from Sigma Aldrich (USA). All other additional chemicals utilized were purchased from Sinopharm Chemical Reagent Co., Ltd. (Beijing, China).

2.2. Ara-C Immobilization on BMs. Due to abundant amino groups in the lipid membrane shell, bacterial magnetosomes isolated from the cells of magnetotactic bacteria are extremely suitable for Ara-C immobilization [19]. Ara-C also has the amino active sites suitable for immobilization. The immobilization of Ara-C is investigated by using various methods such as direct absorption method, and others include various cross-linkers (GP and G). The scheme of preparation was based on our previous study [27].

Initially, purified BMs were suspended in PBS (pH 7.4) and the suspension was subjected to ultrasonic bathing at 50 W for 5 min to distribute the BMs adequately. BMs were then incubated with Ara-C by sonication (50 W, 5 min). Following the addition of GP solution (0.5%), the mixture was distributed by ultrasonic bathing for ten times (50 W, each lasted for 1 min with an interval of 5 min). The mixture was then placed in an incubator shaker with provided conditions (60 rpm, 37°C for 72 h). The resultant ABMs-GP was derived from the blend by magnet and then washed carefully with PBS (pH 7.4). Other designs such as ABMs-G and ABMs were obtained through the same above discussed process, but the only change is by using G and no cross-linker, respectively.

2.3. Physical Characterization. Transmission electron microscope (TEM) images were captured following the procedure

TABLE 1: Zeta potentials of BMs, ABMs-GP, ABMs-G, and ABMs.

Sample	BMs	ABMs-GP	ABMs-G	ABMs
Zeta potential (mV)	-11.5 ± 0.3	-29.1 ± 1.7	-34.6 ± 3.0	-35.9 ± 2.7

for preparing samples. The prepared complexes were washed with PBS and distilled water for many times, followed by being suspended in distilled water using an ultrasonic bathing. Further, the BMs and the previous complex supernatants (15–20 μL) were dropped on the copper grids. After being dried, all grids were observed under the TEM. In addition, surface charge measurements were performed using Zetasizer. The samples were suspended in water, and 1 mL of suspension was subjected to record the surface charge using Zetasizer analyser (ZEN 3600; Malvern Instruments, Ltd., Malvern, UK). All assays were performed in triplicate, and the DTS5.00 for windows was used for statistical analysis.

2.4. Examination by FTIR Spectrometer. To elucidate the functional groups attached, Fourier transform infrared (FT-IR) spectra were recorded on NICOLET iS10, Thermo Fisher Scientific spectrometer at a scanning range of 4000–400 cm^{-1} . Samples were prepared using a dried KBr pellet method.

2.5. Evaluation of the Amount of Ara-C Immobilized to BMs. Appropriate sample suspension was taken out and dissolved in 4.8 mL breaking-membrane liquid composed of 37% hydrochloric acid and 70% ethanol solution ($v/v = 1:2$) for 1 h. The number of Ara-C loaded with BMs was calculated based on a standard curve for Ara-C in breaking-membrane liquid: $Y = 24.4764X + 0.3134$ ($R^2 = 0.9994$), where Y is the concentration of Ara-C ($\mu\text{g}/\text{mL}$) and X is the absorbance of Ara-C in membrane-breaking liquid measured at 283.5 nm.

2.6. In Vitro Drug Release Study. The tests of Ara-C released from various samples were performed by placing the sample containing tubes in an incubator shaker at 60 rpm, 37°C with magnet absorption. The resultants were diluted into PBS at pH 7.4 and incubated for 0.5, 1, 12, 24, 36, or 48 h. At settled time points, the absorption value of Ara-C in the supernatant was measured at 271.4 nm using U-vis spectrophotometer. The concentration of Ara-C was determined using a standard curve: $Y = 26.0769X - 0.0625$ ($R^2 = 0.9999$), where Y is the concentration of Ara-C ($\mu\text{g}/\text{mL}$) and X is the absorption of Ara-C in PBS at 271.4 nm. All assays were performed in triplicate.

3. Results and Discussion

3.1. Immobilization of Ara-C on BMs. The commonly used method to prepare BMs-based conjugates was through amine-amine linkage [28]. We investigated various approaches to couple Ara-C with BMs using different cross-linkers. Figure 1 depicts the TEM image observations elucidating the surface morphology of BMs-based conjugates. A distinct membrane outside of BMs is clearly visible and it is

noteworthy that various conjugates (Figures 1(b)–1(d)) look like they were covered by thickened and blurred materials, which is absent in BMs (Figure 1(a)). This infers that Ara-C is loaded onto the surface of BMs.

The surface charge of nanoconjugates plays a key role in elucidating the drug loading efficiency. As shown in Table 1, the zeta potential values of all drug conjugates were significantly lower than that of BMs (-11.5 ± 0.3 mV). The changes indicate that Ara-C is successfully loaded onto the BMs. This phenomenon could be the occupying of positively charged groups in the membrane. The results also show that the resultant conjugates are stable in aqueous solution.

3.2. Examination by FTIR Spectrometer. FTIR spectra were recorded to characterize the chemical groups and surface modifications within the modified samples. The FTIR spectra of Ara-C, ABMs-GP, ABMs-G, ABMs, and BMs samples are shown in Figure 2. The main characteristic absorption peaks of BMs were at 3435, 2925, 1724, 1635, 1563, 1057, and 589 cm^{-1} . The NH_2 stretching vibration should appear at 3435 and 1563 cm^{-1} . The peaks at 1724 and 1635 cm^{-1} were assigned to C=O and C=C stretching vibration. The absorption peaks observed at 1057 cm^{-1} represents the phosphate stretching vibration signals. The weak absorption peak at 589 cm^{-1} was assigned to the typical Fe-O stretching vibration [29].

It is notable that the FTIR of ABMs-GP showed weaker absorbance at both 3435 and 1568 cm^{-1} than that of BMs, due to the reduction of amino groups on ABMs-GP, while the stronger absorbance peak at 1728 cm^{-1} also was found, which represents the introduction of carbonyl groups [21]. The absorption peak at 809 cm^{-1} assigned to Ara-C was found in ABMs-GP. Additionally, the FTIR of ABMs-G showed stronger absorbance peak at 1059 and 1634 cm^{-1} . Moreover, contrary to the BMs, both the FTIR of ABMs and Ara-C showed absorbance peak at 809 cm^{-1} . All these data manifested that Ara-C is loaded on to BMs membrane via different cross-linkers.

3.3. Evaluation of the Amount of Ara-C Immobilized to BMs. It is well known that high coupling efficiency can facilitate the therapy. Figure 3 depicts that the amount of Ara-C coupled to BMs changes over cross-linking methods. The drug loading of ABMs is much higher than that of previous study [30]. The high drug loading may be due to the abundant amine groups and narrow size distribution. Most important is that direct absorption methods exhibited the highest coupling efficacy and encapsulation efficiency within the experiment, owing to the high surface to volume ratio of BMs [31]. Nevertheless, the drug loading of ABMs-GP and ABMs-G by covalent cross-linking is lower than that of ABMs; it may be because the reaction process is affected by various other factors such as pH, temperature, and concentration. In this paper, we

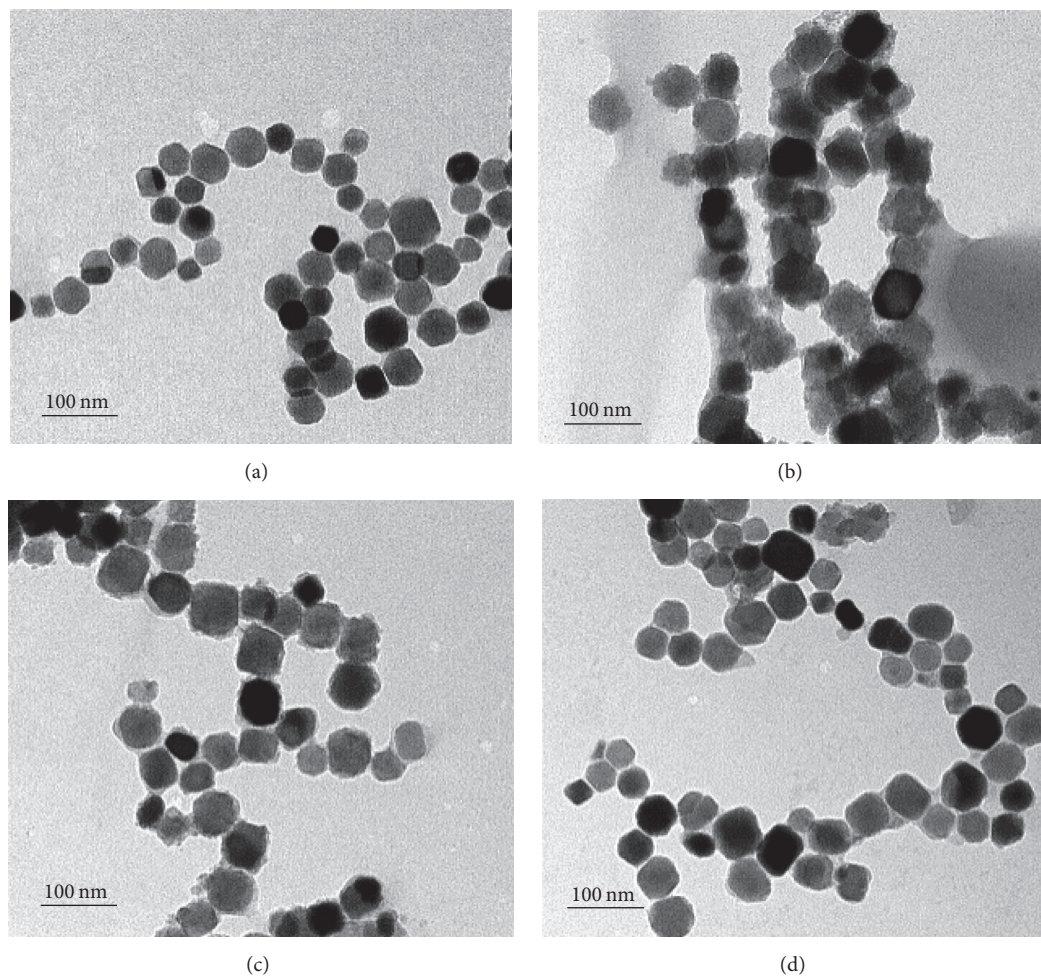


FIGURE 1: TEM images of BMs (a), ABMs-GP (b), ABMs-G (c), and ABMs (d).

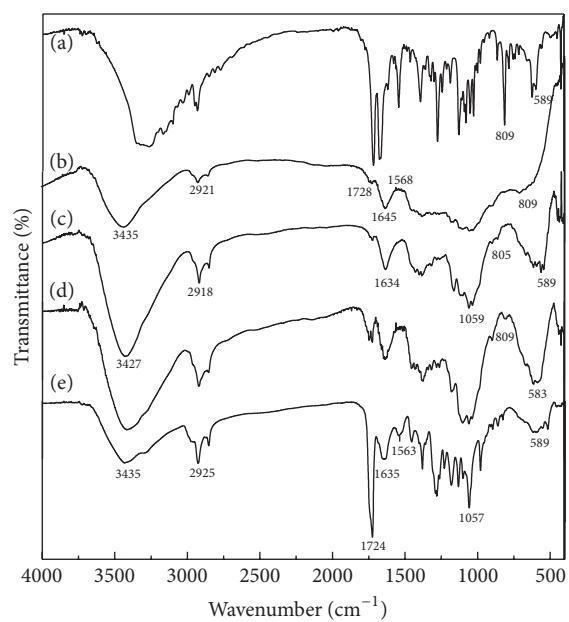


FIGURE 2: The FTIR spectra of (a) Ara-C, (b) ABMs-GP, (c) ABMs-G, (d) ABMs, and (e) BMs.

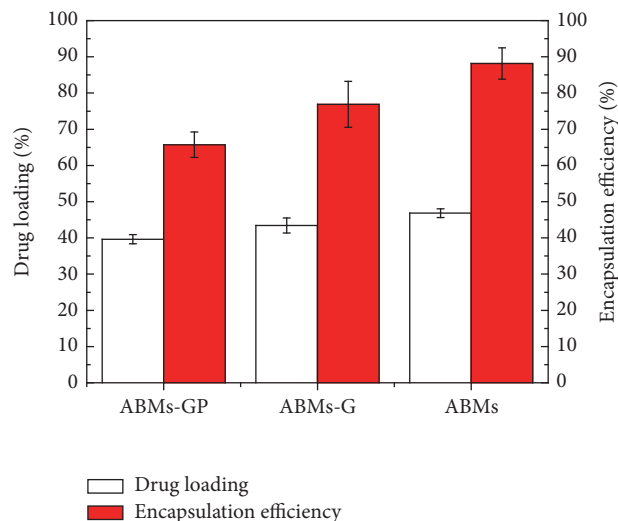


FIGURE 3: Drug loading and encapsulation efficiency of ABMs-GP, ABMs-G, and ABMs.

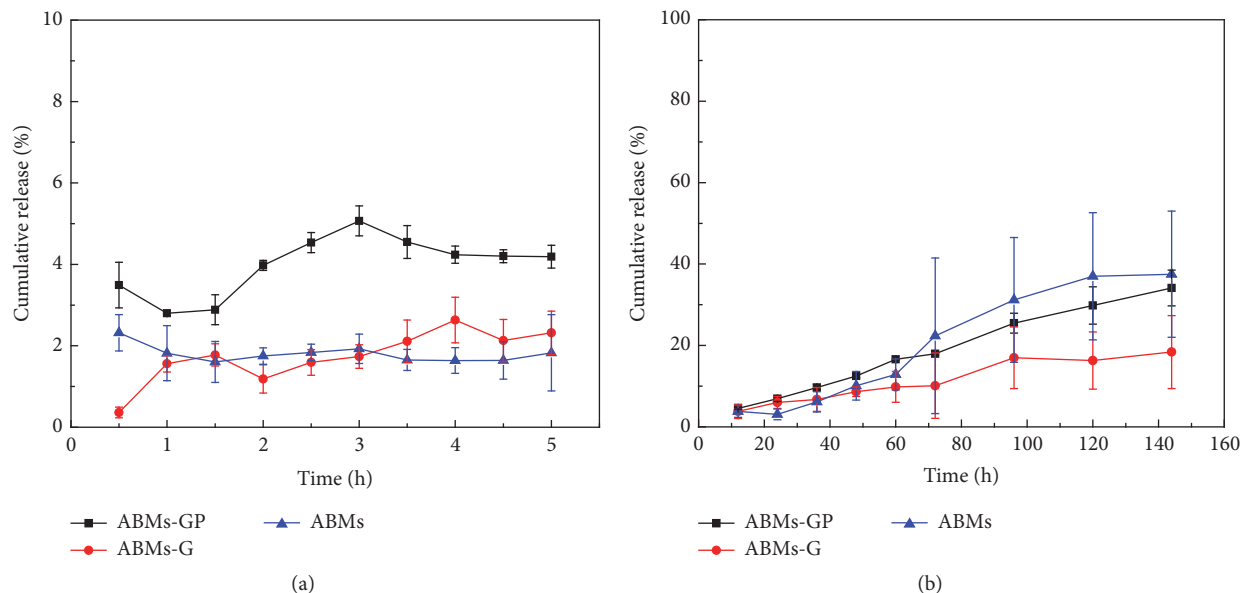


FIGURE 4: The cumulative release of compounds with different preparation methods in vitro (a) before 5 hours and (b) after 5 hours.

selected the optimum condition of our previous study [20]. The other factor is the steric effect of intermolecular reaction, which inhibits the experiment process. The results of drug loading are consistent with that of zeta potentials.

3.4. In Vitro Drug Release. The release of Ara-C from BMs-based conjugates was assayed by suspending them in PBS (pH 7.4) to mimic pH of blood plasma [32]. As shown in Figure 4, drug burst release behavior was not observed in the initial half an hour. Ara-C releases slowly and lower than 40% of the original drug after incubation for 140 h. This phenomenon indicates that BMs-based conjugates are endowed with a long-term release property. Ara-C was released more readily from ABMs-G than that of ABMs-GP and ABMs (Figure 4(b)). The reason may be attributed to

the fact that intermolecular forces of direct absorption are weaker than covalent cross-linking. However, at the first 5 hours (Figure 4(a)), the cumulative release of ABMs was a little slower, which may be a compromise result of the highest drug loading and the relatively higher release amount.

4. Conclusions

In summary, Ara-C was immobilized on BMs efficiently by using GP, G, and direct absorption. Direct absorption shows the highest drug loading of $46.9 \pm 1.2\%$. In comparison with different conjugates, ABMs shows better dispersion and much more stable long-term release property. Our study provides a theoretical basis for cross-linking method to reduce the amount of drug and improve the therapy efficiency.

Conflicts of Interest

The authors declare that they have no conflicts of interest.

Acknowledgments

Financial support from NSFC (31000441 and 31170939), National Marine Economic Innovation and Development Project (16PYY007SF17), the Science Research Foundation of National Health and Family Planning Commission of PRC & United Fujian Provincial Health and Education Project for Tackling the Key Research (WKJ2016-2-22), the Program for New Century Excellent Talents in Fujian Province University (2014FJ-NCET-ZR01), and the Promotion Program for Young and Middle-Aged Teachers in Science and Technology Research of Huaqiao University (ZQN-PY108) is gratefully acknowledged.

References

- X. Y. Zhang and P. Y. Zhang, "Nanotechnology for multimodality treatment of cancer," *Oncology Letters*, vol. 12, pp. 4883–4886, 2016.
- J. Hu, Y. Tang, A. H. Elmenoufy, H. Xu, Z. Cheng, and X. Yang, "Nanocomposite-based photodynamic therapy strategies for deep tumor treatment," *Small*, vol. 11, no. 44, pp. 5860–5887, 2015.
- A. Wicki, D. Witzigmann, V. Balasubramanian, and J. Huwyler, "Nanomedicine in cancer therapy: challenges, opportunities, and clinical applications," *Journal of Controlled Release*, vol. 200, pp. 138–157, 2015.
- R. K. Kankala, Y. Kuthati, C. L. Liu et al., "Killing cancer cells by delivering a nanoreactor for inhibition of catalase and catalytically enhancing intracellular levels of ROS," *RSC Advances*, vol. 5, no. 105, pp. 86072–86081, 2015.
- N. Morimoto, M. Wakamura, K. Muramatsu et al., "Membrane translocation and organelle-selective delivery steered by polymeric zwitterionic nanospheres," *Biomacromolecules*, vol. 17, no. 4, pp. 1523–1535, 2016.
- D. Colmenares, Q. Sun, P. Shen, Y. Yue, D. J. McClements, and Y. Park, "Delivery of dietary triglycerides to caenorhabditis elegans using lipid nanoparticles: nanoemulsion-based delivery systems," *Food Chemistry*, vol. 202, pp. 451–457, 2016.
- P. S. Apaolaza, A. del Pozo-Rodríguez, M. A. Solinís et al., "Structural recovery of the retina in a retinoschisin-deficient mouse after gene replacement therapy by solid lipid nanoparticles," *Biomaterials*, vol. 90, pp. 40–49, 2016.
- L. Rodriguez-Arco, I. A. Rodriguez, V. Carriel et al., "Biocompatible magnetic core-shell nanocomposites for engineered magnetic tissues," *Nanoscale*, vol. 8, no. 15, pp. 8138–8150, 2016.
- S. Yook, Y. Lu, J. J. Jeong et al., "Stability and biodistribution of thiol-functionalized and ¹⁷⁷Lu-labeled metal chelating polymers bound to gold nanoparticles," *Biomacromolecules*, vol. 17, no. 4, pp. 1292–1302, 2016.
- T. Song, H. Cheng, C. Fu et al., "Influence of the active layer nanomorphology on device performance for ternary PbS_xSe_{1-x} quantum dots based solution-processed infrared photodetector," *Nanotechnology*, vol. 27, no. 16, Article ID 165202, 2016.
- S. Chen, X. Hao, X. Liang et al., "Inorganic nanomaterials as carriers for drug delivery," *Journal of Biomedical Nanotechnology*, vol. 12, no. 1, pp. 1–27, 2016.
- X. Li, J. Wei, K. E. Aifantis et al., "Current investigations into magnetic nanoparticles for biomedical applications," *Journal of Biomedical Materials Research Part A*, vol. 104, no. 5, pp. 1285–1296, 2016.
- H. Liu, J. Zhang, X. Chen et al., "Application of iron oxide nanoparticles in glioma imaging and therapy: from bench to bedside," *Nanoscale*, vol. 8, no. 15, pp. 7808–7826, 2016.
- S. Wang, W. T. Yang, H. L. Du et al., "Multifunctional reduction-responsive SPIO&DOX-loaded PEGylated polymeric lipid vesicles for magnetic resonance imaging-guided drug delivery," *Nanotechnology*, vol. 27, no. 16, Article ID 165101, 2016.
- G. Lin, W. Zhu, L. Yang et al., "Delivery of siRNA by MRI-visible nanovehicles to overcome drug resistance in MCF-7/ADR human breast cancer cells," *Biomaterials*, vol. 35, no. 35, pp. 9495–9507, 2014.
- M. Boucher, F. Geffroy, S. Prévèral et al., "Genetically tailored magnetosomes used as MRI probe for molecular imaging of brain tumor," *Biomaterials*, vol. 121, pp. 167–178, 2017.
- C. Chen, P. Wang, and L. Li, "Applications of bacterial magnetic nanoparticles in nanobiotechnology," *Journal of Nanoscience and Nanotechnology*, vol. 16, no. 3, pp. 2164–2171, 2016.
- A. C. V. Araujo, F. Abreu, K. T. Silva, D. A. Bazylinski, and U. Lins, "Magnetotactic bacteria as potential sources of bioproducts," *Marine Drugs*, vol. 13, no. 1, pp. 389–430, 2015.
- A. S. Mathuriya, "Magnetotactic bacteria for cancer therapy," *Biotechnology Letters*, vol. 37, no. 3, pp. 491–498, 2015.
- Y.-G. Liu, Q.-L. Dai, S.-B. Wang, Q.-J. Deng, W.-G. Wu, and A.-Z. Chen, "Preparation and in vitro antitumor effects of cytosine arabinoside-loaded genipin-poly-L-glutamic acid-modified bacterial magnetosomes," *International Journal of Nanomedicine*, vol. 10, pp. 1387–1397, 2015.
- Q. Deng, Y. Liu, S. Wang et al., "Construction of a novel magnetic targeting anti-tumor drug delivery system: cytosine arabinoside-loaded bacterial magnetosome," *Materials*, vol. 6, no. 9, pp. 3755–3763, 2013.
- N. Nakamura, K. Hashimoto, and T. Matsunaga, "Immunoassay method for the determination of immunoglobulin G using bacterial magnetic particles," *Analytical Chemistry*, vol. 63, no. 3, pp. 268–272, 1991.
- L. Xiang, W. Bin, J. Huali et al., "Bacterial magnetic particles (BMPs)-PEI as a novel and efficient non-viral gene delivery system," *Journal of Gene Medicine*, vol. 9, no. 8, pp. 679–690, 2007.
- T. Matsunaga and S. Kamiya, "Use of magnetic particles isolated from magnetotactic bacteria for enzyme immobilization," *Applied Microbiology and Biotechnology*, vol. 26, no. 4, pp. 328–332, 1987.
- Y. Liu, M. Xie, S. Wang, Q. Zheng, A. Chen, and Q. Deng, "Facile fabrication of high performances MTX nanocomposites with natural biomembrane bacterial nanoparticles using GP," *Materials Letters*, vol. 100, pp. 248–251, 2013.
- L. Guo, J. Huang, and L.-M. Zheng, "Control generating of bacterial magnetic nanoparticle-doxorubicin conjugates by poly-L-glutamic acid surface modification," *Nanotechnology*, vol. 22, no. 17, Article ID 175102, 2011.
- R. M. Long, Y. G. Liu, Q. L. Dai et al., "A natural bacterium-produced membrane-bound nanocarrier for drug combination therapy," *Materials*, vol. 9, no. 11, p. 889, 2016.
- J. Sun, Y. Li, X.-J. Liang, and P. C. Wang, "Bacterial magnetosome: a novel biogenetic magnetic targeted drug carrier with potential multifunctions," *Journal of Nanomaterials*, vol. 2011, Article ID 469031, 13 pages, 2011.

- [29] J.-B. Sun, J.-H. Duan, S.-L. Dai et al., "Preparation and anti-tumor efficiency evaluation of doxorubicin-loaded bacterial magnetosomes: magnetic nanoparticles as drug carriers isolated from *Magnetospirillum gryphiswaldense*," *Biotechnology and Bioengineering*, vol. 101, no. 6, pp. 1313–1320, 2008.
- [30] L. Guo, Ji Huang, X. Zhang, Y. Li, and L. Zheng, "Bacterial magnetic nanoparticles as drug carriers," *Journal of Materials Chemistry*, vol. 18, no. 48, pp. 5993–5997, 2008.
- [31] C. F. Chen, P. P. Wang, and L. L. Li, "Applications of bacterial magnetic nanoparticles in nanobiotechnology," *Journal of Nanoscience & Nanotechnology*, vol. 16, no. 3, pp. 2164–2171, 2016.
- [32] M. F. Wang, T. X. Liu, L. Q. Han et al., "Functionalized O-carboxymethyl-chitosan/polyethylenimine based novel dual pH-responsive nanocarriers for controlled co-delivery of DOX and genes," *Polymer Chemistry*, vol. 6, no. 17, pp. 3324–3335, 2015.

Research Article

Preparation and Characterization of a Tumor-Targeting Dual-Image System Based on Iron Oxide Nanoparticles Functionalized with Folic Acid and Rhodamine

Alejandra Ancira-Cortez,¹ Enrique Morales-Avila,¹
Blanca E. Ocampo-García,² Carlos González-Romero,¹ Luis A. Medina,^{3,4}
Gustavo López-Téllez,⁵ and Erick Cuevas-Yáñez⁵

¹Facultad de Química, Universidad Autónoma del Estado de México, 50120 Toluca, MEX, Mexico

²Instituto Nacional de Investigaciones Nucleares, Departamento de Materiales Radiactivos, 52750 Ocoyoacac, MEX, Mexico

³Instituto de Física, Universidad Nacional Autónoma de México, 04510 Ciudad de México, Mexico

⁴Unidad de Investigación Biomédica en Cáncer INCan-UNAM, Instituto Nacional de Cancerología, 14080 Ciudad de México, Mexico

⁵Centro Conjunto de Investigación en Química Sustentable UAEM-UNAM, Universidad Autónoma del Estado de México, Toluca, MEX, Mexico

Correspondence should be addressed to Enrique Morales-Avila; emoralesav@uaemex.mx

Received 25 January 2017; Accepted 2 April 2017; Published 30 April 2017

Academic Editor: Murtaza Bohra

Copyright © 2017 Alejandra Ancira-Cortez et al. This is an open access article distributed under the Creative Commons Attribution License, which permits unrestricted use, distribution, and reproduction in any medium, provided the original work is properly cited.

Cancer is one of the diseases with most deaths worldwide, around 8.2 million annually. For this reason, several treatments and diagnostic tools have been investigated and developed over the past decades. Among them, a dual-image system has been developed to achieve and enhance the detection of cancer, which has not been done with systems currently available. The present study describes the preparation of a dual-image targeting system composed of magnetic iron oxide nanoparticles functionalized with folic acid and rhodamine; nanoparticles synthesis was achieved by a coprecipitation method; the functionalization was carried out by a carbodiimide with folic acid and/or the rhodamine isothiocyanate; conjugates were characterized by spectrometric techniques; toxicity was measured by cell proliferation assay on HeLa cells using progressive concentrations of functionalized nanoparticles. Cellular uptake assay was carried out by competitive assay on HeLa cells. Iron oxide magnetite nanoparticles, modified with folic acid and rhodamine, were successfully synthesized with a particle size lower than 20 nm (TEM), EDS, HRTEM, and XDR showed highly crystalline Fe₃O₄ nanoparticles. Folic acid and rhodamine were conjugated with high efficiency. A significant selectivity and uptake, facilitated by surface modification of iron oxide nanoparticles with folic acid, were demonstrated. The multifunctional system showed suitable physicochemical and biological properties for cell targeting through folate receptors.

1. Introduction

Molecular imaging comprises the noninvasive monitoring of functional and spatiotemporal processes at cellular, subcellular, or molecular levels in humans and other living systems. Although molecular imaging has existed for decades, recent advances in molecular and cell biology, imaging technology, and material sciences have greatly increased its power and potential as specific and sensitive medical tools [1].

Nanoparticles (NPs) are submicron moieties with diameters ranging from 1 to 100 nm, depending on their intended

purpose, which have many novel physical and chemical properties that are not present in the atom nor the bulk counterpart, related to the dimensions and shape, as well as morphology [2, 3]; NPs have been used in many different biological and medical applications as key components for imaging probe design [4–7].

Iron oxide nanoparticles (IONPs) of magnetite type (Fe₃O₄) have desirable physical and biochemical characteristics (e.g., superparamagnetism, high coercivity, low Curie temperature (T_C), high magnetic susceptibility, chemical stability in physiological conditions, high saturation fields,

biocompatibility, and biodegradable and nontoxic nature), which make them useful in the diagnosis and treatment in the oncology field [8–10].

A desirable molecular imaging probe must be able to reach specific targets with high affinity, sensitivity, and suitable biodistribution properties. Nanoparticle-based molecular imaging probes can be functionalized or modified due to their high surface area-to-volume ratio, by bioactive molecules, typically through chemical coupling *via* amide or ester bonds in order to reach a target site. Some of the molecules used as targeting elements include small ligands, antibodies and derivatives, aptamers and other nucleic acids, polyunsaturated fatty acids, peptides, and proteins [2, 11–13]. Furthermore, surface modification can include fluorescence dyes, genes, or drugs, to provide multimodal functionalities [3].

Folic acid (FA) is a water-soluble vitamin, can be easily conjugated to supramolecular and macromolecular structures, and has been used as a vector for cancer cells targeting due to its high affinity ($K_d \sim 10^{-10}$ mM) for its corresponding folate receptors (FRs: FR $_{\alpha}$, FR $_{\beta}$, and FR $_{\gamma}$), to mediate cellular uptake of FA [12, 14–18].

FRs are overexpressed in a large number of cancer cells and are positively associated with tumor stage and histologic grade (e.g., ovarian cancer, endometrial cancer, kidney cancer, colorectal cancer, lung cancer, breast cancer, brain cancer, and myeloid leukemia); FRs provide a special marker that distinguishes cancer cells from normal cells, as these exhibit limited expression, are largely restricted to those important for embryonic development (e.g., placenta and neural tubes), and present low levels in folate resorption through kidney and lung. It has been reported that folate conjugation to the IONPs enhances the cellular uptake to target cells, improving therapeutic efficacy [12, 17–21].

Rhodamine B isothiocyanate, on the other hand, is a fluorophore that belongs to the xanthene dyes family. Due to its photophysical properties and excellent photostability, it is used as fluorescence probes for imaging sensor techniques. Optical imaging allows noninvasive drug visualization in cells and tissues in order to understand molecular processes in real time. Specifically, it has been reported that several MNPs (magnetic nanoparticles) can be used as dual-modality imaging probes, in nuclear and optical fluorescence imaging which is the case of IONPs [22–25].

Therefore, we aimed to develop a tumor-targeting dual-image system based on IONPs with folic acid as a vector and rhodamine isothiocyanate as an imaging agent, primarily designed for noninvasive monitoring, in order to acquire high-quality targeted images without cytotoxicity to normal cells.

2. Materials and Method

All chemicals were of analytical grade from commercial sources used without further purification. Ferric chloride hexahydrate (FeCl $_3$ ·6H $_2$ O), ferrous chloride tetrahydrate (FeCl $_2$ ·4H $_2$ O), folic acid, *N*-(3-dimethylaminopropyl)-*N'*-ethylcarbodiimide hydrochloride (EDC), 4-(dimethylamino)pyridine (DMAP), 2-aminoethylphosphonic acid (2-AEP), and rhodamine B isothiocyanate mixed isomers

(RITC) were purchased from Sigma-Aldrich® Chemical Co. (St. Louis, MO, USA). Folate-free RPMI-1640 medium, bovine fetal serum, NaHCO $_3$, antibiotic-antimycotic solution (100x) containing penicillin, streptomycin, and amphotericin, and other chemicals and solvents were of reagent grade. The HeLa cell line was obtained from the National Institute of Cancerology, Mexico.

2.1. Synthesis of Magnetic Iron Oxide Nanoparticles (IONPs) and Surface Activation. Bare magnetic iron oxide nanoparticles were synthesized by an alkaline coprecipitation of Fe $^{3+}$ and Fe $^{2+}$, in agreement with Banerji et al., [26]. For surface activation, a freshly prepared aqueous solution of 2-AEP (1 mM) was added to 4 mM of a colloidal suspension of NPs with sonication using a high-intensity ultrasonic probe during an hour. Then, the resulting nanoparticle suspension was stirred vigorously at 25°C for 24 h. The particles were then washed with deionized water three times *via* magnetic decantation and finally dried by evaporation at 37°C. Samples were stored for posterior use (see Figure 1(a)).

2.2. Synthesis of the Iron Oxide Folate Conjugate (IONPs-FA). Magnetic iron oxide NPs were modified with folic acid (FA) using a solution of FA (2.5 mM) in 5 mL of dichloromethane (DCM). The solution was mixed with an ethanolic solution of *N*-(3-dimethylaminopropyl)-*N'*-ethylcarbodiimide (EDC) (75 mM) and 4-(dimethylamino) pyridine (DMAP) (15 mM). Afterwards, the solution was sonicated using a high-intensity ultrasound probe during 2 h. The solution was allowed to stand overnight. Posteriorly, the solution was stirred vigorously at 25°C during 24 h, and the IONPs were recovered and washed *via* magnetic decantation, using ethanol and deionized water as diluents (see Figure 1(b)). The product was stored for use in the subsequent steps.

2.3. Synthesis of Amine-Functionalized Magnetofluorescent RITC Nanoparticles (IONPs-RITC). An aqueous suspension of 2-AEP-functionalized IONPs (~25 mg) was prepared and homogenized using a high-intensity ultrasound probe for 10 min. Then, RITC (0.25 mM) was dissolved in 10 mL of DMSO, and the solution of RITC was added dropwise to the aqueous suspension. Once the mixture was complete, the resulting suspension was sonicated for an hour in the dark. Nanoparticles were recovered by magnetic concentration and washed thoroughly with deionized water; samples were stored for posterior use.

2.4. Synthesis of Iron Oxide Folate Fluorescent Nanoparticles (FA-IONPs-RITC). To create the multifunctional system, ~1.3 mg of RITC (0.25 mM) was dissolved in 10 mL of DMSO. Then, the solution was added dropwise in the dark to the previous iron oxide folate suspension (IONPs-FA). The resulting suspension was sonicated during an hour. After that, the system was thoroughly washed with deionized water *via* magnetic concentration and stored for posterior use (see Figure 1(c)).

2.4.1. Size and Morphology. Nanoparticles were analyzed by TEM in a JEOL JEM 2010 HT microscope operating at

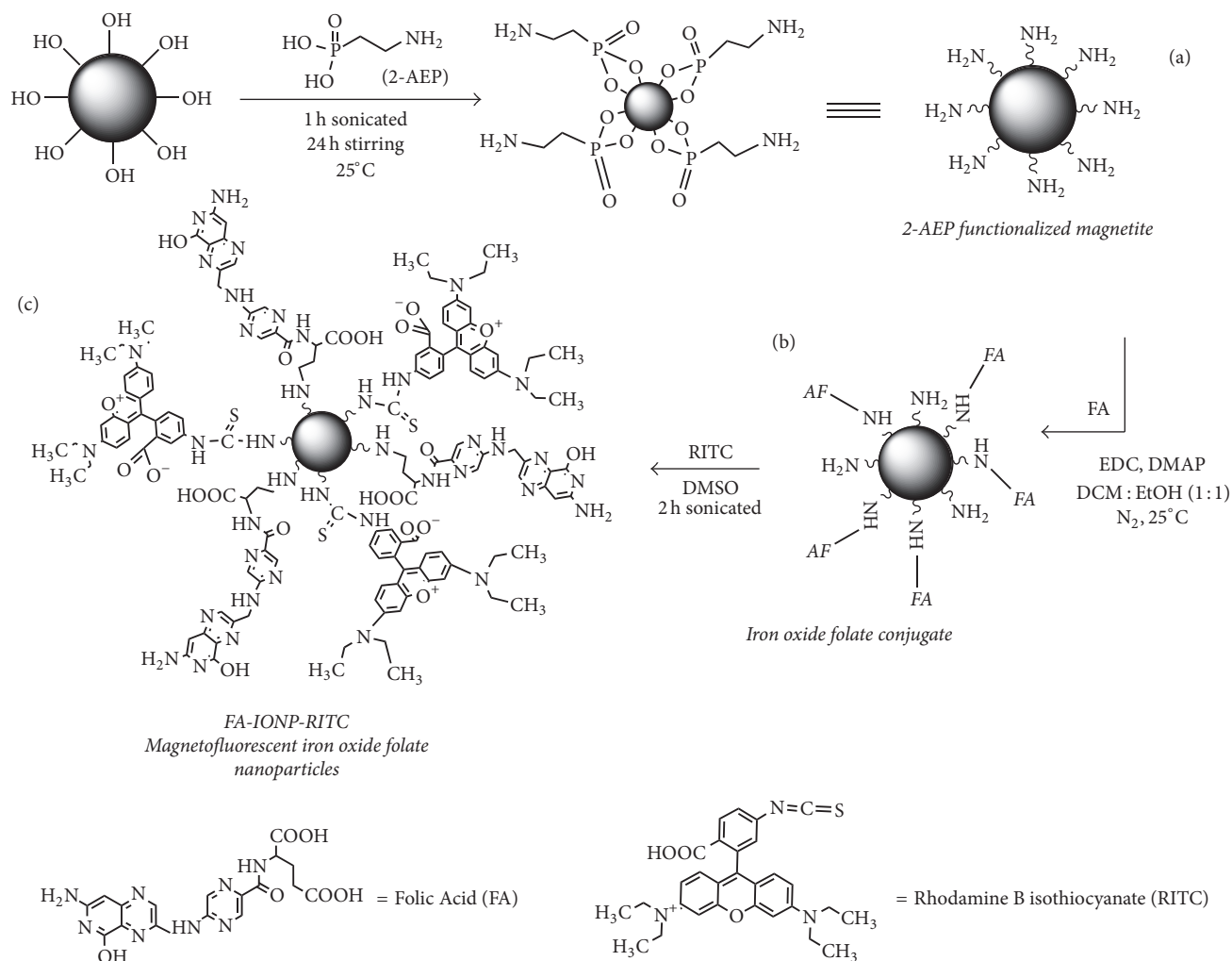


FIGURE 1: Schematic synthesis of amine-functionalized magnetite nanoparticles: (a) the surface of IONPs was modified with 2-AEP to form an amine-functionalized phosphonate monolayer, and (b) folic acid/rhodamine isothiocyanate were conjugated through the carbodiimide reaction, in order to obtain FA-IONPs-RITC.

200 kV in order to observe the two-dimensional relative size and morphology of nanoparticles. Samples were prepared for analysis by evaporating a drop of aqueous product on a carbon-coated TEM copper grid. At least 1000 nanoparticles were measured using the Image J software, to determine the mean diameter of nanoparticles.

2.4.2. X-Ray Diffraction. X-ray diffraction (XRD) patterns of naked iron oxide cores were recorded on a powder diffractometer Bruker D8 Advance to characterize the crystallite type. Sample was centered with magnetic decantation and dried by evaporation at room temperature and high vacuum. After that, sample was removed and desiccated thoroughly over dried silica gel and posteriorly screened with the goniometer at 2θ angles from 5° to 80° at a step width of 0.03° .

2.4.3. Infrared Spectroscopy. The IR spectra were acquired from vacuum-dried samples on a PerkinElmer System 2000 spectrometer with an ATR platform (Pike Technologies) by

applying the Attenuated Total Reflection Fourier Transform Infrared (ATR-FTIR) spectroscopy with a 4 cm^{-1} resolution, 40 scans, and operating range at $4000\text{--}40\text{ cm}^{-1}$.

2.4.4. UV-Vis Studies. The absorption spectra, in the range of $200\text{--}700\text{ nm}$, were obtained through a Thermo Genesys 10S spectrometer using a 1 cm quartz cuvette.

2.4.5. Fluorescence Spectroscopy. The emission fluorescence spectra, in the range of $450\text{--}750\text{ nm}$, were obtained through a Horiba Jobin Yvon Spectrofluorometer (Fluoromax-P) with dual excitation and emission monochromators in a wavelength range between 350 and 800 nm . Nanoparticles were measured with a λ_{exc} of 398 nm using a 1 cm cuvette. Three-/0.5-second scans were acquired.

2.4.6. Determination of the Concentration of FA Conjugated over the Surface of the IONPs. The number of FA molecules attached per nanoparticle was calculated by UV-Vis spectroscopy using different FA concentration (2.5 to 10.0 mM),

as in the carbodiimide reaction described in the experimental section. The concentration was calculated using the prepared standard curve ($r^2 = 0.9997$, with excellent linearity from 0.0125 mM to 15 mM). The experiments were conducted in triplicate.

2.4.7. Concentration of RITC Conjugated over the Surface of the IONPs. Conjugation was determined by titration using 0.0125 mM, 0.0375 mM, and 0.0625 mM RITC, employing the synthesis method described in the experimental section. Samples were washed with purified and deionized water, and the corresponding nanoparticles were measured by UV-Vis spectroscopy, calculating the concentration using the prepared rhodamine isothiocyanate standard curve ($r^2 \geq 0.9975$, with excellent linearity from 0.0033 mM to 0.0673 mM). The experiments were conducted in triplicate.

2.4.8. Cell Proliferation Studies/Nanoparticle-Induced Cytotoxicity. HeLa (human cervix adenocarcinoma) cells (1×10^4 cells/well) were seeded onto a 96-well plate and cultured in 200 μ L of folate-free RPMI medium containing 10% FBS, 100 units mL^{-1} penicillin, 100 $\mu\text{g mL}^{-1}$ streptomycin, and 0.25 $\mu\text{g mL}^{-1}$ amphotericin B at 37°C in a humidified 5%-CO₂/95%-air atmosphere and incubated for 24 h. The cells were treated with 20 μ L of different FA-IONPs-RITC nanoparticle concentrations (0.5 mg mL^{-1} , 0.25 mg mL^{-1} , 0.125 mg mL^{-1} , and 0.0625 mg mL^{-1}) and 180 μ L of media culture was added and incubated for 24 h at 37°C in a humidified incubator maintained at 5% CO₂/95% air atmosphere. Thereafter, cells were washed thoroughly with PBS to remove the noninternalized nanoparticles. Cell viability was evaluated using a crystal violet staining. Untreated cells served as 100% viable cells.

2.4.9. Cellular Uptake. Nanoparticle uptake by HeLa cells was evaluated using 5×10^5 cells/well seeded onto 24-well plates and cultured in a total volume of 2000 μ L of folate-free RPMI medium containing 10% FBS, 100 units mL^{-1} penicillin, 10 $\mu\text{g mL}^{-1}$ streptomycin, and 0.25 $\mu\text{g mL}^{-1}$ amphotericin B at 37°C in a humidified 5%-CO₂/95%-air atmosphere at 37°C in a humidified incubator maintained at 5%CO₂/95% air atmosphere. To test nanoparticle uptake *via* folate receptors, a group of HeLa cells were pretreated with 500 μ L of free folic acid (11 mg/mL) in order to saturate receptors and incubated at 37°C for 2 h. After receptor saturation, both blocked and nonblocked HeLa cells were treated with 40 μ L of IONPs (at a concentration of 0.25 mg mL^{-1}) eluted in PBS for 3 h, posteriorly supernatants were collected and measured by UV-Vis spectroscopy at 280 nm, and absorbances were extrapolated to FA calibration curve. Uptake percentage was calculated, using the baseline as untreated cells in the same conditions. The experiment was performed in triplicate. Finally the images for the cellular uptake test were obtained with an inverted confocal microscope, consisting of an Olympus IX80 with a Plan-Neofluar 40x, AxioVert (Carl Zeiss) objective, and an AxioVision software.

3. Results and Discussion

3.1. Size and Morphology. The coprecipitation method for obtaining magnetic iron oxide nanoparticles is one of the fastest and easiest methods for this purpose. Nanoparticles were synthesized in a molar ratio of Fe³⁺:Fe²⁺ of 2:1. Transmission electron microscopy (TEM) studies of IONPs revealed that the as-synthesized magnetite nanoparticles were closer to a spherical form and were uniform and homogeneous, which corresponds to that previously reported [26, 27].

The IONPs were obtained with a mean hydrodynamic diameter of 18.65 nm \pm 0.17 nm (Figure 2(a)). Size distribution showed a monomodal population; the frequency histogram is shown in Figure 2(b). The EDS patterns shown in (Figure 2(c)), diffraction from the samples consisting of fine particles, and the broad ring patterns from crystal planes attributed to Fe₃O₄ nanoparticles confirm the nucleus composition. Additionally, crystallographic High Resolution TEM (HRTEM) showed the highly crystalline Fe₃O₄ nanoparticles with the lattice fringes, corresponding to (220) and (111) planes of magnetite crystal with lattice spacing of 0.30 and 0.49 nm, respectively.

Evidence of identity and crystal structure was further verified by X-ray diffraction patterns (Figure 3). Intensity signals appeared at defined scattering angles 2θ with the most prominent ones at 18.26°, 30.05°, 35.54°, 43.11°, 53.42°, 56.92°, 62.63°, and 73.97° (Figure 2). The Bragg peaks could be assigned to specific diffraction planes inside the lattice: (111), (220), (311), (400), (422), (511), (440), and (533) corresponding to magnetite (Fe₃O₄), in agreement with JCPDS (16-0629).

3.2. FT-IR Studies

3.2.1. Iron Oxide Nanoparticles. The Far-IR and FT-IR (Mid) spectra of IONPs obtained showed the characteristic vibrations for the iron oxide material, in its magnetite phase (Figure 4(a)). For the first case (700–40 cm^{-1}), the medium-intense band at 345 cm^{-1} is attributed to the vibration of the magnetite core. The previously mentioned band has been previously reported to be specific for Fe₃O₄ [28]. In the second case, for the medium zone (4500–400 cm^{-1}), the expected vibrational bands were observed at 558 cm^{-1} and 3256 cm^{-1} . The first one corresponds to the specific Fe-O vibration of iron oxide nanoparticles, which confirms the material expected. The band at 3256 cm^{-1} was assigned to the -OH *st* vibration groups due to adsorbed water on the surface of the iron oxide nanoparticles [29, 30].

3.2.2. Amino-Modified Nanoparticles. The FT-IR of 2-AEP functionalized IONPs (Figure 4(b)) showed a strong band at 1026 cm^{-1} from the *st* vibration related to the overlapping of the signals which correspond to the vibrations of M-O-P, P=O, and the P-O bond. The band at 3361 cm^{-1} corresponds to the -NH₂ group *st* vibration, which is confirmed with the bending scissoring vibration present at 1631 cm^{-1} . These two bands confirm the presence of the amino-terminal groups

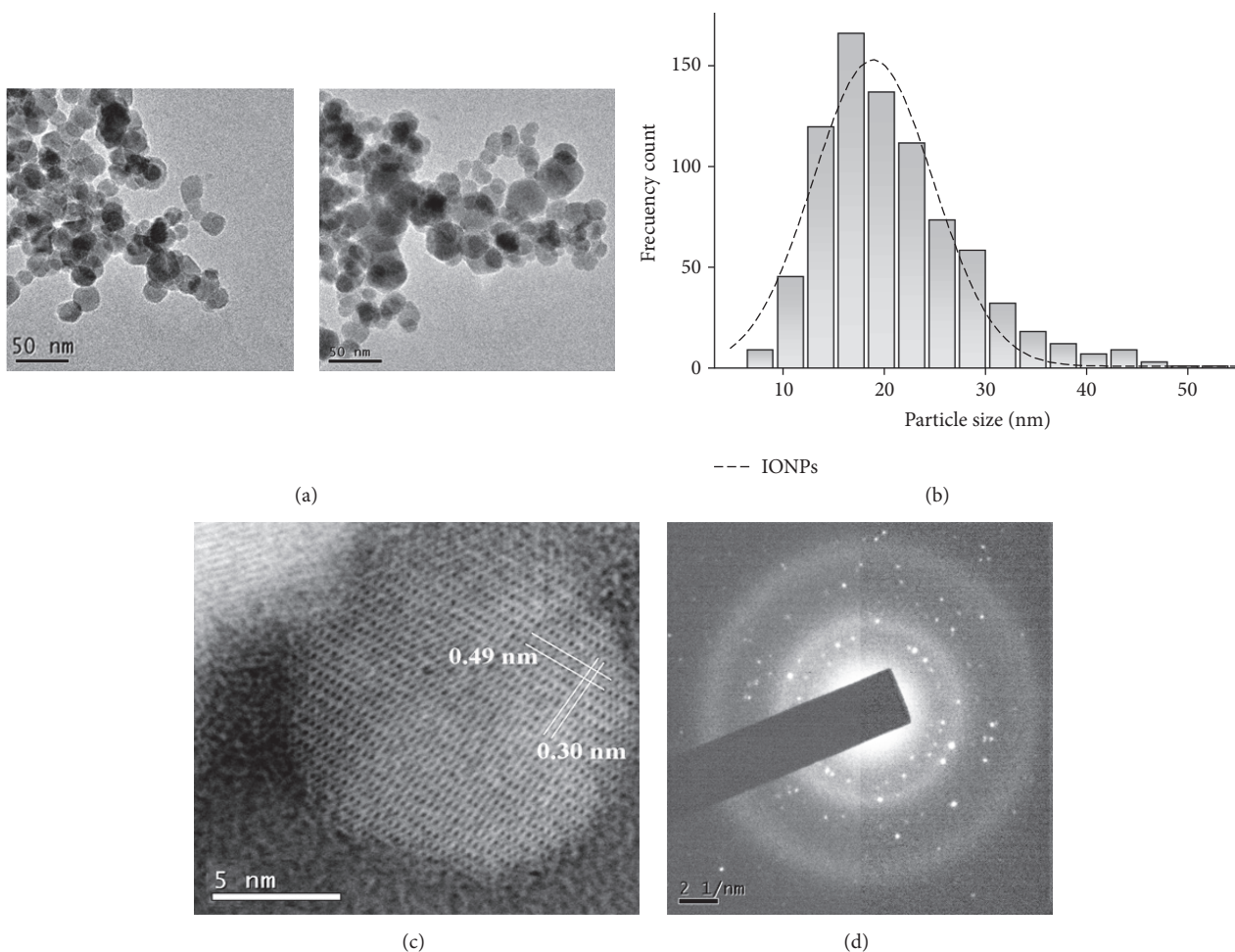


FIGURE 2: (a) TEM micrograph of unmodified magnetite nanoparticles; (b) particle size distribution (PSD) histogram and adjusted fit function; (c) HRTEM of a fine particle and (d) DR pattern attributed to the diffraction from the crystal planes of Fe_3O_4 nanoparticles.

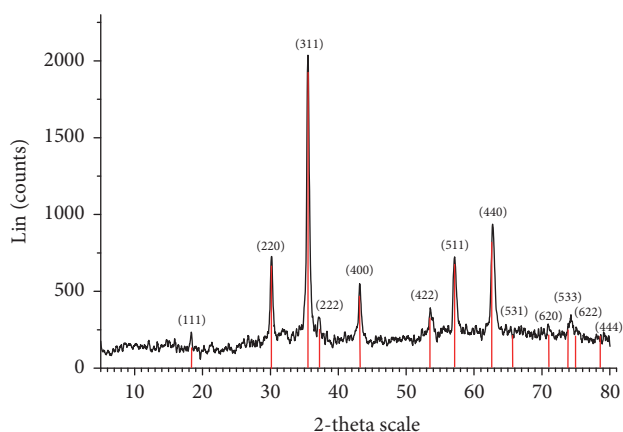


FIGURE 3: XRD pattern of prepared magnetite (Fe_3O_4) nanoparticles indicative of inverse spinel structure. Significant signals are assignable to diffraction planes (111), (220), (311), (222), (400), (422), (511), (440), and (533).

on the nanoparticle surface, which are necessary for the posterior functionalization. The peak for the magnetite core at 558 cm^{-1} shifts towards higher wavenumbers, to 570 cm^{-1} .

Also, a significant decrease in the intensity of this band was observed, which indicates the adsorption of phosphonic acids onto the magnetite surface.

3.2.3. IONPs-FA System. In the FT-IR spectrum of folate-conjugated nanoparticles (Figure 4(c)), the peak in the range of $3100\text{--}3500\text{ cm}^{-1}$ was assigned to the N-H *st* vibration from the $-\text{NH}_2$ and amine NH groups from folic acid. At 1648 cm^{-1} , the band present is related to the carbonyl group *st* vibration from amide and acidic groups, which exhibits less intensity and was shifted to $\sim 1700\text{ cm}^{-1}$, indicating that folic acid was successfully attached to the IONPs. The bands at 1606 cm^{-1} and 1548 cm^{-1} were assigned to the characteristic FA *st* vibrations (amide II and amide I, resp.), which indicate the successful conjugation to the nanoparticle surface. The presence of the new band at 1530 cm^{-1} was confirmed from the *st* vibration of the amide binding between $\text{Fe}_3\text{O}_4\text{-NH}_2\text{-FA}$, which indicates the formation of an extra amide bond attributed to the FA attachment onto the surface of IONPs, as well as the amide bands within the FA structure. Finally, it is important to mention that the vibration from the magnetite

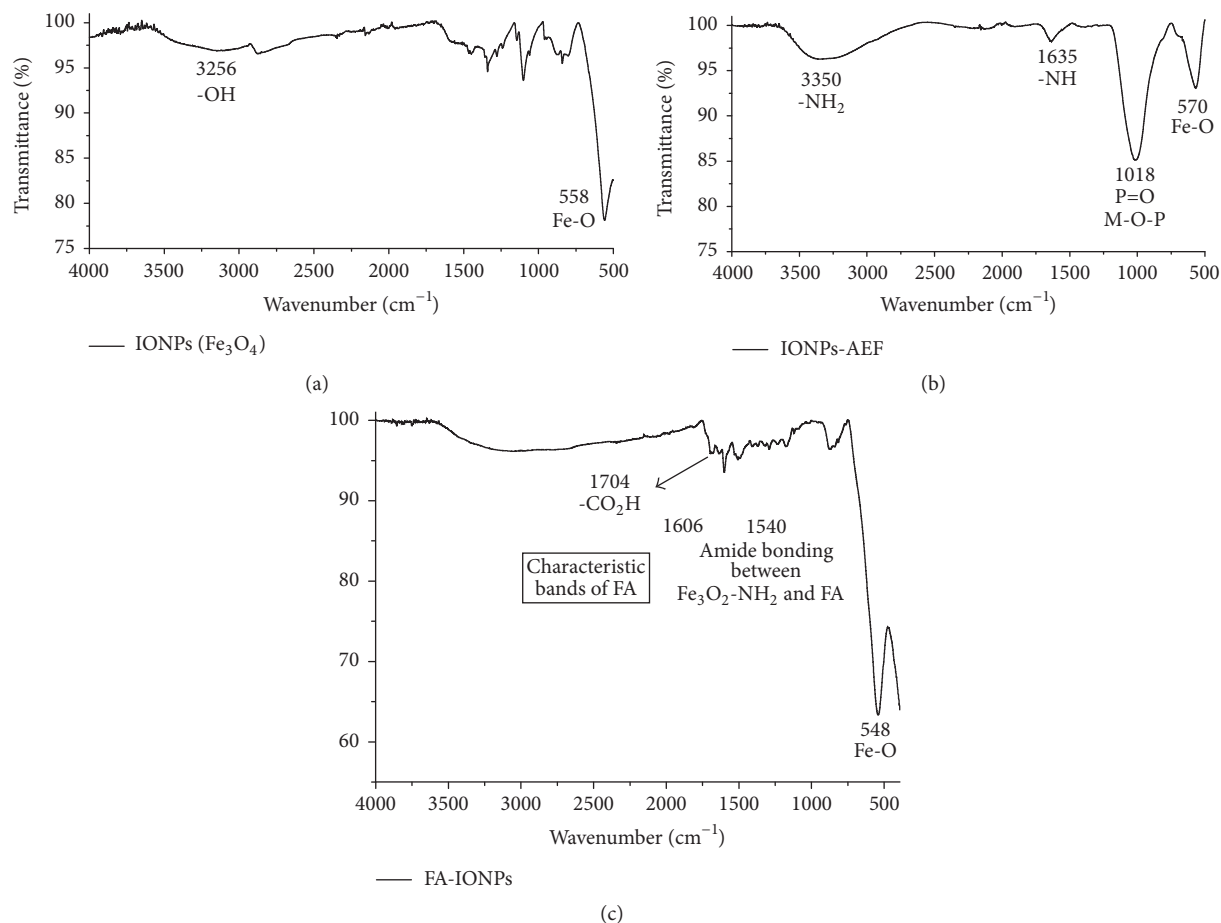


FIGURE 4: FT-IR spectra of (a) unmodified and amino-functionalized magnetite nanoparticles, (b) iron oxide folate conjugate nanoparticles, and (c) unmodified magnetite nanoparticles in far infrared.

core still appears at 548 cm^{-1} , which suggests that, even with the formation of the conjugate, the core does not suffer any important alteration [18].

3.3. UV-Vis Studies. The UV-Vis spectra from the unmodified magnetite, folic acid conjugate, rhodamine conjugate, folic acid/rhodamine magnetite nanoparticles, folic acid solution, and rhodamine solution have been depicted in the Figure 5(a). The magnetite core of the system, in the range 200–700 nm of the UV-Vis spectra, showed a characteristic band around 360 nm which demonstrated a suitable synthesis. The peak at $\sim 280 \text{ nm}$ was assigned to FA due to the well-known $\pi-\pi^*$ transitions from the pteridine ring moiety in the FA structure [31]. This UV-Vis band is present in the FA aqueous solution at 282 nm and in the IONPs-FA system at 283 nm. In the case of the FA-IONPs-RITC system, in which FA is also present, the band still appeared at 283 nm [29].

On the other hand, for the UV-Vis spectra for the same systems but focus on the RITC molecules, a band around 550 nm is present, which has been reported in previous works (536 nm for IONPs-RITC and 580 nm for FA-IONPs-RITC) [32], and although it is broad, the maximum absorption occurs in the same region.

3.4. Fluorescence Studies. In Figure 5(b), the fluorescence emission spectra from magnetite, folic acid conjugate, rhodamine conjugate, folic acid/rhodamine magnetite nanoparticles, folic acid solution, and rhodamine solution have been depicted.

The band around 575 nm for the fluorescent emission spectra of the systems containing rhodamine (FA-IONPs-RITC and IONPs-RITC) and the one for the solution of RITC are in excellent agreement with the previously reported around 570–575 nm [33, 34]. The differences in the band are due to the chemical environment, and the low intensity is due to the quantity employed in the synthesis procedure (being less than 0.1% of the total system).

For the systems with FA, either FA-IONPs-RITC or IONPs-AF, the emission spectra presented a common band at 545 nm. In the case of FA-IONPs-RITC, a second band appeared at 579 nm that corresponds to the RITC molecule previously described. For the band at 545 nm, according to previous studies, FA could be present in two forms (basic and acid), due to the pteridine ring moiety. In the emission spectra, the alkaline form used to have a band between 300 and 400 nm and another band in the 230–290 nm range with higher absorption coefficients than their acid form. On the

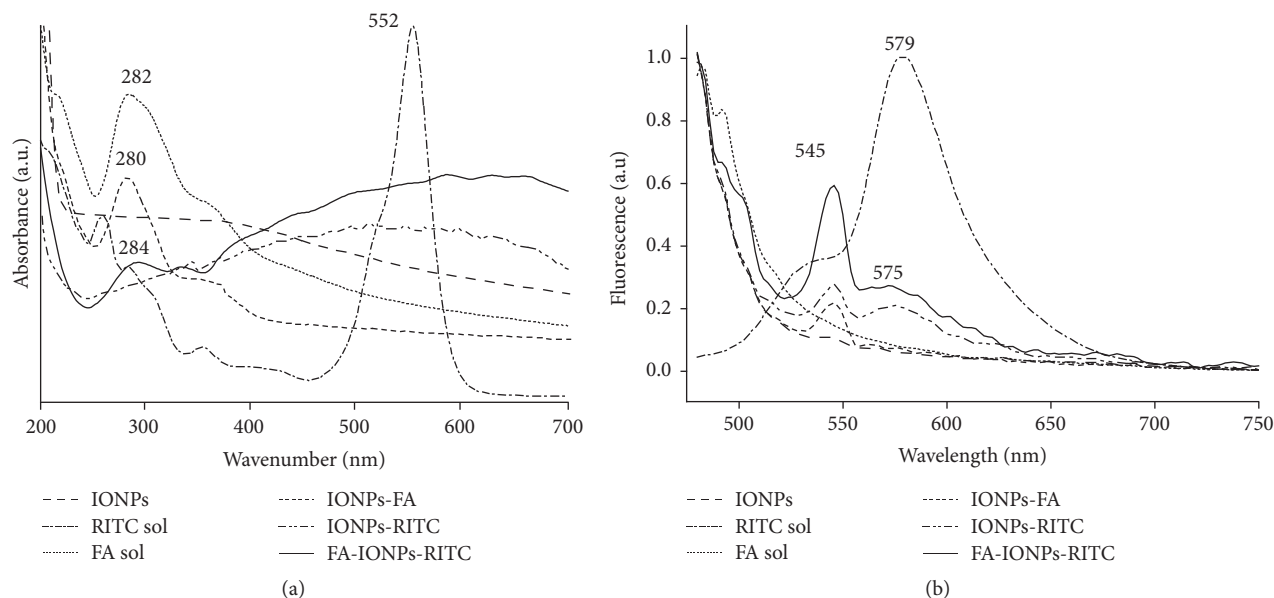


FIGURE 5: (a) UV-Vis spectra of unmodified magnetite, folic acid conjugate, rhodamine conjugate, folic acid/rhodamine magnetite nanoparticles, folic acid solution, and rhodamine solution. (b) Fluorescence emission spectra of magnetite, folic acid conjugate, rhodamine conjugate, folic acid/rhodamine magnetite nanoparticles, folic acid solution, and rhodamine solution.

TABLE 1: Determination of concentration of FA and RITC conjugated over the IONPs' surface.

Initial [FA] [mg mL ⁻¹]	% FA in IONPs' surface [%]	FA in IONPs' surface [mg mL ⁻¹]	Initial [RITC] [mg mL ⁻¹]	% RITC in IONPs' surface [%]	RITC in IONPs' surface [mg mL ⁻¹]
4.4	98.8	4.3	0.75	96.8	0.72
3.8	98.3	3.7	2.25	96.9	2.18
3.2	98.2	3.1	3.75	97.0	3.63
2.6	98.0	2.5			
2.2	97.7	2.1			
1.0	96.0	0.9			

other hand, the complete molecule of FA usually presents two bands (at 255 nm and 285 nm) in its alkaline form and an overlapping of the same for the acid form, resulting in a unique band at 285 nm.

Considering this and assuming that the system conjugation was carried out according to what is previously proposed, it is possible to suggest that the pteridine moiety is exposed on system surface. Thus, with the fluorescence studies, it was possible to observe a relative increment of the band at 545 nm, which corresponds to the alkaline form, indicating, in that way, the correct and suitable system conjugation. However, the magnetite core presented a lower intensity band in the same region (~545 nm), so it is possible to suggest that, in the FA-IONPs-RITC and IONPs-RITC systems, a contribution of both compounds (IONPs and FA) existed in order to increase the intensity of the band in that wavelength. As for the IONPs-RITC system, there was no FA (with its pteridine ring moiety), which can cause the appearance of a band.

3.5. FA Conjugated over the IONPs' Surface. In accordance with the percentages obtained from analysis, it was possible to observe that, even at the lowest initial concentration of

FA, $a > 95\%$ of FA in IONPs surface was reached. Also was important the fact that the reaction had a maximal saturation point with a concentration > 5.0 mM, where the percentages were over 98%. These data results were important to optimize the quantities of FA in the final system. In Table 1, the concentrations of FA employed and the percentage of conjugation over the nanoparticle surface are shown.

3.6. RITC Conjugated over the IONPs' Surface. The results demonstrate that, even at the lowest initial concentration of RITC, $a > 95\%$ was conjugated in IONPs surface. The saturation of the system for this specific case was reached even with the lowest initial concentration employed, where the percentages were over 96%. These data results were important to optimize the quantities of RITC in the final system. In Table 1, the RITC concentrations and the conjugation percentage are shown.

Magnetite nanoparticles were successfully prepared in accordance with previous reports using a chemical coprecipitation method in a basic medium, obtaining spheroidal forms with nanometric size [26]. The amino-modified nanoparticles were used as precursor, the functionalization was carried

out using a derivative of phosphonic acid that undergoes easy formation of a self-assembled, strongly organic monolayer on the nanoparticle surface, and established mechanisms are the chemisorption of 2-AEP on IONPs for the introduction of polar functional groups onto the surface [27]. This coating allows further functionalization by chemical reactions [2]. Several studies have reported that phosphonates and phosphates bind efficiently to the iron oxide nanoparticle surface and can be useful as potential alternatives to link fatty acids or other functional groups. Also, they have good biocompatibility and a high capacity to form strong complexes with transition metals in aqueous solution and show suitable affinity for the metal oxide surface [2, 35]; additionally, a significant increase on colloidal and chemical stability was observed preventing nanoparticle oxidation processes.

Considering that colloidal stability in an aqueous and physiological medium is one of the most important issues related to the biomedical applications of nanoparticles, these polar functional groups render nanoparticles thermodynamically stable against aggregation and keep them well-dispersed in aqueous media. Furthermore, this system facilitates conjugation with a variety of molecules through sulfhydryl, carboxyl, anhydride, or imine groups, allowing easy manipulation of the surface functionality [35].

The molecular imaging techniques provide a reliable methodology to monitor and record the presence, location, and extent of diseases, although methods such as computed tomography and magnetic resonance imaging have been primary tools for cancer diagnostic, the introduction of new criteria and recommendations for the assessment of an adequate diagnostic, and measure of progression disease, promoting the development of bimodal targeted contrast agents for the detection of molecular markers with both MRI and fluorescence imaging.

In our case, the formation of magnetofluorescent nanoparticles was achieved through a covalent immobilization of rhodamine B isothiocyanate (RITC) on the particle surface, by means of a thiourea linkage through a nucleophilic addition of surface-pendent amine to isothiocyanate groups, to which primary amino groups of suitable organic molecules can be covalently linked, forming the magnetic fluorescent carrier, in this particular case [22, 36].

To achieve specificity and cell receptor selectivity, the magnetite nanoparticles were functionalized with folic acid. The active-NH₂ groups present on the amino-functionalized nanoparticle surface were covalently conjugated with FA *via* activation of the carboxyl groups in its glutamic acid moiety by the carbodiimide method. This method may lead to the formation of two structural isomers, in which FA is linked either through the α -carboxyl or through γ -carboxyl group of its glutamic acid moiety. However, the folate linked *via* γ -carboxyl group is formed as the major isomer because it is more prone to this reaction due to its higher reactivity and retains a strong affinity towards its receptor, whereas its α -carboxyl derivatives are not recognized as readily [36].

The information obtained with analytical technique suggests that the conjugation of the FA at the surface of the IONPs was carried out successfully, as well as the preparation of the multifunctional system FA-IONPs-RITC.

3.7. Nanoparticle-Induced Cytotoxicity. For the cell viability test, the IONPs exposure time was 24 h as usual. It is important to note that the highest IONPs concentration employed (0.5 mg mL^{-1}) was lower than concentrations used in other studies with different cell lines but much higher than in many other works with that employed magnetite [37]. According to the results shown in Figure 6(a), there was a significant difference between the lowest (0.0 mg mL^{-1}) and the highest (0.5 mg mL^{-1}) concentrations. Despite this, all treatments showed cell viability higher than 80%. The highest FA-IONPs-RITC concentration (0.5 mg mL^{-1}) showed 82.5% of viability, which demonstrated the biocompatibility of the multifunctional system.

3.8. Cellular Uptake. The folate-conjugated nanoparticles were found to be distributed within the cytoplasm, suggesting cellular internalization through receptor-mediated endocytosis, instead of adhesion to the cell surface. This study unequivocally establishes that all the iron oxide folate nanoconjugates, developed in the course of this research, are preferentially targeted towards cancer cells and effectively internalized ($63 \pm 7\%$ of internalization with respect to $43 \pm 5\%$ of the blocked group). Also, the results indicated that the system with FA could enhance the intracellular uptake of the IONPs effectively, assuming that FA works as a tumor-targeting ligand, which likely enhances receptor-mediated endocytosis [31]. Receptor-mediated internalization of nanoparticles by FA receptor in overexpressing cancer cells was further demonstrated using an inverted confocal microscope (Olympus IX80). As was predicted from the cytotoxicity experiments, photomicrographs (taken with an Olympus IX80 inverted confocal microscope and an AxioVision software) clearly showed that cellular structures were well preserved without morphology abnormalities after nanoparticles treatment (see Figure 6(b)).

According to previous reports, a nanoparticle size between 10 and 100 nm results in systems with a size small enough to avoid the mononuclear phagocyte system (MPS) and to penetrate the capillary body cavities. Also, for medical applications, nanoparticles must conform to a size smaller than 100 nm, at which they possess unique physicochemical and pharmacokinetic characteristics are desirables [12, 38].

Generally, once a tumor-targeting ligand conjugate has reached its target receptor, uptake and internalization can occur through receptor-mediated bioevents, mainly receptor-mediated endocytosis, but phagocytosis and pinocytosis can also contribute to internalization. After endocytosis, most but not all ligand-receptor complexes dissociate in the endosomes and the ligand eventually ends up in the lysosomes, while receptors are often recycled and transported back to the cell surface by transport vesicles [31].

The results of the internalization of magnetic nanoparticles are dependent on two factors: (I) the type of coating and (II) the nanoparticle concentration [31]. In the system designed, FA demonstrated that it can promote tumor cell receptor-mediated internalization [17].

A promising diagnostic imaging methods consist in molecular targeting with exogenous fluorescent agents,

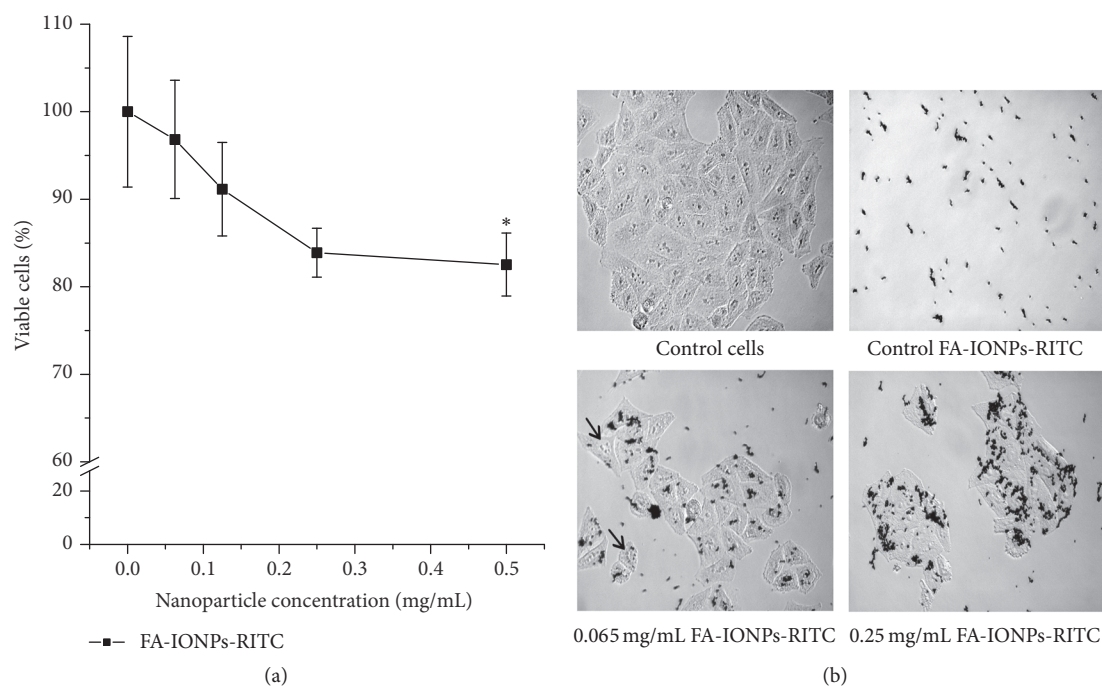


FIGURE 6: (a) Effect of folate-rhodamine-conjugated nanoparticles on the HeLa cells viability. Cells incubated with different nanoparticle concentrations for 24 h at 37°C followed by crystal violet staining. * No significant reduction ($p < 0.05$) in cellular viability was observed, the survival rate being higher than 80%, even at the highest nanoparticle concentration. (b) Photomicrographs of cellular uptake test in HeLa cells at two different concentrations. The black arrows show the internalization of the system, which is visible even at low concentrations (0.065 mg mL^{-1}).

employing sensitive targets to report disease and metabolism activity; FA-IONPs-RITC system provides a new class of magnetic/fluorescent nanomaterial. Additionally, fluorescent properties of this conjugate, water soluble, chemically stable, and biocompatible, are desirable features for pharmaceutical purposes. New molecular imaging devices offer the advantage for better spatial resolution and could be applied to extend three-dimensional tissue architecture and dynamic metabolic processes. The development of hybrid contrast agents is based on increasing capabilities to overcome depth tissue limitations and spatial accuracy by image fusion techniques.

4. Conclusions

In this work, iron oxide magnetite nanoparticles, modified with folic acid/rhodamine, were successfully synthesized *via* carbodiimide reaction. This system demonstrated optimal conditions for their use in medical application. The proposed uptake mechanism is through folic acid receptor endocytosis. However, to assure that such mechanism is involved, it is necessary to carry out studies focused on the labeling and tracing of the mechanism through recognition of its receptor. Also, PK studies are crucial in order to elucidate their behavior *in vivo* and also to prove their magnetic and fluorescent properties.

Conflicts of Interest

The authors confirm that this article content has no conflicts of interest.

Acknowledgments

This study was supported by the International Atomic Energy Agency (CRP-F22064, Contract no. 18358) and the Universidad Autónoma del Estado de México, through Project no. 3543/2013CHT. The authors gratefully acknowledge the skillful analytical and instrumental assistance of “Laboratorio Nacional de Investigación y Desarrollo de Radiofármacos, CONACyT.”

References

- [1] K. Chen and X. Chen, “Design and development of molecular imaging probes,” *Current Topics in Medicinal Chemistry*, vol. 10, no. 12, pp. 1227–1236, 2010.
- [2] M. Mahmoudi, M. A. Sahraian, M. A. Shokrgozar, and S. Laurent, “Superparamagnetic iron oxide nanoparticles: promises for diagnosis and treatment of multiple sclerosis,” *ACS Chemical Neuroscience*, vol. 2, no. 3, pp. 118–140, 2011.
- [3] M. K. Yu, J. Park, and S. Jon, “Targeting strategies for multifunctional nanoparticles in cancer imaging and therapy,” *Theranostics*, vol. 2, no. 1, pp. 3–44, 2012.
- [4] F. Zeinali Sehgri, S. Majidi, S. Asvadi et al., “An update on clinical applications of magnetic nanoparticles for increasing the resolution of magnetic resonance imaging,” *Artificial Cells, Nanomedicine, and Biotechnology*, pp. 1–6, 2015.
- [5] C. Rümennapp, B. Gleich, H. G. Mannherz, and A. Haase, “Detection of molecules and cells using nuclear magnetic resonance with magnetic nanoparticles,” *Journal of Magnetism and Magnetic Materials*, vol. 380, pp. 271–275, 2015.

- [6] K. Y. Choi, G. Liu, S. Lee, and X. Chen, "Theranostic nanoplat-forms for simultaneous cancer imaging and therapy: current approaches and future perspectives," *Nanoscale*, vol. 4, no. 2, pp. 330–342, 2012.
- [7] K. M. Bennett, J.-I. Jo, H. Cabral, R. Bakalova, and I. Aoki, "MR imaging techniques for nano-pathophysiology and theranostics," *Advanced Drug Delivery Reviews*, vol. 74, pp. 75–94, 2014.
- [8] J. E. Rosen, L. Chan, D.-B. Shieh, and F. X. Gu, "Iron oxide nanoparticles for targeted cancer imaging and diagnostics," *Nanomedicine: Nanotechnology, Biology, and Medicine*, vol. 8, no. 3, pp. 275–290, 2012.
- [9] K. C. Barick, S. Singh, D. Bahadur, M. A. Lawande, D. P. Patkar, and P. A. Hassan, "Carboxyl decorated Fe₃O₄ nanoparticles for MRI diagnosis and localized hyperthermia," *Journal of Colloid and Interface Science*, vol. 418, pp. 120–125, 2014.
- [10] M. K. Lima-Tenório, E. A. Gómez Pineda, N. M. Ahmad, H. Fessi, and A. Elaissari, "Magnetic nanoparticles: in vivo cancer diagnosis and therapy," *International Journal of Pharmaceutics*, vol. 493, no. 1, pp. 313–327, 2015.
- [11] B. Jang, H. Kwon, P. Katila, S. J. Lee, and H. Lee, "Dual delivery of biological therapeutics for multimodal and synergistic cancer therapies," *Advanced Drug Delivery Reviews*, vol. 98, pp. 113–133, 2016.
- [12] L. T. Thu Huong, N. H. Nam, D. H. Doan et al., "Folate attached, curcumin loaded Fe₃O₄ nanoparticles: a novel multifunctional drug delivery system for cancer treatment," *Materials Chemistry and Physics*, vol. 172, pp. 98–104, 2016.
- [13] C. Song, G.-Y. Wang, and D.-M. Kong, "A facile fluorescence method for versatile biomolecular detection based on pristine α -Fe₂O₃ nanoparticle-induced fluorescence quenching," *Biosensors and Bioelectronics*, vol. 68, pp. 239–244, 2015.
- [14] M. Mahmoudi, S. Sant, B. Wang, S. Laurent, and T. Sen, "Superparamagnetic iron oxide nanoparticles (SPIONs): development, surface modification and applications in chemotherapy," *Advanced Drug Delivery Reviews*, vol. 63, no. 1-2, pp. 24–46, 2011.
- [15] N. Erathodiyil and J. Y. Ying, "Functionalization of inorganic nanoparticles for bioimaging applications," *Accounts of Chemical Research*, vol. 44, no. 10, pp. 925–935, 2011.
- [16] J. J. Castillo, T. Rindzevicius, C. E. Rozo, and A. Boisen, "Adsorption and vibrational study of folic acid on gold nanopillar structures using surface-enhanced raman scattering spectroscopy," *Nanomaterials and Nanotechnology*, vol. 5, no. 1, article 29, 2015.
- [17] A. Scomparin, S. Salmaso, A. Eldar-Boock et al., "A comparative study of folate receptor-targeted doxorubicin delivery systems: dosing regimens and therapeutic index," *Journal of Controlled Release*, vol. 208, pp. 106–120, 2015.
- [18] A. Kraiss, L. Wortmann, L. Hermanns et al., "Targeted uptake of folic acid-functionalized iron oxide nanoparticles by ovarian cancer cells in the presence but not in the absence of serum," *Nanomedicine: Nanotechnology, Biology, and Medicine*, vol. 10, no. 7, pp. 1421–1431, 2014.
- [19] L. E. Kelemen, "The role of folate receptor α in cancer development, progression and treatment: cause, consequence or innocent bystander?" *International Journal of Cancer*, vol. 119, no. 2, pp. 243–250, 2006.
- [20] C. Chen, J. Ke, X. Edward Zhou et al., "Structural basis for molecular recognition of folic acid by folate receptors," *Nature*, vol. 500, no. 7463, pp. 486–489, 2013.
- [21] J. Wen, S. Jiang, Z. Chen et al., "Apoptosis selectively induced in BEL-7402 cells by folic acid-modified magnetic nanoparticles combined with 100 Hz magnetic field," *International Journal of Nanomedicine*, vol. 9, no. 1, pp. 2043–2050, 2014.
- [22] M. Magro, G. Sinigaglia, L. Nodari et al., "Charge binding of rhodamine derivative to OH—stabilized nanomaghemite: universal nanocarrier for construction of magnetofluorescent biosensors," *Acta Biomaterialia*, vol. 8, no. 6, pp. 2068–2076, 2012.
- [23] D. Shi, N. M. Bedford, and H.-S. Cho, "Engineered multi-functional nanocarriers for cancer diagnosis and therapeutics," *Small*, vol. 7, no. 18, pp. 2549–2567, 2011.
- [24] P. Eghbali, H. Fattahi, S. Laurent, R. N. Muller, and Y. M. Oskoei, "Fluorophore-tagged superparamagnetic iron oxide nanoparticles as bimodal contrast agents for MR/optical imaging," *Journal of the Iranian Chemical Society*, vol. 13, no. 1, pp. 87–93, 2016.
- [25] V. S. R. Harrison, C. E. Carney, K. W. Macrenaris, and T. J. Meade, "A multimeric MR-optical contrast agent for multimodal imaging," *Chemical Communications*, vol. 50, no. 78, pp. 11469–11471, 2014.
- [26] B. Banerji, S. K. Pramanik, S. Mandal, N. C. Maiti, and K. Chaudhuri, "Synthesis, characterization and cytotoxicity study of magnetic (Fe₃O₄) nanoparticles and their drug conjugate," *RSC Advances*, vol. 2, no. 6, pp. 2493–2497, 2012.
- [27] J. Lodhia, G. Mandarano, N. J. Ferris, P. Eu, and S. F. Cowell, "Development and use of iron oxide nanoparticles (Part 1): synthesis of iron oxide nanoparticles for MRI," *Biomedical Imaging and Intervention Journal*, vol. 6, no. 2, article e12, 2010.
- [28] J. Sun, S. Zhou, P. Hou et al., "Synthesis and characterization of biocompatible Fe₃O₄ nanoparticles," *Journal of Biomedical Materials Research—Part A*, vol. 80, no. 2, pp. 333–341, 2007.
- [29] S. Karamipour, M. S. Sadjadi, and N. Farhadyar, "Fabrication and spectroscopic studies of folic acid-conjugated Fe₃O₄@Au core-shell for targeted drug delivery application," *Spectrochimica Acta—Part A: Molecular and Biomolecular Spectroscopy*, vol. 148, pp. 146–155, 2015.
- [30] S. Sitthichai, C. Pilapong, T. Thongtem, and S. Thongtem, "CMC-coated Fe₃O₄ nanoparticles as new MRI probes for hepatocellular carcinoma," *Applied Surface Science*, vol. 356, pp. 972–977, 2015.
- [31] L. Zhao, T.-H. Kim, H.-W. Kim, J.-C. Ahn, and S. Y. Kim, "Enhanced cellular uptake and phototoxicity of Verteporfin-conjugated gold nanoparticles as theranostic nanocarriers for targeted photodynamic therapy and imaging of cancers," *Materials Science and Engineering C*, vol. 67, pp. 611–622, 2016.
- [32] T. T. T. N'Guyen, H. T. T. Duong, J. Basuki et al., "Functional iron oxide magnetic nanoparticles with hyperthermia-induced drug release ability by using a combination of orthogonal click reactions," *Angewandte Chemie—International Edition*, vol. 52, no. 52, pp. 14152–14156, 2013.
- [33] T. E. Pylaev, E. K. Volkova, V. I. Kochubey, V. A. Bogatyrev, and N. G. Khlebtsov, "DNA detection assay based on fluorescence quenching of rhodamine B by gold nanoparticles: The optical mechanisms," *Journal of Quantitative Spectroscopy and Radiative Transfer*, vol. 131, pp. 34–42, 2013.
- [34] H. Liu, Y. Wang, H. Li, Z. Wang, and D. Xu, "Luminescent Rhodamine B doped core-shell silica nanoparticle labels for protein microarray detection," *Dyes and Pigments*, vol. 98, no. 1, pp. 119–124, 2013.
- [35] M. Das, D. Mishra, T. K. Maiti, A. Basak, and P. Pramanik, "Bio-functionalization of magnetite nanoparticles using an aminophosphonic acid coupling agent: new, ultradispersed, iron-oxide folate nanoconjugates for cancer-specific targeting," *Nanotechnology*, vol. 19, no. 41, Article ID 415101, 2008.

- [36] M. Das, D. Bandyopadhyay, D. Mishra et al., ““Clickable”, trifunctional magnetite nanoparticles and their chemoselective biofunctionalization,” *Bioconjugate Chemistry*, vol. 22, no. 6, pp. 1181–1193, 2011.
- [37] M. Calero, L. Gutiérrez, G. Salas et al., “Efficient and safe internalization of magnetic iron oxide nanoparticles: two fundamental requirements for biomedical applications,” *Nanomedicine: Nanotechnology, Biology, and Medicine*, vol. 10, no. 4, pp. 733–743, 2014.
- [38] A. M. Nyström and K. L. Wooley, “The importance of chemistry in creating well-defined nanoscopic embedded therapeutics: devices capable of the dual functions of imaging and therapy,” *Accounts of Chemical Research*, vol. 44, no. 10, pp. 969–978, 2011.

Research Article

Room Temperature Ferromagnetic and Optical Properties of Chrome Doped ZnS Nanorods Prepared by Hydrothermal Method

Wenhua Zhao,^{1,2} Zhiqiang Wei,^{1,2} Li Zhang,¹ Xiaojuan Wu,^{1,2}
Xuan Wang,² and Jinlong Jiang²

¹State Key Laboratory of Advanced Processing and Recycling Nonferrous Metals, Lanzhou University of Technology, Lanzhou 730050, China

²School of Science, Lanzhou University of Technology, Lanzhou 730050, China

Correspondence should be addressed to Zhiqiang Wei; qianweizuo@163.com

Received 24 December 2016; Accepted 27 February 2017; Published 27 March 2017

Academic Editor: Biswanath Bhoi

Copyright © 2017 Wenhua Zhao et al. This is an open access article distributed under the Creative Commons Attribution License, which permits unrestricted use, distribution, and reproduction in any medium, provided the original work is properly cited.

Cr doped Zn_{1-x}Cr_xS nanorods with different concentration ratio ($x = 0, 0.01, 0.03, \text{ and } 0.05$) were successfully synthesized by hydrothermal method. The crystal microstructure, morphology, chemical composition, and optical and magnetic properties of the samples were characterized by X-ray diffraction (XRD), field-emission scanning electron microscopy (FESEM), high-resolution transmission electron microscopy (HRTEM), X-ray energy dispersive spectrometry (XEDS), diffuse-reflectance spectroscopy (DRS), photoluminescence (PL) spectra, and the vibrating sample magnetometer (VSM). All the samples synthesized by this method exhibited single-phase wurtzite structure with good crystallization as demonstrated by XRD studies, which indicated that all Cr ions successfully substituted for the lattice site of Zn²⁺ and generated single-phase Zn_{1-x}Cr_xS. DRS revealed the band gap of doped Zn_{1-x}Cr_xS underwent blue shift compared to that of the bulk ZnS. PL spectra showed obvious ultraviolet emission peak at 375 nm and two blue emissions appear about 500 and 580 nm. The blue emissions intensity of doped samples improved with the increase of Cr concentration, comparing to pure ZnS. Magnetic measurements indicated that the undoped and doped ZnS nanorods exhibited well-defined ferromagnetic behavior at room temperature. The saturation magnetization weakened significantly with increasing Cr concentration comparing to pure ZnS and reached minimum for 3% Cr.

1. Introduction

Diluted magnetic semiconductors (DMS) are referred to as nonmagnetic semiconductors in which a small fraction of host cations are replaced by transition metal or rare-earth ions, with both spin and charge degrees of freedom in a single material [1]. DMS has attracted enormous interest due to the exchange interactions between the spins of the dopant atoms and the carriers in the semiconductor host, as they are expected to bring global ferromagnetic order in the entire lattice at room temperature. ZnS is a kind of the II-VI semiconductor materials with direct wide band gap energy (3.7 eV), and it is a versatile and multifunctional semiconductor material, which has good piezoelectric, ferromagnetic,

photoelectric, and photosensitive properties [2, 3]. The investigations for ZnS diluted magnetic semiconductor (DMS) nanocrystals have attracted considerable attention due to their novel properties and broad application prospect in diverse areas, such as spin-polarized light emitting diode, spin field-effect transistors, field-emission devices, optical isolator, and quantum computer [4–8].

In recent years, single transition metal doped ZnS have been extensively investigated by various methods, and the electrical, magnetic, and optical properties of ZnS can be modified by controlling the preparation process, changing the kinds of doping elements and doping amount. Transition metals (TMs) (e.g., Nd [9], Mn [10], Co [11], Cu [12], Fe [13], and Ni [14–16]) doped ZnS based diluted magnetic

semiconductors (DMS) are potential candidate for luminescent properties and room temperature ferromagnetism. Many experimental results have observed the room temperature ferromagnetism (RTFM) and extraordinary photoluminescence (PL) primarily depending on the synthesis method as well as processing conditions [17–19]. But, to the best of our knowledge, there are no reports on the effect of the structural, optical, and magnetic properties for Cr doped ZnS nanorods.

Hence, the understanding of FM origination in Cr doped ZnS nanorods is still in urgent demand.

In the present work, undoped and Cr doped ZnS nanorods were synthesized by hydrothermal method using ethylenediamine as modifier. The samples were characterized by X-ray diffraction (XRD), field-emission scanning electron microscopy (FESEM), high-resolution transmission electron microscopy (HRTEM), X-ray energy dispersive spectrometry (XEDS), diffuse-reflectance spectroscopy (DRS), photoluminescence (PL) spectra, and the vibrating sample magnetometer (VSM) to investigate the crystal microstructure, morphology, constituent elements, and optical and magnetic properties.

2. Materials and Methods

$Zn_{1-x}Cr_xS$ nanorods ($x = 0, 0.01, 0.03, \text{ and } 0.05$) were successfully synthesized by hydrothermal method. All raw materials used in this work were of analytical grade and without further purification. In the synthesis process, a required amount of ethylenediamine ($C_2H_8N_2$) was dissolved in deionized water. Meanwhile, weighed zinc acetate ($Zn(CH_3COO)_2 \cdot 2H_2O$) and chrome chloride ($CrCl_3 \cdot 6H_2O$) according to the chemical formula and the mole ratio of the metal cation of undoped ZnS and Cr doped ZnS mixed together and dissolved into the mixed solvent to obtain a solution of 0.015 mol/L. Then a certain amount of thiourea ($(NH_2)_2CS$) was added to the above solution, and the mixture was magnetically stirred at room temperature for 30 min. Finally, the prepared solution was transferred into a 100 ml Teflon lined stainless steel autoclave, and the hydrothermal synthesis was heated at $200^\circ C$ for 12 h in an oven and then cooled to room temperature naturally. Thereafter, the resulting precipitate was separated centrifugally and washed with distilled water and absolute alcohol several times, respectively. The obtained products were dried in oven at $60^\circ C$ for 10 h. Thus, $Zn_{1-x}Cr_xS$ nanocrystals were collected and used for further studies.

The structural analysis of as-synthesized samples was examined by a powder X-ray diffractometer (Japan Rigaku D/Max-2400) with $CuK\alpha$ radiation at $\lambda = 1.54056 \text{ \AA}$. The samples were scanned in the angular range from 10 to 90° (2θ) with scanning rate $0.005^\circ/s$ and step size 0.02° . The average crystalline grain size of the products was estimated from the half maximum width and the peak position of an XRD line broadened according the Scherrer formula. The morphology and microstructure of the samples were observed by field-emission scanning electron microscope (FESEM, 200 FEG) and high-resolution transmission electron microscopy (HRTEM, JEM-2010). The chemical composition of the products was verified by X-ray energy

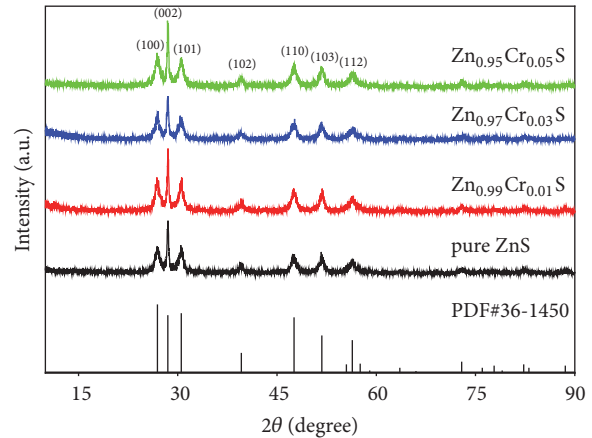


FIGURE 1: XRD patterns of $Zn_{1-x}Cr_xS$ ($x = 0, 0.01, 0.03, \text{ and } 0.05$) nanorods.

dispersive spectroscopy (XEDS) at an acceleration voltage of 200 keV in TEM. The optical properties of the samples were analyzed using ultraviolet-visible (UV-VIS, TU-1901) spectrophotometer. Photoluminescence (PL) spectra were recorded on a PerkinElmer fluorescence spectrometer with the excitation wavelength of 320 nm. Magnetic hysteresis loops were investigated at room temperature using a vibrating sample magnetometer (VSM, Lakeshore 7304) with an applied field from -8000 Oe to 8000 Oe.

3. Results and Discussion

3.1. Structural Analysis. The XRD patterns of different doping concentration ratio $Zn_{1-x}Cr_xS$ ($x = 0.01, 0.03, \text{ and } 0.05$) nanorods compared with pure ZnS are shown in Figure 1. It is obvious that the diffraction peaks located at $2\theta = 26.91^\circ, 28.50^\circ, 30.53^\circ, 39.61^\circ, 47.56^\circ, 51.78^\circ, \text{ and } 56.39^\circ$ correspond to (100), (002), (101), (102), (110), (103), and (112) planes, respectively. All the diffraction peaks can be well indexed with the single-phase hexagonal wurtzite ZnS structure, which are readily matched with the standard spectrum (JCPDS 36-1450). In addition, no extra diffraction peaks assigned to other secondary phases such as metal clusters or metal oxides are detected from the XRD patterns, which confirms that the samples are pure single phase. Thus, it indicates that Cr^{3+} is effectively substituted into Zn^{2+} ions sites within the ZnS crystal lattice without changing the wurtzite structure of the parent ZnS.

Based on the XRD results, the average crystalline size of pure ZnS and doped ZnS nanorods can be calculated from the full width at half maximum (FWHM) of the most intense diffraction peak (002) according to Scherrer formula as follows: $D = K\lambda/B \cos \theta$, where D represents the average crystalline size, $K = 0.89$ is the Scherrer constant, λ is X-ray wavelength (Cu Ka, 1.54056 \AA), θ is the diffraction angle, and B is FWHM of (002) diffraction peak in radians. The (002) diffraction peak FWHM of pure ZnS is greater than that of doped ZnS samples, which is indicating the incorporation of dopant ions as substituents in the lattice of the host material. It is evident that the increase slightly

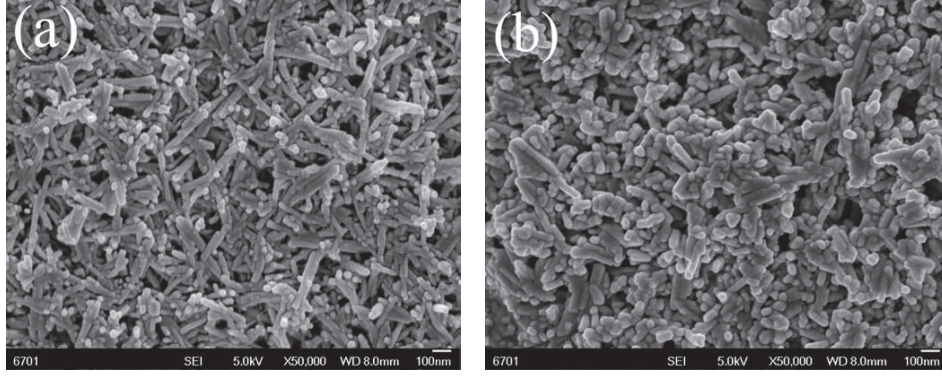


FIGURE 2: FESEM images of (a) pure ZnS and (b) $\text{Zn}_{0.95}\text{Cr}_{0.05}\text{S}$ nanorods.

TABLE 1: Parameters of the XRD patterns for $\text{Zn}_{1-x}\text{Cr}_x\text{S}$ ($x = 0, 0.01, 0.03, \text{ and } 0.05$) nanorods.

Sample	2θ ($^\circ$)	FWHM ($^\circ$)	d_{hkl} (\AA)	a (\AA)	c (\AA)	Cell volume (\AA^3)	D (nm)
Pure ZnS	28.500	0.269	3.129	3.829	6.258	79.45	30
$\text{Zn}_{0.99}\text{Cr}_{0.01}\text{S}$	28.520	0.213	3.127	3.828	6.254	79.36	34
$\text{Zn}_{0.97}\text{Cr}_{0.03}\text{S}$	28.618	0.245	3.117	3.799	6.233	77.90	36
$\text{Zn}_{0.95}\text{Cr}_{0.05}\text{S}$	28.539	0.258	3.125	3.824	6.250	79.15	39

of FWHM with increasing Cr dopant concentration is in turn increase of the crystallite size. Comparing the doped samples and pure ZnS, the results suggest that the doping concentration influences the crystallites size.

The corresponding parameters of the main diffraction peak (002) for undoped ZnS and Cr doped ZnS samples are listed in Table 1. The (002) diffraction peak position for $\text{Zn}_{1-x}\text{Cr}_x\text{S}$ samples evidently shifts to higher angle, comparing to pure ZnS. In addition, the peak positions of synthesized $\text{Zn}_{1-x}\text{Cr}_x\text{S}$ nanorods shift to higher angles with the concentration of Cr doping increasing. When there is a small amount of Cr doping ($x = 0.03$), the diffraction peak position of the doped ZnS nanorods reaches maximum. Shift of peak position towards higher angle is explained from lattice constant shrinkage, which is attributed to the substitution of the Zn^{2+} ions by the smaller Cr^{3+} ions. According to the Bragg formula: $2d_{hkl} \sin \theta = \lambda$, where d_{hkl} denotes the crystalline plane distance for indices (hkl) and θ is the diffraction angle of the (002) peak. Plainly, the decrease of the crystalline plane distances will result in the increase of the diffraction angles. From Table 1, it can be found that d values of pure ZnS are greater than that of doped ZnS samples, while d value of doped samples decrease with the increase of Cr doped content. The lattice constants a and c are calculated by the following formula:

$a = d_{hkl} \sqrt{(4/3)(h^2 + hk + l^2) + (a/c)^2 l^2}$, the lattice constant a is obtained for the (100) plane through the relation $a = \lambda / \sqrt{3} \sin \theta$, and the lattice constant c is derived for the (002) plane using the relation $c = \lambda / \sin \theta$, respectively. The calculation results are given in Table 1. The lattice constants of the doped ZnS are smaller than that of pure ZnS, and the lattice constants a and c and their interplanar distance of

doped ZnS decrease with the increase of Cr doped content, reaching minimum for 3% Cr. It can be attributed that the ionic radius of the Cr^{3+} (0.69 \AA) is smaller than that of the Zn^{2+} (0.74 \AA), which revealed that Cr ions occupy Zn ions sites in the wurtzite structure, causing lattice distortion [20].

The volume of unit cell of hexagonal system is evaluated from equation: $V = \sqrt{3}a^2c/2 = 0.866a^2c$. As the doping concentration is increasing, the volume of the unit cell of the doped nanorods dramatically decreases comparing to pure ZnS. When there is a small amount of Cr doping ($x = 0.03$), the volume of the unit cell of the doped nanorods reaches maximum, which is shown in Table 1. It indicates that the changes in peak position, peak width, and peak intensity depend on the lattice parameter and cell volume, which is mainly attributed to the successful incorporation of Cr^{3+} ions into ZnS lattice.

3.2. Morphological Studies. The morphology of pure ZnS and doped ZnS samples is studied by FESEM and HRTEM. Figure 2 shows the FESEM images of the undoped ZnS and $\text{Zn}_{0.95}\text{Cr}_{0.05}\text{S}$ samples, respectively. Figure 2(a) shows FESEM images of undoped ZnS sample, and it is observed that pure ZnS nanorods possess one-dimensional rod-like shape. The diameter of the samples ranges from 30 to 40 nm, with an average diameter approximately 30 nm and the length about 200–300 nm. The micrograph clearly indicates the presence of weak aggregation between the rods. Figure 2(b) shows the FESEM micrograph of $\text{Zn}_{0.95}\text{Cr}_{0.05}\text{S}$ sample, which shows the presence of large roughly one-dimensional rod-like structure with regular length distribution. Cr doped ZnS system does not change the morphology of the samples, but the diameter slightly increases and the length decreases with the increase

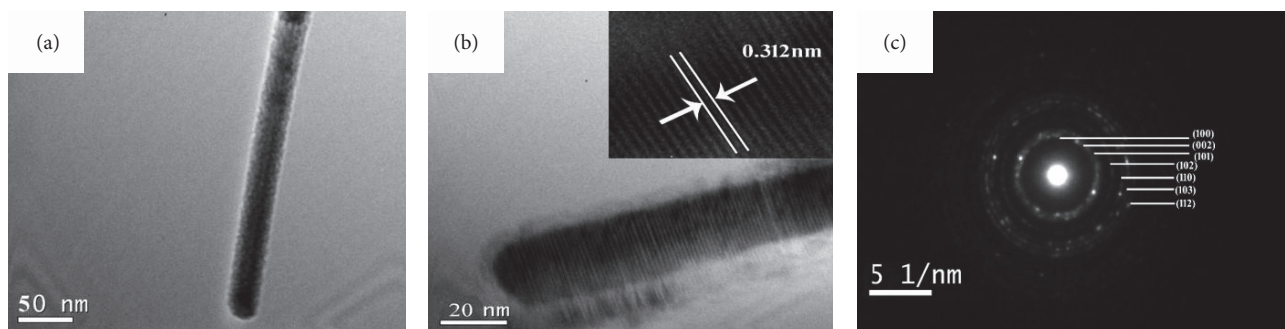


FIGURE 3: HRTEM micrographs and SAED patterns of $\text{Zn}_{0.95}\text{Cr}_{0.05}\text{S}$.

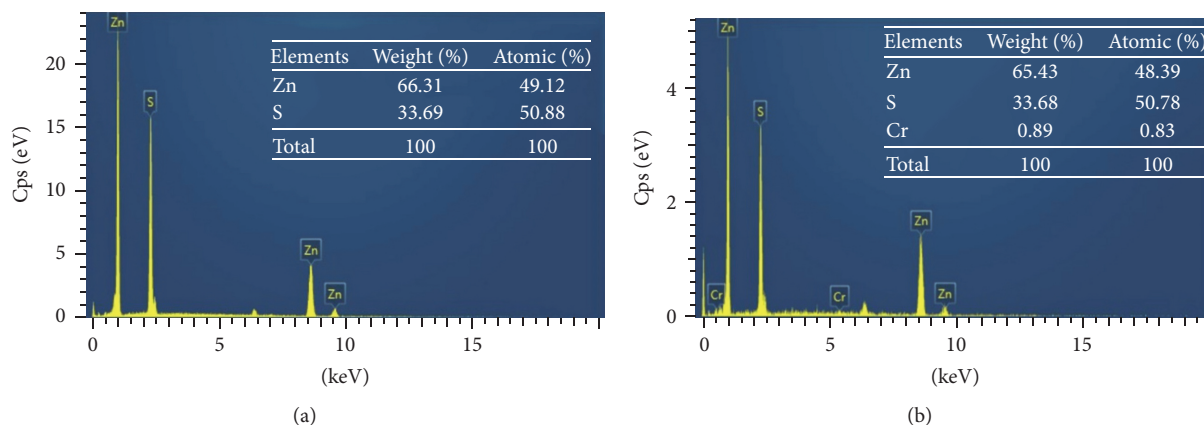


FIGURE 4: XEDS patterns of pure ZnS (a) and $\text{Zn}_{0.95}\text{Cr}_{0.05}\text{S}$ (b).

of Cr concentration. From the above observations, it can be noticed that the doping concentration of Cr affects the parent ZnS, and the nanorods are in the nanoscale region. Comparing with pure ZnS samples, the morphology of doped samples becomes shorter and wider, and the rod length diameter ratio becomes lower.

Figure 3 displays the HRTEM micrographs of $\text{Zn}_{0.95}\text{Cr}_{0.05}\text{S}$ sample. From this figure, it can be found that $\text{Zn}_{0.95}\text{Cr}_{0.05}\text{S}$ nanorods are the same as the FESEM images, possessing roughly one-dimensional rod-like structure and well dispersed with clear edge and smooth surface. The average diameter of the nanorods is about 30 nm, and the length ranges from 200 to 300 nm. Figure 3(b) displays the typical HRTEM image of $\text{Zn}_{0.95}\text{Cr}_{0.05}\text{S}$ nanorods, and it reveals the clear lattice fringe, with no obvious defects. The interplanar distance is about 0.312 nm, which is in good agreement with the d -spacing of (002) plane of hexagonal wurtzite ZnS structure. The value of lattice spacing is smaller than that of bulk ZnS, and the crystal lattice has tendency to shrink, which can be attributed to the difference of ion radius of Zn^{2+} (0.74 Å) comparing with that of Cr^{3+} (0.69 Å). Therefore, it is evident that Cr doping influences the morphology of the samples. The HRTEM analysis is in good agreement with the FESEM and XRD results, which further indicates that all Cr^{3+} successfully substituted for the lattice site of Zn^{2+} and generated single-phase $\text{Zn}_{1-x}\text{Cr}_x\text{S}$ [21].

The corresponding selected area electron diffraction (SAED) patterns of $\text{Zn}_{0.95}\text{Cr}_{0.05}\text{S}$ sample are shown in Figure 3(c), and the SAED pattern consists of many regular diffraction rings with different radius and one center. These rings correspond to (100), (002), (101), (102), (110), (103), and (112) planes of $\text{Zn}_{0.95}\text{Cr}_{0.05}\text{S}$ nanorods from inner to exterior, respectively. The SAED pattern also confirms that $\text{Zn}_{0.95}\text{Cr}_{0.05}\text{S}$ nanorods are wurtzite structure, belonging to polycrystalline structure, which is in agreement with the result of XRD. It indicates that the Cr^{3+} ions do not degrade the crystallinity of ZnS nanorods.

3.3. Chemical Characterization. In order to confirm the existence of the Cr elements of the doped samples, XEDS analysis is recorded. Figure 4 shows the XEDS patterns of the undoped ZnS and $\text{Zn}_{0.92}\text{Cr}_{0.05}\text{S}$ nanorods. From Figure 4(a), it can be found that the undoped ZnS nanorods mainly contain S and Zn two elements. Figure 4(b) obviously confirms the presence of Cr elements besides S and Zn elements for $\text{Zn}_{0.95}\text{Cr}_{0.05}\text{S}$ nanorods, whereas the spectrum of pure ZnS did not find the presence of Cr elements. The quantitative atomic and weight percentage of the compositional elements are indicated in the inset of Figure 4. The calculated weight and atomic percentage are nearly equal to their nominal stoichiometry within the experimental error. The XEDS results further verify XRD conclusion, which indicates that

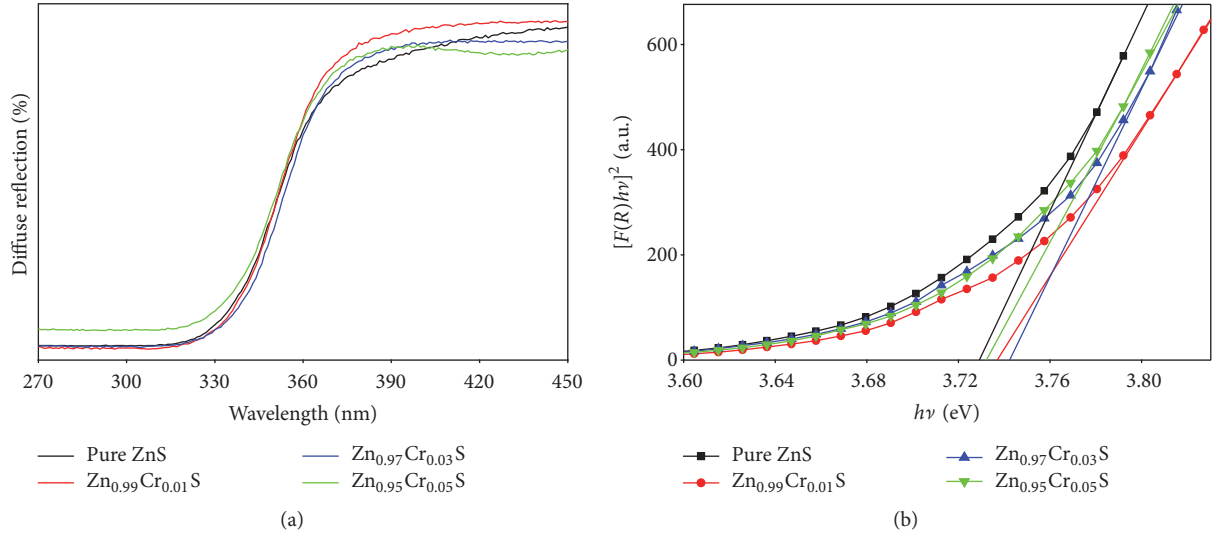


FIGURE 5: UV-Vis diffuse-reflectance spectra (a) and $(F(R)hv)^2$ versus hv curves (b) of $Zn_{1-x}Cr_xS$ ($x = 0, 0.01, 0.03, \text{ and } 0.05$) nanorods.

TABLE 2: Band gap and magnetic moments of $Zn_{1-x}Cr_xS$ ($x = 0, 0.01, 0.03, \text{ and } 0.05$) nanorods.

Sample	Band gap (eV)	Magnetic moments (emu/g)		
		Saturation magnetization	Remanent magnetization (10^{-4})	Coercivity (Oe)
Pure ZnS	3.729	0.0117	6.415	46.71
$Zn_{0.99}Cr_{0.01}S$	3.737	0.0111	5.122	40.26
$Zn_{0.97}Cr_{0.03}S$	3.743	0.0097	5.339	41.22
$Zn_{0.95}Cr_{0.05}S$	3.732	0.0105	5.376	42.74

Cr doped ZnS diluted magnetic semiconductors are successfully synthesized by hydrothermal method, and Cr^{3+} are successfully substituted as dopant in ZnS matrix.

3.4. Optical Properties. The diffuse-reflectance spectra are employed to investigate the effect of Cr doping on the optical characteristics of $Zn_{1-x}Cr_xS$ nanorods. The DRS of the pure ZnS and doped ZnS nanorods are depicted in Figure 5(a). The characteristic absorption edges band at ultraviolet (UV) region lies in the range of 330–390 nm, which shows that all samples possess wide absorption. The absorption coefficients are different, and there is an effect on the position of the absorption peaks. For analysis purposes the diffuse-reflectance (R) of the sample can be related to the Kubelka-Munk function $F(R)$ by the relation $F(R) = (1 - R)^2/2R$. The band gap of the $Zn_{1-x}Cr_xS$ nanorods is estimated from the diffuse-reflectance spectra by plotting the square of the Kubelka-Munk function $F(R)^2$ versus energy and extrapolating the linear part of the curve to $F(R)^2 = 0$, which is shown in Figure 5(b). The absorption edges for $Zn_{1-x}Cr_xS$ samples are seen to be evidently shifted towards lower wavelengths comparing with pure ZnS and are shown in Figure 5(b). The measured values of optical band gap energy for pure ZnS are showed in Table 2, and $Zn_{0.99}Cr_{0.01}S$, $Zn_{0.97}Cr_{0.03}S$, and $Zn_{0.95}Cr_{0.05}S$ are 3.729 eV, 3.737 eV, 3.743 eV, and 3.732 eV, respectively, which indicates that the Cr ions replace the Zn

ions in the ZnS lattice, and the band gap of Cr doped ZnS samples is greater than that of pure ZnS. The band gap energy gradually increases with the increase of Cr concentration, up to a maximum 3.743 eV for 3% Cr. Furthermore, the band gap values estimated for these samples are in the range of 3.729–3.743 eV that are slightly greater than that of bulk ZnS (3.7 eV), which is manifested in the fact that the band gap energy undergoes blue shift in the doped ZnS system. The increase in the band gap energy with the decrease in the lattice parameters (a , c , and V) is due to the effect of doping, which are strongly supported by XRD results and associated with the variation of the lattice parameters. It can be explained that the increase of optical band gap may be attributed to the sp-d spin-exchange interactions between the band electrons of host matrix and the localized d electrons of the transition metal ion substituting the captions. Thus, the s-d and p-d exchange interactions between the band electrons of ZnS and localized d electrons of Cr give rise to change in the energy band structure, which can increase the band gap.

PL spectra of pure ZnS and Cr doped ZnS nanorods are shown in Figure 6. It is observed that PL intensity of doped samples is higher than pure ZnS sample. The ZnS samples exhibit three obvious broad emission peaks at 375 nm, 500 nm, and 580 nm, respectively. The obvious UV emission can be attributed to originate from excitonic recombination corresponding to the near-band-edge emission (NBE) of

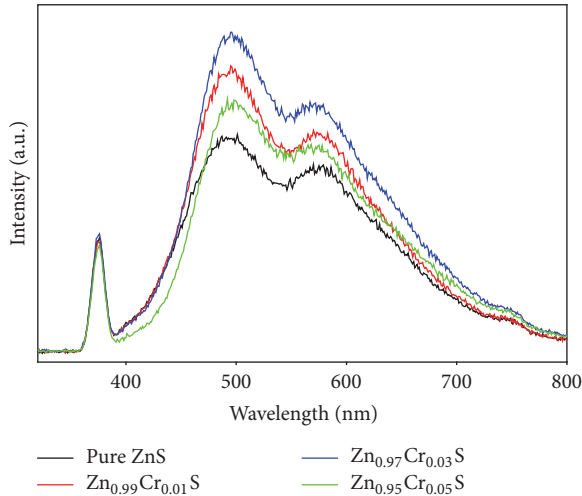


FIGURE 6: PL spectra of $Zn_{1-x}Cr_xS$ ($x = 0, 0.01, 0.03,$ and 0.05) nanorods.

wide band gap of ZnS due to the quantum confinement effect [22]. The blue-green emission bands centered at 500 nm for samples may be attributed to S vacancies in ZnS nanorods and Zn vacancy related defects [23, 24]. The green emission peak at 580 nm is possibly assigned to positively charged electron transition and surface traps mediated by defects in the band gap [25]. The origin of this peak is still not clear and needs further study.

The doped samples exhibit similar ultraviolet (UV) emission band at 375 nm to compare with pure ZnS, which illustrates that the doped samples display nearly the same structure of pure ZnS. As the doping concentration increases, the intensity of PL emission of the doped nanorods dramatically increases comparing to pure ZnS. When there is a small amount of Cr doping ($x = 0.03$), the intensity of the peak of the PL spectrum reaches maximum. It is observed that the particle sizes of the doped samples increase with the increasing of Cr concentration from Table 1, which corresponds with XRD data. The increase in particle size results in enhanced surface defects leading to an increase in the PL intensity as chrome content is increased. It is because Cr^{3+} acts as a sensitizing agent and enhances the radiative recombination processes. Thus, the PL intensity of doped $Zn_{1-x}Cr_xS$ nanorods is higher than that of pure ZnS [26]. These results are in good agreement with XRD, EDX, and UV-visible studies.

3.5. Magnetic Studies. Figure 7 presents the RT magnetic hysteresis ($M-H$) loops of the undoped ZnS and $Zn_{1-x}Cr_xS$ ($x = 0.01, 0.03,$ and 0.05) nanorods measured with the applied magnetic field of 8 kOe. It has deducted the contributions from the diamagnetism of the Si substrate and the paramagnetism of the sample holder during VSM measurement. The $M-H$ curves show that all the samples exhibit obvious ferromagnetic behaviors. The ferromagnetism of undoped ZnS sample is attributed to the fact that sulfur vacancies boost both the emission and the magnetism, which is revealed $d0$ ferromagnetism [27], and the stronger exchange interactions

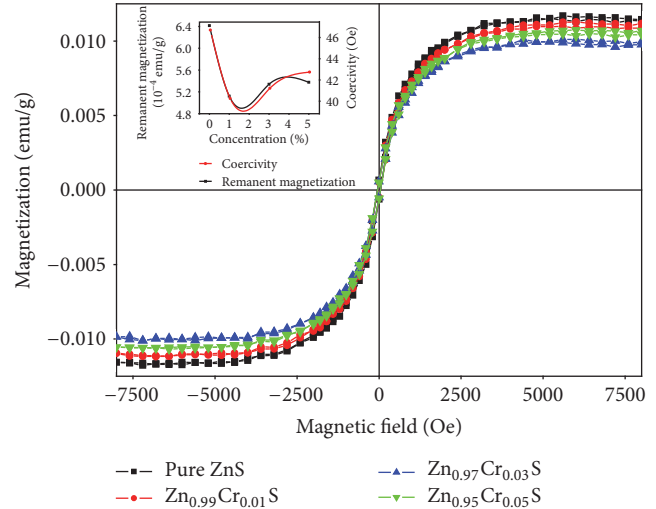


FIGURE 7: $M-H$ curves of $Zn_{1-x}Cr_xS$ ($x = 0, 0.01, 0.03,$ and 0.05) nanorods.

between these sulfur vacancies weakened the saturation magnetization (M_s). From XRD results of doped ZnS nanorods, it is suggested that there are no traces of impurity or secondary phases, thus removing the possibility of ferromagnetism due to the clusters of transition elements or secondary phases in the samples. Hence, the room temperature ferromagnetism of Cr doped ZnS samples could arise from intrinsic magnetic property.

The $M-H$ curves indicate the saturation magnetization values of 0.0117 emu/g, 0.0111 emu/g, 0.0097 emu/g, and 0.0105 emu/g for pure ZnS, $Zn_{0.99}Cr_{0.01}S$, $Zn_{0.97}Cr_{0.03}S$, and $Zn_{0.95}Cr_{0.05}S$ nanorods, respectively. In view of the Cr^{3+} ions substituted into ZnS lattice, the origin of magnetism in the samples is due to the exchange interaction between local spin-polarized electrons (such as the electrons of Cr^{3+} ions) and the conductive electrons. Such interaction can lead to the spin polarization of conductive electrons. Consequently, the spin-polarized conductive electrons undergo an exchange interaction with local spin-polarized electrons of other Cr^{3+} ions. Thus, after a successive long-range exchange interaction, almost all Cr^{3+} ions exhibit the same spin direction, resulting in the ferromagnetism of the material. Poornaprakash et al. also report [28] the magnetic property in Cr doped ZnS nanoparticles by hydrothermal method. Therefore, there is an increase in the intensity of the peak with increase in dopant content in that report.

The saturation magnetization of doped samples is smaller than that of pure ZnS, and the values of saturation magnetization decrease with the increase of Cr doping concentration. It is interesting that the ferromagnetism is suppressed with the Cr concentration increasing. In addition, the saturation magnetization of $Zn_{1-x}Cr_xS$ samples decreases with the increase of Cr concentration comparing to pure ZnS and reaches minimum for 3% Cr. It is because the Cr^{3+} ions substitute the Zn ions, with the local hole concentration at the anion increasing. As the Cr concentration increases, the distance between the Cr atoms and each other is closer and the super

exchange interaction between the neighboring Cr atoms is antiferromagnetic in nature. When there is an increase of Cr doping concentration, the enhanced antiferromagnetic interaction is attributed to the decreased volume and the ferromagnetic ordering is suppressed [29].

The variation of coercivity (H_c) and remanent magnetization (M_r) with Cr concentration of $Zn_{1-x}Cr_xS$ nanorods are indicated in the inset of Figure 7. It is observed that the values of M_s , H_c , and M_r of Cr doped ZnS samples are lower than that of pure ZnS, respectively. In order to investigate the magnetic properties in $Zn_{1-x}Cr_xS$ nanorods clearly, the magnetic moments values are shown in Table 2. Furthermore, the H_c and M_r gradually increase in doped samples with the increase of Cr concentration. When H_c is smaller, the synthesized ZnS nanorods show soft magnetic properties.

4. Conclusions

- (1) Pure ZnS and doped $Zn_{1-x}Cr_xS$ nanorods with different concentration ratio ($x = 0, 0.01, 0.03, \text{ and } 0.05$) were successfully synthesized by hydrothermal method. All the samples synthesized by this method exhibit single-phase wurtzite structure with good crystallization. All Cr ions successfully substituted for the lattice site of Zn^{2+} and generate single-phase $Zn_{1-x}Cr_xS$, the lattice constant underwent distortion, and the grain size increased with increasing Cr doping concentration. The morphology of all the samples is one-dimensional rod-like shape with good dispersion.
- (2) The band gap of doped $Zn_{1-x}Cr_xS$ nanorods underwent blue shift compared to that of the bulk ZnS. PL spectra show obvious ultraviolet emission peak at 375 nm and two blue emissions appear about 500 and 580 nm, and the blue emissions intensity of doped samples improves with the increase of Cr concentration comparing to pure ZnS and reaches maximum for 3% Cr.
- (3) Magnetic measurements indicate that the undoped and Cr doped ZnS samples exhibit ferromagnetic behavior at room temperature, and the saturation magnetization weakened significantly with increasing Cr concentration comparing to pure ZnS and reached minimum for 3% Cr. The variation of coercivity and remanent magnetization of Cr doped ZnS samples is lower than that of pure ZnS, respectively. The H_c and M_r gradually increase with the increase of Cr concentration.

Conflicts of Interest

The authors declare that they have no conflicts of interest.

Acknowledgments

This work was supported by the National Natural Science Foundation of China (no. 51261015) and the Natural Science Foundation of Gansu Province, China (no. 1308RJZA238).

References

- [1] D. Bui and V. Phan, "Ferromagnetic clusters induced by a nonmagnetic random disorder in diluted magnetic semiconductors," *Annals of Physics*, vol. 375, pp. 313–321, 2016.
- [2] J. Cao, Q. Liu, D. Han et al., "Highly enhanced photocatalytic properties of ZnS nanowires-graphene nanocomposites," *RSC Advances*, vol. 4, no. 58, pp. 30798–30806, 2014.
- [3] C.-J. Chang, K.-W. Chu, M.-H. Hsu, and C.-Y. Chen, "Ni-doped ZnS decorated graphene composites with enhanced photocatalytic hydrogen-production performance," *International Journal of Hydrogen Energy*, vol. 40, no. 42, pp. 14498–14506, 2015.
- [4] J.-Y. Kim, H. Kim, S. H. Park et al., "Effect of a critical percolation threshold in purified short carbon nanotube-polymer/ZnS:Cu,Cl composite on electroluminescence," *Organic Electronics: Physics, Materials, Applications*, vol. 13, no. 12, pp. 2959–2966, 2012.
- [5] H. Haddad, A. Chelouche, D. Talantikite, H. Merzouk, F. Boudjouan, and D. Djouadi, "Effects of deposition time in chemically deposited ZnS films in acidic solution," *Thin Solid Films*, vol. 589, pp. 451–456, 2015.
- [6] A. I. Inamdar, S. Cho, Y. Jo et al., "Optical properties in Mn-doped ZnS thin films: photoluminescence quenching," *Materials Letters*, vol. 163, pp. 126–129, 2016.
- [7] M. J. Iqbal and S. Iqbal, "Synthesis of stable and highly luminescent beryllium and magnesium doped ZnS quantum dots suitable for design of photonic and sensor material," *Journal of Luminescence*, vol. 134, pp. 739–746, 2013.
- [8] X. Xu, L. Hu, N. Gao et al., "Controlled growth from ZnS nanoparticles to ZnS-CdS nanoparticle hybrids with enhanced photoactivity," *Advanced Functional Materials*, vol. 25, no. 3, pp. 445–454, 2015.
- [9] B. Poornaprakash, S. Ramu, S.-H. Park, R. P. Vijayalakshmi, and B. K. Reddy, "Room temperature ferromagnetism in Nd doped ZnS diluted magnetic semiconductor nanoparticles," *Materials Letters*, vol. 164, pp. 104–107, 2016.
- [10] R. Nasser, H. Elhouichet, and M. Férid, "Effect of Mn doping on structural, optical and photocatalytic behaviors of hydrothermal $Zn_{1-x}Mn_xS$ nanocrystals," *Applied Surface Science*, vol. 351, pp. 1122–1130, 2015.
- [11] L. Liu, L. Yang, Y. Pu, D. Xiao, and J. Zhu, "Optical properties of water-soluble Co^{2+} :ZnS semiconductor nanocrystals synthesized by a hydrothermal process," *Materials Letters*, vol. 66, no. 1, pp. 121–124, 2012.
- [12] W.-S. Ni and Y.-J. Lin, "Defect-induced magnetic properties of Cu-doped ZnS films with different copper contents," *Journal of Alloys and Compounds*, vol. 649, pp. 968–972, 2015.
- [13] D. Saikia, R. Raland, and J. P. Borah, "Influence of Fe doping on the structural, optical and magnetic properties of ZnS diluted magnetic semiconductor," *Physica E: Low-Dimensional Systems and Nanostructures*, vol. 83, pp. 56–63, 2016.
- [14] G. Murugadoss and M. Rajesh Kumar, "Synthesis and optical properties of monodispersed Ni^{2+} -doped ZnS nanoparticles," *Applied Nanoscience*, vol. 4, no. 1, pp. 67–75, 2014.
- [15] S. Kumar and N. K. Verma, "Effect of Ni-doping on optical and magnetic properties of solvothermally synthesized ZnS wurtzite nanorods," *Journal of Materials Science: Materials in Electronics*, vol. 25, no. 2, pp. 785–790, 2014.
- [16] J. Tang and K. L. Wang, "Electrical spin injection and transport in semiconductor nanowires: challenges, progress and perspectives," *Nanoscale*, vol. 7, no. 10, pp. 4325–4337, 2015.

- [17] C. Liu, D. Meng, H. Pang et al., "Influence of Fe-doping on the structural, optical and magnetic properties of ZnO nanoparticles," *Journal of Magnetism and Magnetic Materials*, vol. 324, no. 20, pp. 3356–3360, 2012.
- [18] A. Goktas and İ. H. Mutlu, "Structural, optical, and magnetic properties of solution-processed co-doped ZnS thin films," *Journal of Electronic Materials*, vol. 45, no. 11, pp. 5709–5720, 2016.
- [19] L.-J. Tang, G.-F. Huang, Y. Tian et al., "Efficient ultraviolet emission of ZnS nanospheres: co doping enhancement," *Materials Letters*, vol. 100, pp. 237–240, 2013.
- [20] X. Wu, Z. Wei, L. Zhang, X. Wang, H. Yang, and J. Jiang, "Optical and magnetic properties of Fe doped ZnO nanoparticles obtained by hydrothermal synthesis," *Journal of Nanomaterials*, vol. 2014, Article ID 792102, 6 pages, 2014.
- [21] X. Wu, Z. Wei, L. Zhang, C. Zhang, H. Yang, and J. Jiang, "Synthesis and characterization of Fe and Ni co-doped ZnO nanorods synthesized by a hydrothermal method," *Ceramics International*, vol. 40, no. 9, pp. 14635–14640, 2014.
- [22] Z. Deng, J. Qi, Y. Zhang, Q. Liao, and Y. Huang, "Growth mechanism and optical properties of ZnS nanotetrapods," *Nanotechnology*, vol. 18, no. 47, Article ID 475603, 2007.
- [23] S. Kar and S. Chaudhuri, "Synthesis and optical properties of single and bicrystalline ZnS nanoribbons," *Chemical Physics Letters*, vol. 414, no. 1–3, pp. 40–46, 2005.
- [24] X. Zhang, Y. Zhang, Y. Song, Z. Wang, and D. Yu, "Optical properties of ZnS nanowires synthesized via simple physical evaporation," *Physica E: Low-Dimensional Systems and Nanostructures*, vol. 28, no. 1, pp. 1–6, 2005.
- [25] Y.-C. Zhu, Y. Bando, and D.-F. Xue, "Spontaneous growth and luminescence of zinc sulfide nanobelts," *Applied Physics Letters*, vol. 82, no. 11, pp. 1769–1771, 2003.
- [26] B. Poornaprakash, D. Amaranatha Reddy, G. Murali, N. Madhusudhana Rao, R. P. Vijayalakshmi, and B. K. Reddy, "Composition dependent room temperature ferromagnetism and PL intensity of cobalt doped ZnS nanoparticles," *Journal of Alloys and Compounds*, vol. 577, pp. 79–85, 2013.
- [27] D. Gao, G. Yang, J. Zhang, Z. Zhu, M. Si, and D. Xue, "D0 ferromagnetism in undoped sphalerite ZnS nanoparticles," *Applied Physics Letters*, vol. 99, no. 5, Article ID 052502, 2011.
- [28] B. Poornaprakash, K. Naveen Kumar, U. Chalapathi, M. Reddeppa, P. T. Poojitha, and S.-H. Park, "Chromium doped ZnS nanoparticles: chemical, structural, luminescence and magnetic studies," *Journal of Materials Science: Materials in Electronics*, vol. 27, no. 6, pp. 6474–6479, 2016.
- [29] S. Sambasivam, D. Paul Joseph, J. G. Lin, and C. Venkateswaran, "Doping induced magnetism in Co-ZnS nanoparticles," *Journal of Solid State Chemistry*, vol. 182, no. 10, pp. 2598–2601, 2009.

Research Article

Biocompatibility and Toxicity of Polylactic Acid/Ferrosferric Oxide Nanomagnetic Microsphere

Hongzhao Xiang,¹ Yuanhua Mu,¹ Chengbo Hu,² and Xiaobing Luo³

¹College of Materials Science and Engineering, Chongqing Jiaotong University, Chongqing 400074, China

²Chongqing Key Laboratory of Environmental Materials & Remediation Technologies, Chongqing University of Arts and Sciences, Chongqing 402160, China

³College of Science, Chongqing University of Posts and Telecommunications, Chongqing 400065, China

Correspondence should be addressed to Hongzhao Xiang; xhzscu@163.com

Received 23 November 2016; Accepted 22 January 2017; Published 19 February 2017

Academic Editor: Vidyadhar Singh

Copyright © 2017 Hongzhao Xiang et al. This is an open access article distributed under the Creative Commons Attribution License, which permits unrestricted use, distribution, and reproduction in any medium, provided the original work is properly cited.

Magnetic targeted drugs delivery system (MTDDS) is a new targeted drug system, which can greatly reduce the dosage and improve the therapeutic efficiency of medicine. Currently superparamagnetic ferric oxide plays important function as targeted drug in the treatment of tumors, but cytotoxicity was still regarded as side effect in the process of drug. In this paper, we take advantage of drug carrier (ferric oxide) toxicity controlling cancer cell growth in cancer treatment, increasing targeted drug efficiency. We applied the modified chemical precipitation method to prepare polylactic acid (PLA) coated high-purity superparamagnetic Fe₃O₄ nanoparticles for targeted drug, characterized PLA/Fe₃O₄ microspheres physical and chemical properties, and then investigated cytotoxicity influence of PLA/Fe₃O₄ nanomagnetic microspheres as carrier for normal liver cells (7701) and liver cancer cells (HePG2) in different concentration; results of MTT and hemolysis and micronucleus test showed that carrier restrained the growth of HePG2 in special concentration; meanwhile the proliferation rate of liver cells was not affected. The study demonstrates that compared with liver cell, liver cancer cells (HepG2) are easy to be disturbed by PLA/Fe₃O₄ nanomagnetic microsphere, which have higher sensitivity and absorption ability. We hope to take advantage of the susceptible property of cancer cells for carriers to improve targeted drug function.

1. Introduction

Currently magnetic nanoparticles play important function as targeted drug in the treatment of tumors, which easily control the site of drug delivering. The drug can aggregate in lesion site for inhibiting and eliminating tumor growth, besides reducing the dosage of no lesion and thus lowering the side effect of drug on normal tissue [1–3]. Among them, superparamagnetic ferric oxide (Fe₃O₄, γ -Fe₂O₃, and CO-Fe₂O₄) received special attention, in part due to their magnetic properties, crystal structure, chemical stability, and decreased toxicity (LD50 2000 mg/kg, far higher than the dosage of clinical application). In order to further enhance targeted drug capacity of nanomagnetic particles [4, 5], scientists carry out study from three aspects: (1) selecting appropriate polymer as membrane coating particles, which help to

increase dispersion and biocompatibility of microsphere; (2) modifying the surface, as nanoparticles may bond with kinds of functional group (-OH, -COOH, -NH₂, -CHO, etc.) on the surface of material, which are beneficial for connecting important bioactive substance (such as enzyme, cell, and drug) by adsorption or covalent bonding way; (3) improving particles superparamagnetic properties by adjusting diameter of microsphere, thickness of polymer membrane, and so on, which easily lead to targeted drug separation and tropism under magnetic field.

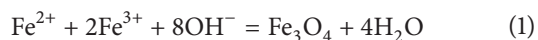
Preparation way of Fe₃O₄ nanomagnetic particles usually includes chemical precipitation, oxidation, and pyrolysis method, in which chemical precipitation method is the frequently used method for preparing Fe₃O₄ nanomagnetic particles. Polyester (polycaprolactone, polylactide) is widely used functional biomaterial with good biocompatibility and

biodegradability, which often acts as membrane coating on the surface of magnetic particles. Magnetic microspheres coated by polyester have the very good application prospect in biological medicine. Utkan et al. [6] adsorbed glycolic acid on the surface of n-Fe₃O₄ by electrostatic effect and catalyzed CL graft reacting with the terminal hydroxyl through Sn(oct)₂, and magnetic component content was about 10–40% in the magnetic polymer microspheres. In the DMSO solution, PCL has the upper critical solution temperature (UCST) at 35°C, and the PCL lattice should be destroyed if above the temperature, meanwhile changing solubility, permeability, and other properties. 35°C is close to the temperature of the human body and therefore has a potential application in controlled drug release. In addition, Ni and Ramanujan [7] used similar way that initiated lactide (LA) reaction. In these experiments, researchers usually pay more attention to toxicity effect of drug delivering, releasing process on the cell or tissue in lesion, and biocompatibility of drug carriers. Today there are more researches on polyethylene glycol (PEG), polylactic acid (PLA), and/or poly-ε-caprolactone (PCL) for coating nanoparticles in the internal and external environment [8–16]. The toxicity reduction in human fibroblast cell was reported with superparamagnetic particles coated with pullulan in human skin fibroblast [17]. But few people take notice that carrier materials have certain potential of toxicity effect for cancer cell growth in targeted drug. In this study, at first we prepared Fe₃O₄ magnetic nanoparticle coated by PLA and then characterized structure, morphology, and biocompatibility of PLA/Fe₃O₄ microsphere; lastly it was investigated whether or not PLA/Fe₃O₄ nanomagnetic microspheres as carrier cause cytotoxicity for growth of normal liver cells and liver cancer cells. This paper focused on toxicity effect of drug carrier to cancer cell proliferation for increasing targeted drug efficiency.

2. Materials and Methods

2.1. Materials. Ferrous chloride tetrahydrate (FeCl₂·4H₂O), ferric chloride hexahydrate (FeCl₃·6H₂O), and hexamine were the products of the Chengdu Changzheng Chemical Reagent Company; oleic acid was obtained from Sichuan Guoguang Chemical Plant; PLA was purchased from Chengdu Lianhe Chemical Reagent Company.

2.2. Synthesis of PLA/Fe₃O₄ Microsphere



n-Fe₃O₄ was synthesized with the chemical precipitation method (see (1)). A certain amount of FeCl₃·6H₂O 1.7 g and FeCl₂·4H₂O 0.6 g (Fe³⁺:Fe²⁺ = 2:1) was dissolved in deionized water and added hexamine. Subsequently the solution was poured into a three-mouth flask, with nitrogen protection, and heated to 80°C, and then ammonia solution was dropped to adjust pH to 10–11, keeping temperature at 80°C for 1 h under vigorous stirring, and gained black n-Fe₃O₄ crystals. Then oleic acid was added, under 80°C for 0.5 h, and cooled to room temperature. Excess ammonia was

neutralized with hydrochloric acid to pH 7, n-Fe₃O₄ isolated by centrifugation and magnet processes, and n-Fe₃O₄ washed with ethanol three times to remove excess oleic acid and hexamine. Finally the crystals were collected and dried in a vacuum oven at 60°C.

PLA/Fe₃O₄ microspheres are prepared as follows: at first 0.5 g PLA was dissolved in 10 mL dichloromethane, then solution was put into three-neck bottle, 0.2 g Fe₃O₄ was added, and solution was stirred and heated at 55°C for one hour and then centrifuged for 5 minutes. The upper layer of the supernatant liquid was decanted and the precipitates were carefully transferred into a beaker. Finally, it was washed several times with distilled water and ultrasonicated and obtained the suspension of n-PLA/Fe₃O₄ microspheres.

2.3. Instruments. X-ray diffraction (XRD) patterns of the samples were characterized in a Philips X'Pert Pro X-ray diffractometer (Philips, Netherlands). All the samples were irradiated with monochromatized CuKα radiation (λ = 0.154178 nm). A continuous scan rate of 5° min⁻¹ from 5° to 80° of 2θ was used for samples. Tube voltage and current were 40 kV and 40 mA, respectively. The functional groups were identified by Fourier transformed infrared (FTIR) spectra recorded using a Nicolet 6700 in transmission mode in the range 4000–400 cm⁻¹ using the KBr pellet method. Transmission electron microscope (TEM) was obtained with a JEOL-2010 (Japan) microscope using an accelerating voltage of 200 kV. PLA/Fe₃O₄ microspheres were observed by scanning electron microscopy (SEM) (S-450; Hitachi Ltd, Tokyo, Japan).

2.4. Cell and Animal Testing. Cells: human liver cells 7701 and human liver cancer cell HepG2 were provided by Sichuan Provincial People's Hospital, the research center of freezing and thawing. There were 60 Kunming mice: 4 weeks old, SPF grade, half male and half female, weight (21 ± 2) g, and provided by medical experimental animal center of Huaxi Medical Central Sichuan University (license number: SYXX 2012-0043). There were 14 New Zealand rabbits, male and female, provided by Sichuan University Animal Center (certificate number: 33-016). MTT [3-(4,5-dimethyl-2-thiazolyl)-2,5-diphenyl-2H-tetrazolium bromide] was purchased from Sigma (St Louis, MO). The cell experiment was completed in the Nanotechnology Central of Sichuan University.

In order to study PLA/Fe₃O₄ nanomagnetic microsphere biocompatibility and cytotoxicity, we applied MTT assays in vitro to investigate proliferation of samples. First, the 7701 cell and HepG2 cell concentration were adjusted to 1 × 10⁵/mL and inoculated on a 96-well culture plate at 100 μL/well. The samples were cultured in the culture box at 37°C under saturated humidity and 5% CO₂ condition. The supernatant was discarded after 24 hours, and then the culture solution was added; besides primary concentration of PLA/Fe₃O₄ nanomagnetic particle solution was diluted up to 2, 5, 10, 15, 20 times. 7701 cell and HepG2 cell were cultured in the magnetic field. The DMEM group was used as the negative control, and a 0.7% polyacrylamide monomer solution was used as the positive control. Each sample group comprising

TABLE 1: Results of MTT test of PLA/Fe₃O₄ magnetic microspheres for 7701 cell.

Group	A490 ($X \pm S$)	Inhibition rate (%)	Relative growth rate (%)	Toxicity grading
Negative control (DMEM)	3.380 ± 0.106		100	0
5% PLA/Fe ₃ O ₄ nanomagnetic fluid	3.321 ± 0.085	1	99	0
25% PLA/Fe ₃ O ₄ nanomagnetic fluid	3.436 ± 0.054	-2	102	0
50% PLA/Fe ₃ O ₄ nanomagnetic fluid	3.164 ± 0.167	2	98	1
75% PLA/Fe ₃ O ₄ nanomagnetic fluid	3.373 ± 0.084	-3	103	0
100% PLA/Fe ₃ O ₄ nanomagnetic fluid	3.035 ± 0.267	4	96	1
Positive control (polyacrylamide)	0.065 ± 0.032	76	24	4

$P < 0.05$ versus positive control group.

TABLE 2: Results of MTT test of PLA/Fe₃O₄ nanomagnetic microspheres for HePG2 cell sequence.

Group	A 490 nm ($X \pm S$)	Inhibition rate (%)	Relative growth rate (%)	Toxicity grading
Negative control (DMEM)	2.405 ± 0.263		100	0
5% PLA/Fe ₃ O ₄ nanomagnetic fluid	1.482 ± 0.307	19	81	1
25% PLA/Fe ₃ O ₄ nanomagnetic fluid	1.454 ± 0.225	15	85	1
50% PLA/Fe ₃ O ₄ nanomagnetic fluid	1.242 ± 0.093	36	64	2
75% PLA/Fe ₃ O ₄ nanomagnetic fluid	1.233 ± 0.158	23	77	1
100% PLA/Fe ₃ O ₄ nanomagnetic fluid	1.172 ± 0.103	40	60	2
Positive control (polyacrylamide)	0.054 ± 0.034	80	20	4

$P < 0.01$, $P < 0.01$ versus negative control group.

nine wells was cultured for 72 hours, and 20 μ L of MTT was then added to each well and vibrated for 10 minutes. The absorbance value was measured at 493 nm using an immunoenzyme labeler.

The relative cell activity rate was calculated as follows: relative growth rate % = OD (optical density) absorbance data of sample/OD absorbance data of negative control \times 100%. The relative growth rate value was converted into six levels, as indicated in Tables 1 and 2. Levels 0-1 are acceptable, whereas level 2 should be assessed comprehensively considering cell morphology, and levels 3-5 are unacceptable.

Hemolysis test: a 10 mL blood sample was taken from a New Zealand rabbit (male, 2.1 kg), and 0.5 mL of 20 g/L potassium oxalate was added to sample. Fresh rabbit blood was diluted (dilution ratio 8 mL blood to 10 mL normal saline). n-Fe₃O₄ microspheres were washed twice with distilled water, dried, and suspended using normal saline (final concentration 0.1 g/mL). Normal saline was used as the negative control and distilled water as the positive control. Each group consisted of three test tubes. There was a suspension of the materials to be tested, and 10 mL normal saline and 10 mL distilled water were added to each tube, which was then placed in a 37°C water bath for 30 minutes. Diluted fresh rabbit blood (0.2 mL) was added to each tube, which was replaced to the 37°C water bath for 60 minutes. Then each tube was centrifuged in a dry centrifuge trunnion for 5 minutes at 2500 rpm; the supernatant was then removed and OD values were measured with a spectrophotometer. Absorbance values of each group were measured at 545 nm in hemolytic test. The hemolysis rate (%) = (OD absorbance data of sample - OD absorbance data of negative control)/(OD absorbance data of positive control - OD absorbance data of negative control) \times 100%. If the hemolytic rate is less than 5%,

the material will have no hemolytic effect and conform to the requirements of the hemolytic test for biomaterials.

Micronucleus assay: 60 Kunming mice were divided into six groups; each group includes ten mice, aged 4 weeks and weighing 20-22 g, (half male and half female). Injecting PLA/Fe₃O₄ suspension into mice abdomen, the dosage groups were 5, 2.5, 1.25, and 0.625 mg/kg. The positive control group used cyclophosphamide (40 mg/kg) for abdominal injection and the negative control group used normal saline for abdominal injection. The 30-hour injection method was applied: a 24-hour interval between two injections, then a 6-hour waits after the second injection, after which time the mice were killed by cervical vertebra dislocation. Narrow smear of the femur was treated by methanol for 5 min and then observed after Giemsa straining. The micronucleus test includes counting micronucleus number in each of the 1000 polychromatic erythrocytes of mouse, calculating the micro-containing rate of cells. The result was expressed (%) and significant difference checked among the groups based on Poisson distribution method.

3. Results and Discussion

3.1. Characterization of PLA/Fe₃O₄ Nanoparticle

3.1.1. XRD Analysis. In Figure 1, the crystal structure of pure Fe₃O₄ and PLA coated Fe₃O₄ microspheres was analyzed by XRD. In this figure, Fe₃O₄ crystal corresponds with face centered cubic (space group: Fd-3m), and lattice parameters of Fe₃O₄ are similar to the data of the International Centre for Diffraction Data [JCPDS: 65-3107]. The peak broadening of the XRD pattern can deduce diameter of particles, and according to the Scherrer formula, we can calculate average

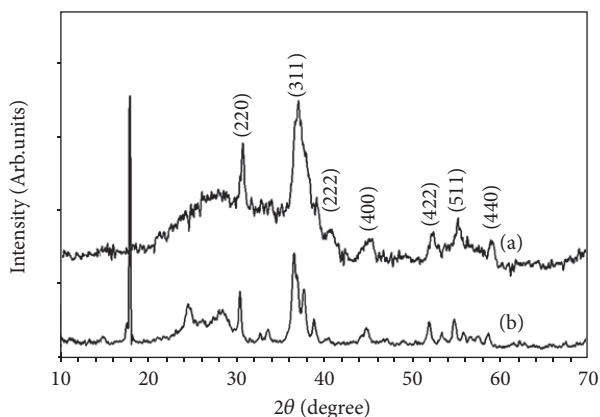


FIGURE 1: XRD pattern for the nanostructure Fe_3O_4 (a) and $\text{PLA}/\text{Fe}_3\text{O}_4$ (b).

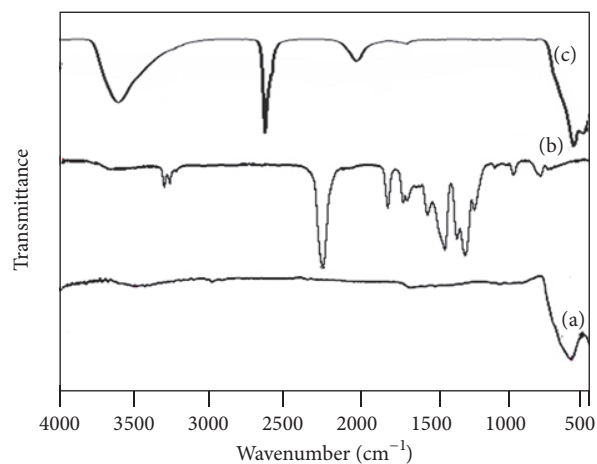


FIGURE 2: FTIR spectra for the Fe_3O_4 (a), PLA (b), and $\text{PLA}/\text{Fe}_3\text{O}_4$ (c).

crystal size, about 40 nm. The intensity of the diffraction peak of (311) plane is stronger than the other peaks. The polymer coated magnetic nanoparticle shows similar XRD peaks, without any peak shift when compared to pure Fe_3O_4 nanoparticle. The characteristic peaks of PLA are about 17.8° , and polymer membrane coated particles' surface, whose factors disturb high degree of crystalline and sharpness of peaks.

3.1.2. FTIR Analysis. Figure 2 corresponds to the FTIR spectrum of pure Fe_3O_4 , PLA, and PLA coated Fe_3O_4 nanomagnetic microspheres, which were measured in the range of $400\text{--}4000\text{ cm}^{-1}$. See Figure 2, and pure Fe_3O_4 crystal shows the broad and strong absorption peak at 574 cm^{-1} , which corresponds with Fe-O bond of Fe_3O_4 crystal [18–20]. A broad peak at 3405 cm^{-1} represents the O-H stretching vibration with the presence of water molecules. No other extra peaks were observed and this confirms the high purity of uncoated magnetic nanoparticle.

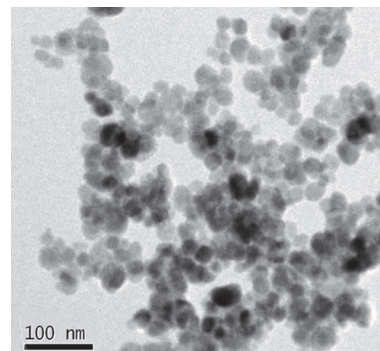


FIGURE 3: TEM images of $n\text{-Fe}_3\text{O}_4$ particles.

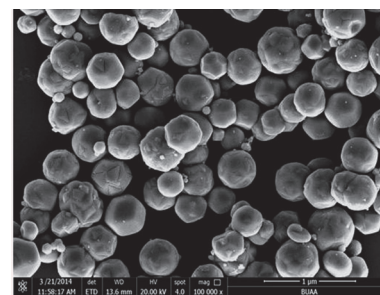


FIGURE 4: SEM image of $\text{PLA}/\text{Fe}_3\text{O}_4$ magnetic microspheres.

PLA coated Fe_3O_4 magnetic microsphere: the peak at 1180 cm^{-1} represents the vibration of the C-O group, and another peak at 1759 cm^{-1} corresponds to the C=O stretching vibration, maybe due to the LA molecule coating the surface of the Fe_3O_4 nanoparticles, so it further confirms the modification of the surface on magnetite nanoparticles by hydrophilic molecules, which facilitate the anisotropic crystal growth. The broad peak at $3400\text{--}3450\text{ cm}^{-1}$ belongs to the O-H stretching vibration of hydroxyl groups. The slight shifts in the Fe-O bond are in the range $480\text{--}590\text{ cm}^{-1}$ for amine and polymer coated magnetic nanoparticles, and it may be due to the hexamine or the polymers coating the nanoparticles, which can enhance stabilization through some physical interaction on the surface of Fe_3O_4 [21]. These results confirm the successful wrapping hexamine and the polymers on the surface of the Fe_3O_4 nanoparticles.

3.1.3. TEM/SEM Observation. Figures 3 and 4 are the TEM images of pure Fe_3O_4 particles and SEM of $\text{PLA}/\text{Fe}_3\text{O}_4$ nanomagnetic particles. Photos reveal that diameter of Fe_3O_4 nanomagnetic particles is about $40\text{--}50\text{ nm}$, and statistics were gathered from more than one hundred particles, which are consistent with calculation result of the Scherrer formula based on the characteristic peak of XRD, mentioned above.

The SEM image of PLA coated Fe_3O_4 magnetic nanoparticles: Figure 4 shows that the monodispersed spherical nanoparticles are around $400\text{--}500\text{ nm}$ in size. Microsphere size controlling is key elements of targeted drug. Reducing particle size can improve the dispersed stability of the microspheres but affects magnetic strength and targeting ability

to transport. Furthermore, increasing size of microspheres can help to form embolism near the tumor vascular and reduce nutrient supplying tumors. In this experiment, size of Fe_3O_4 magnetic microspheres ranges from 400 to 500 nm, and each microsphere consists of many small Fe_3O_4 crystals. The aim of loading drug and gene, polylactic acid (PLA) coating Fe_3O_4 with oleic acid (PEI), can be realized to modify and enhance the loading ability of magnetic microsphere for drug to improve the transportation efficiency [22].

Some researchers applied coprecipitation method to prepare microsphere. Preparation of Fe_3O_4 , precipitation of polymer, and coating nanoparticles are in the same environment. Polymer can be used to reduce aggregation and improve dispersibility of particles by changing the intrinsic properties of magnetic nanoparticles such as size, surface charge, and reactivity. The growth of nanocrystal can be controlled by the interface with organic components or polymer in one-step synthesis. In some experiments, researchers need to modify surface of nanoparticles with several organic and inorganic components before connecting with polymer; they usually divide synthesis into several steps, which are favorable to control reaction condition.

We investigated cytotoxicity influence of PLA/ Fe_3O_4 nanomagnetic microspheres as carrier, hoping to decrease influence of other organic and inorganic components as possible. In one-step method, Fe_2O_3 particles, surfactant, and organic components can be introduced in microsphere together, making it difficult for separation and disturbing result of cytotoxicity test. On the contrary, two-step method can easily control precipitating of n- Fe_3O_4 , crystal growth, modification, washing, and drying process.

Besides hexamine was added in the process of preparing Fe_3O_4 nanoparticles. Adding surfactant is to reduce the surface energy and enhance the formation of monodispersed spherically shaped nanoparticles, which can control the growth of spherical Fe_3O_4 . Hexamine contains one or more functional group such as amide, hydroxyl, and carboxyl groups, which can act as the reaction site to enhance the reaction rate and fine orientation on the surface of Fe_3O_4 . The kinetics of crystal growth leads to the uniform distribution of agglomeration free nanoparticles. When the particles exceed their critical size, the hexamine molecules act not only as shape controlling agents but also as stabilizing agents to control the growth of the magnetic nanoparticles.

3.2. Toxicity and Biocompatibility Study In Vitro and In Vivo

3.2.1. MTT Test. Biocompatibility and toxicity of PLA/ Fe_3O_4 nanomagnetic microspheres were evaluated by MTT (cytotoxicity test), hemolysis test, and micronucleus test.

Tables 1 and 2 show result of MTT of PLA/ Fe_3O_4 microspheres for 7701 cell and HePG2 cell. Table 1 indicates that cytotoxicity of PLA/ Fe_3O_4 microsphere has no effect on growth of normal liver cell at low concentration; Table 2 shows that toxicity grade of PLA/ Fe_3O_4 microsphere ranges from 1 to 2, as mentioned above, and at the level of 2, survival and proliferation of cell not only consider toxicity grade, but also assess cell's morphology comprehensively, which means

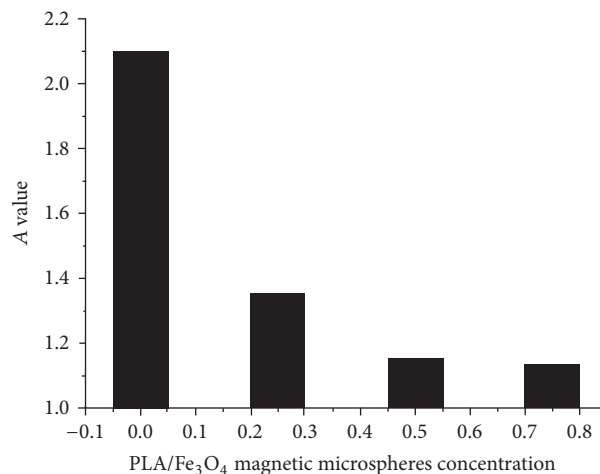


FIGURE 5: Relationship between PLA/ Fe_3O_4 magnetic microspheres concentration and hepatocyte HePG2 activity.

TABLE 3: Results of hemolysis test of PLA/ Fe_3O_4 magnetic nanoparticles extract liquid.

Group	A value			Mean A value
	1	2	3	
Negative control (physiological saline)	0.018	0.017	0.016	0.0173
Experimental	0.020	0.024	0.023	0.0221
Positive control (distilled water)	0.787	0.779	0.770	0.7810

that growth of HepG2 is easy to be disturbed by PLA/ Fe_3O_4 nanomagnetic microsphere at special concentration.

We investigated relationship between the different concentration of PLA/ Fe_3O_4 magnetic nanoparticles and inhibition rate for liver cancer cell HepG2 (see Figure 5). PLA/ Fe_3O_4 nanomagnetic microspheres used as drug carrier have no obvious toxicity to normal liver cells but inhibited liver cancer cells proliferation, which can help targeted drugs to treat cancer and increases the efficacy of the drugs.

3.2.2. Hemolysis Test. The hemolytic test is considered to be a supplementary test for assessment of cytotoxicity. It is used to evaluate if erythrocytes should dissolve and release hemoglobin after direct contact of the biomaterial with blood. It can be a sensitive measure of the biomaterial influence on erythrocytes and plays an important role in evaluation of biological safety. According to Table 3, introduced data of in vitro hemolysis test into the formula of hemolysis [7], result showed that hemolytic data of PLA/ Fe_3O_4 nanomagnetic microsphere was 0.62%, far less than the standard (5%), and showed no hemolysis response, and the requirements of the hemolytic test were met in biomaterials.

3.2.3. Micronucleus Test. The micronucleus test is a strategy to rapidly assess chromosomal damage and interference with mitosis caused by biomaterials. See Table 4; the test found no significant difference for micronucleus formation of the

TABLE 4: Results of micronucleus test of PLA/Fe₃O₄ nanomagnetic fluid ($n = 10$).

Group	Numbers of polychromatocytes	Numbers of micronucleuses in polychromatocytes	Micronucleus rates (%)
Negative control (physiological saline)	10000	26	24
5.00 g/Kg PLA/Fe ₃ O ₄ nanomagnetic fluid	10000	24	23
4.00 g/Kg PLA/Fe ₃ O ₄ nanomagnetic fluid	10000	22	21
2.50 g/Kg PLA/Fe ₃ O ₄ nanomagnetic fluid	10000	20	19
1.25g/Kg PLA/Fe ₃ O ₄ nanomagnetic fluid	10000	21	22
Positive control (cyclophosphamide)	10000	291	289

mice in bone marrow between the material and the negative control group. However, a significant difference for data of the positive control group was noted. Based on these data, the experimental material does not induce deformations or mutations.

3.3. Discussion. Magnetic targeted drugs delivery system (MTDDS) is a new targeted drug system in recent years, which have the immense potential to treat some diseases, especially malignant tumors and other major diseases. MTDDS method can reduce the dosage and side effects and improve the therapeutic efficiency of medicine. Usually magnetic targeted drug delivery system consists of magnetic polymer microspheres and drug, and drug combines with microspheres by physical adsorption, entrapment, and chemical bonding methods. Most of drug loading microspheres play function through arterial injection, and then microspheres were placed and aggregated in lesion position under effect of the magnetic field, take advantage of embolism effect, and release drug, thereby achieving the purpose of treatment. Thus MTDDS can greatly reduce the dosage and side effects in the treatment of disease and improve the therapeutic efficiency. In 1960, Freeman first reported that the crystal (5–100 nm) of iron was introduced into the vascular system and iron accumulated in special part of the body under controlled external magnetic field. Turcu and colleagues [23] prepared magnetic polymethyl methacrylate microspheres containing indomethacin, intravenously injected, and employed magnetic field in the rat tail for 60 min; drug concentration in the rat tail was 60 times higher than that of control group. In recent years, magnetic polymer microspheres as drug carrier for liver cancer therapy attracted scientist's attention [24, 25]. Lbbe and colleagues first applied magnetic polymer microsphere in clinical trials, they used magnetic microspheres (100 nm) containing epirubicin treating 14 patients with advanced stage hepatoma, and results showed that the method of cure reduces the side effect of drugs greatly and, at the same time, realized aggregation of microspheres in targeted area under the magnetic field. However the MRI showed that part of microspheres were detained in the lungs.

There are still some problems for Fe₃O₄ magnetic microsphere as carrier being used in the targeted drug field, especially cytotoxicity. Many studies have demonstrated toxicity of Fe₃O₄ nanoparticles in biological systems. Currently it is not clear whether Fe₃O₄ alone or combination of other

harmful agents (polymer membrane and functional group) causes the danger. Some scientists deduced the phenomenon to the ferric oxide nanoparticle releasing active oxygen and causing oxidative stress and inflammation by the RES (reticuloendothelial system).

So researchers focus on drug release; lowering or eliminating toxicity of targeted drug often follows three elements: (1) the skeleton material in the body can be metabolism and metabolites ought to have no toxicity and be excreted in a certain period; (2) diameter of nonbiodegradable particles (Fe₃O₄) contained in microspheres has to be less than 20 μm [26]; (3) magnetic polymer microspheres should have strong magnetic response potential and high surface area. But they often ignored the value for toxicity of drug carrier. This study investigated influence of carrier toxicity for proliferation of liver cells 7701 and liver cancer cell HepG2 at different concentrations. MTT results showed that carrier restrained the growth of HepG2 in special concentration. Meanwhile, the proliferation rate of liver cells was right. We attributed this result to two factors: (1) liver cancer cells have high sensitivity. Compared with liver cell, HepG2 is easy to be disturbed by PLA/Fe₃O₄ nanomagnetic fluid toxicity, so the growth of HepG2 is inhibited; (2) absorption ability of cancer cell is stronger than normal cells if cocultured with PLA/Fe₃O₄ nanomagnetic solution. So we can take advantage of drug carrier toxicity controlling cancer cell growth in cancer treatment.

In the paper, Fe₃O₄ nanoparticles are modified with oleic acid, its surface bond with oleic acid chains, and hydroxyl group, so it is amphiphathy. If n-Fe₃O₄ were placed in the PLA solution environment, amphiphathy of Fe₃O₄ nanoparticles tends to be self-assembled by bonding with carboxyl group and hydroxyl groups on the surface of Fe₃O₄ nanoparticles; surface charge of PLA/Fe₃O₄ microspheres can affect the dispersion, magnetic strength, and size of microspheres in solvents.

4. Conclusions

In the study, we successfully prepared PLA/Fe₃O₄ nanomagnetic microsphere. Biocompatibility was evaluated by a series test in vivo and in vitro, MTT experiments showed that the toxicity of the material in normal liver cell was between Grade 0 and Grade 1, Fe₃O₄ nanomagnetic microsphere inhibited liver cancer cell proliferation, the material lacked hemolysis

activity, and micronucleus testing showed no genotoxic effects. Test demonstrated that the Fe_3O_4 nanoparticle had no effect on the main organs and blood biochemistry in mice, its performance conforms to clinical requirements, and its biocompatibility conforms to the standard for medical material. We investigated toxicity effect of drug carrier for different cells. As liver cancer cells are susceptible to PLA/ Fe_3O_4 nanomagnetic fluid toxicity, PLA/ Fe_3O_4 carrier has certain potential to restrain liver cancer cells growth. So applying PLA/ Fe_3O_4 nanomagnetic microsphere as drug carrier not only has good targeting capacity, but also helps to control cancer cell growth by toxicity effect of carrier and enhance targeted drug efficiency.

Competing Interests

The authors declare that they have no competing interests.

Acknowledgments

This work was financially supported by Research Foundation of the Chongqing Jiaotong University (16JDKJC-A035) and Chongqing Post-Doctoral Study Foundation (Xm2016128).

References

- [1] L. H. Reddy, J. L. Arias, J. Nicolas, and P. Couvreur, "Magnetic nanoparticles: design and characterization, toxicity and biocompatibility, pharmaceutical and biomedical applications," *Chemical Reviews*, vol. 112, no. 11, pp. 5818–5878, 2012.
- [2] L. Biao, G. Jian-guo, W. Qi et al., "Preparation of nanometer cobalt particles by polyol reduction process and mechanism research," *Materials Transactions*, vol. 46, no. 4, pp. 1865–1867, 2010.
- [3] Z. Ying, J. Shengming, Q. Guanzhou et al., "Preparation of ultrafine nickel powder by polyol method and its oxidation product," *Materials Science and Engineering B*, vol. 122, no. 1, pp. 222–225, 2013.
- [4] C.-C. Huang, K.-Y. Chuang, C.-P. Chou et al., "Size-control synthesis of structure deficient truncated octahedral $\text{Fe}_{3-\delta}\text{O}_4$ nanoparticles: high magnetization magnetites as effective hepatic contrast agents," *Journal of Materials Chemistry*, vol. 21, no. 20, pp. 7472–7479, 2011.
- [5] H. T. Hai, H. Kura, M. Takahashi, and T. Ogawa, "Facile synthesis of Fe_3O_4 nanoparticles by reduction phase transformation from $\gamma\text{-Fe}_2\text{O}_3$ nanoparticles in organic solvent," *Journal of Colloid and Interface Science*, vol. 341, no. 1, pp. 194–199, 2010.
- [6] G. Utkan, F. Sayar, P. Batat, S. Ide, M. Kriechbaum, and E. Pişkin, "Synthesis and characterization of nanomagnetite particles and their polymer coated forms," *Journal of Colloid and Interface Science*, vol. 35, no. 2, pp. 372–379, 2011.
- [7] S. Ni and R. V. Ramanujan, "Doxorubicin loaded PLA coated iron oxide nanoparticles for targeted drug delivery," *Materials Science and Engineering C*, vol. 30, no. 7, pp. 484–490, 2010.
- [8] S. Liu, Y. Han, R. Qiao et al., "Investigations on the interactions between plasma proteins and magnetic iron oxide nanoparticles with different surface modifications," *Journal of Physical Chemistry C*, vol. 114, no. 49, pp. 21270–21276, 2010.
- [9] A. J. Cole, A. E. David, J. Wang, C. J. Galbán, H. L. Hill, and V. C. Yang, "Polyethylene glycol modified, cross-linked starch-coated iron oxide nanoparticles for enhanced magnetic tumor targeting," *Biomaterials*, vol. 32, no. 8, pp. 2183–2193, 2011.
- [10] N. Arsalani, H. Fattahi, and M. Nazarpour, "Synthesis and characterization of PVP-functionalized superparamagnetic Fe_3O_4 nanoparticles as an MRI contrast agent," *Express Polymer Letters*, vol. 4, no. 6, pp. 329–338, 2010.
- [11] D.-H. Zhang, G.-D. Li, J.-X. Li, and J.-S. Chen, "One-pot synthesis of Ag- Fe_3O_4 nanocomposite: a magnetically recyclable and efficient catalyst for epoxidation of styrene," *Chemical Communications*, no. 29, pp. 3414–3416, 2008.
- [12] A. Sugunan, H. C. Warad, M. Boman, and J. Dutta, "Zinc oxide nanowires in chemical bath on seeded substrates: role of hexamine," *Journal of Sol-Gel Science and Technology*, vol. 39, no. 1, pp. 49–56, 2006.
- [13] W. Jiang, Z. Sun, F. Li et al., "A novel approach to preparing magnetic protein microspheres with core-shell structure," *Journal of Magnetism and Magnetic Materials*, vol. 323, no. 5, pp. 435–439, 2011.
- [14] E. Iglesias-Silva, J. Rivas, L. M. León Isidro, and M. A. López-Quintela, "Synthesis of silver-coated magnetite nanoparticles," *Journal of Non-Crystalline Solids*, vol. 353, no. 8-10, pp. 829–831, 2007.
- [15] Z. Zou, A. G. Xuan, Z. G. Yan, Y. X. Wu, and N. Li, "Preparation of Fe_3O_4 particles from copper/iron ore cinder and their microwave absorption properties," *Chemical Engineering Science*, vol. 65, no. 1, pp. 160–164, 2010.
- [16] J. Liang, L. Li, M. Luo, J. Fang, and Y. Hu, "Synthesis and properties of magnetite Fe_3O_4 via a simple hydrothermal route," *Solid State Sciences*, vol. 12, no. 8, pp. 1422–1425, 2010.
- [17] Y. Yin, S. Zhou, C. Min, and L. Wu, "Preparation of rattle-type magnetic mesoporous carbon spheres and their highly efficient adsorption and separation," *Journal of Colloid and Interface Science*, vol. 361, no. 2, pp. 527–533, 2011.
- [18] W. Beck, C. G. Souza, T. L. Silva, M. Jafelicci, and L. C. Varanda, "Formation mechanism via a heterocoagulation approach of FePt nanoparticles using the modified polyol process," *The Journal of Physical Chemistry C*, vol. 115, no. 21, pp. 10475–10482, 2011.
- [19] Y. Zhan, R. Zhao, F. Meng et al., "Oriented growth of magnetite along the carbon nanotubes via covalently bonded method in a simple solvothermal system," *Materials Science and Engineering B*, vol. 176, pp. 779–784, 2011.
- [20] J. Töpfer and A. Angermann, "Nanocrystalline magnetite and Mn-Zn ferrite particles via the polyol process: synthesis and magnetic properties," *Materials Chemistry and Physics*, vol. 129, no. 1, pp. 337–342, 2011.
- [21] B. Wang, B. Wang, P. Wei, X. Wang, and W. Lou, "Controlled synthesis and size-dependent thermal conductivity of Fe_3O_4 magnetic nanofluids," *Dalton Transactions*, vol. 41, no. 3, pp. 896–899, 2012.
- [22] Z. Pu, M. Cao, J. Yang, K. Huang, and C. Hu, "Controlled synthesis and growth mechanism of hematite nanorhombhedra, nanorods and nanocubes," *Nanotechnology*, vol. 17, no. 3, pp. 799–804, 2006.
- [23] R. Turcu, O. Pana, A. Nan, I. Craciunescu, O. Chauvet, and C. Payen, "Polypyrrole coated magnetite nanoparticles from water based nanofluids," *Journal of Physics D: Applied Physics*, vol. 41, no. 24, Article ID 245002, 2008.

- [24] E. Maltas, M. Ozmen, H. C. Vural, S. Yildiz, and M. Ersoz, "Immobilization of albumin on magnetite nanoparticles," *Materials Letters*, vol. 65, no. 23-24, pp. 3499–3501, 2011.
- [25] X. Wang, G. Xi, Y. Liu, and Y. Qian, "Controllable synthesis of PbSe nanostructures and growth mechanisms," *Crystal Growth & Design*, vol. 8, no. 4, pp. 1406–1411, 2008.
- [26] M. Mahmoudi, A. Simchi, M. Imani, P. Stroeve, and A. Sohrabi, "Templated growth of superparamagnetic iron oxide nanoparticles by temperature programming in the presence of poly(vinyl alcohol)," *Thin Solid Films*, vol. 518, no. 15, pp. 4281–4289, 2010.

Research Article

Effect of Annealing Temperature and Spin Coating Speed on Mn-Doped ZnS Nanocrystals Thin Film by Spin Coating

Noor Azie Azura Mohd Arif,¹ Chong Chee Jiun,¹ and Sahbudin Shaari²

¹Centre for Pre-University Studies, Universiti Malaysia Sarawak, 94300 Kota Samarahan, Sarawak, Malaysia

²Institute of Microengineering and Nanoelectronics, Universiti Kebangsaan Malaysia, 43600 Bangi, Selangor, Malaysia

Correspondence should be addressed to Noor Azie Azura Mohd Arif; manaazura@unimas.my

Received 7 October 2016; Revised 13 December 2016; Accepted 19 December 2016; Published 4 January 2017

Academic Editor: Biswanath Bhoi

Copyright © 2017 Noor Azie Azura Mohd Arif et al. This is an open access article distributed under the Creative Commons Attribution License, which permits unrestricted use, distribution, and reproduction in any medium, provided the original work is properly cited.

ZnS:Mn nanocrystals thin film was fabricated at 300°C and 500°C via the spin coating method. Its sol-gel was spin coated for 20 s at 3000 rpm and 4000 rpm with metal tape being used to mold the shape of the thin film. A different combination of these parameters was used to investigate their influences on the fabrication of the film. Optical and structural characterizations have been performed. Optical characterization was analyzed using UV-visible spectroscopy and photoluminescence spectrophotometer while the structural and compositional analysis of films was measured via field emission scanning electron microscopy and energy dispersive X-ray. From UV-vis spectra, the wavelength of the ZnS:Mn was 250 nm and the band gap was within the range 4.43 eV–4.60 eV. In room temperature PL spectra, there were two emission peaks centered at 460 nm and 590 nm. Under higher annealing temperature and higher speed used in spin coating, an increase of 0.05 eV was observed. It was concluded that the spin coating process is able to synthesize high quality spherical ZnS:Mn nanocrystals. This conventional process can replace other high technology methods due to its synthesis cost.

1. Introduction

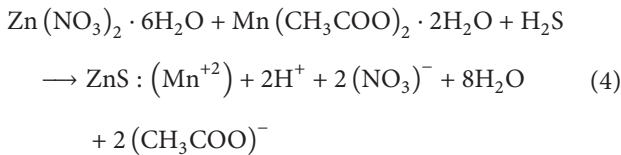
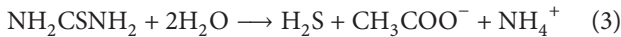
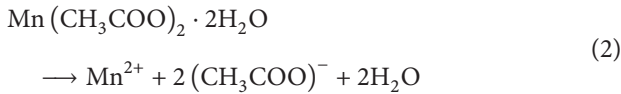
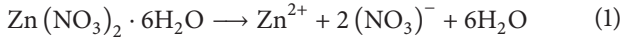
ZnS is one of the most studied nanomaterials. It is relatively easy to fabricate the nanomaterial with the intended optical and electrical properties through controlling the shape of its nanostructure [1, 2]. It has a wide energy band gap with a value of 3.68 eV for cubic phase and 3.77 eV for hexagonal phase [3–10]. There are several physical methods (ion sputtering, laser ablation, gas condensation, pyrolysis, etc.) and chemical methods (solvothermal, photochemical, electrochemical, thermolytic, sol-gel, etc.) to synthesize nanocrystalline thin film and to control its crystal size [11]. Sol-gel is a cheap chemical method that fabricates material through the process of phase change from liquid phase (sol) to solid phase (gel) [12–14]. Fabrication that employs this method will usually be entailed by either spin coating or dip coating process followed by heat treatment process. Walker et al. (1995) found that annealing treatment is required to reduce material defects. Annealing treatment is a common

procedure in fabrication of nanomaterial to either improve the quality of crystal or stabilize the structure at a temperature [15]. Due to the fact that the dopant is able to extend the capability of a semiconductor compound, this work focused on doped ZnS. Besides, the luminance color of the doped material changes according to the dopant used. The commonly used dopant is manganese ions (Mn^{2+}) and copper ions (Cu^{2+}). Mn^{2+} produces orange emission while Cu^{2+} produces green emission [16–19]. Parameters such as annealing temperature and speed of rotation were used in these experiments to investigate their influence on the fabrication of nanocrystalline thin film. Based on [20–22], the influence of the spin coating speed will affect the band gap of the thin film. The band gap increases roughly with the increase in annealing temperature and spin coating speed. This work aims to identify the characteristics of zinc sulphide doped manganese (ZnS:Mn) fabricated using several combinations of annealing temperatures and speeds of spin coating.

2. Methodology

In this study, ZnS:Mn thin films were prepared using the conventional triple process (sol-gel, self-assembly, and spin coating process). The morphology and composition of the films were studied using a field emission scanning electron microscope (FE-SEM) (model Zeiss Supra 55) and energy dispersive X-ray (EDX) while the optical properties of the film were studied using a photoluminescence (PL) spectrometer (model Perkin Elmer LS 55) and ultraviolet-visible spectroscopy (UV-Vis) (model Lambda 650, Perkin Elmer). Characterization was done at room temperature. Sections 2.1 and 2.2 describe each fabrication step in detail.

2.1. Preparation of Sol. The solution was prepared according to the formula $Zn_{(1-x)}Mn_xS$ at $x = 0.05$ using hydrated zinc nitrate, manganese acetate, thiourea, 2-propanol, hydrochloric acid, and distilled water. In the reaction, hydrated zinc nitrate and manganese acetate were dissolved in 2-propanol and distilled water to produce zinc and manganese ions. Then, hydrochloric acid was added to the solution as a catalyst. After 5 seconds, thiourea was added to the solution to produce sulfur. A clear solution was produced after 48 hours of stirring. Equations (1)–(3) describe the reactions that took place during the preparation while (4) describes the overall preparation process.



2.2. Preparation of Thin Film. ZnS:Mn sol was deposited on a glass substrate using a spin coater (model WS-400BX-6NPP/LITE). The sample was rotated with high efficiency at the speed of 3000 rpm for 20 seconds. During the process, the centripetal acceleration spread the sol in all directions and the thin film could only be produced by sol that adhered on the surface of the substrate. In order to maximize the amount of sol that could adhere on the substrate, a metal tape was placed on the substrate acting as a wall to hold the structure of the sol during the spin coating process. This process was repeated with another spin coating speed of 4000 rpm to observe the effect of speed on the material produced. During the deposition process, the arrangement of the particles in nanocrystalline ZnS:Mn remained unorganized. Heat treatment was used to reduce material defects. After that, the thin film was cooled to room temperature at normal rates. Figure 1 shows the position of glass substrate during the heating process. Two heating temperatures (300°C and 500°C) were used to study the influence of heat temperature

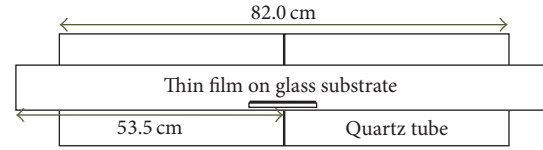


FIGURE 1: Position of the substrate during the annealing process.

on the optical and microstructural properties of the thin films produced.

3. Results and Discussion

3.1. Photoluminescent (PL) Spectra. Figures 2(a) and 2(b) display the spectrum of photoluminescence for all the thin films when they underwent the 250 nm excitation wavelength. In both figures, three emission spectra were observed. The first peak was produced within wavelength ranging from 350 to 450 nm. This is evident to the recombination of electron trapped in the energy gap of ZnS [23]. From an earlier research investigation, it was mentioned that the emission was not affected by the Mn dopant [24, 25]. The second peak is the highest located at the center (500 nm) and was generated due to the impact of the first excited wavelength of 250 nm. This huge peak at 500 nm is not related to the sample. Lastly, the orange emission peak at 590 nm was attributed to ${}^4T_1 \rightarrow {}^6A_1$ transition in d-orbital of Mn^{2+} . Besides these three bands, a small peak can be observed at 460 nm which was caused by the presence of Mn ions (d-orbital) in the host lattice ZnS [26].

3.2. Absorption and Transmittance Spectra. It is well known that the effect of 3D quantum confinement only occurs when the size of nanocrystals is equal to de Broglie wavelength of electrons or holes. The resulting shift in the semiconductor absorption is a consequence of quantum confinement related to the improvement of energy gap between valence and conduction band. Figures 3(a) and 3(b) show the absorption spectrum for thin films produced at different speeds of spin coating and temperatures of annealing treatment. In these figures, the absorption peak occurred at around 250 nm. The resulting spectrum was a blue shift which was different with the bulk ZnS (345 nm). Based on previous studies, ZnS has great potential to absorb light at wavelength ranging between 220 nm and 350 nm [4].

Transmittance spectra, which are the inverse in the absorption spectrum, showed that almost 85% transmittance is within the visible range. As shown in Figures 4(a) and 4(b), the sharp fall of transmittance spectrum occurs in the vicinity of energy band region. The absorption coefficient α can be calculated from the data of transmittance using Manificier model [27].

3.3. Optical Energy Band Gap E_g . The energy band gap E_g for the thin films was studied as well. These values were obtained from the plot of $(\alpha h\nu)^2$ against $h\nu$ by superimposing a straight line on the data points as shown in Figure 5. The values of

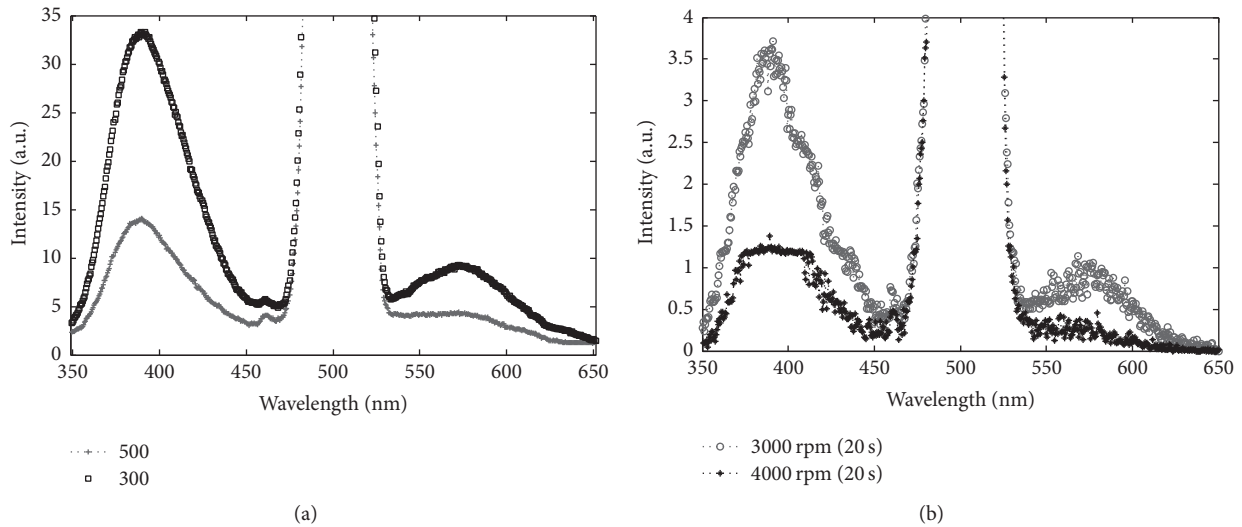


FIGURE 2: Photoluminescence spectra of Mn-doped ZnS nanocrystals at different (a) temperatures and (b) times and speeds of rotation.

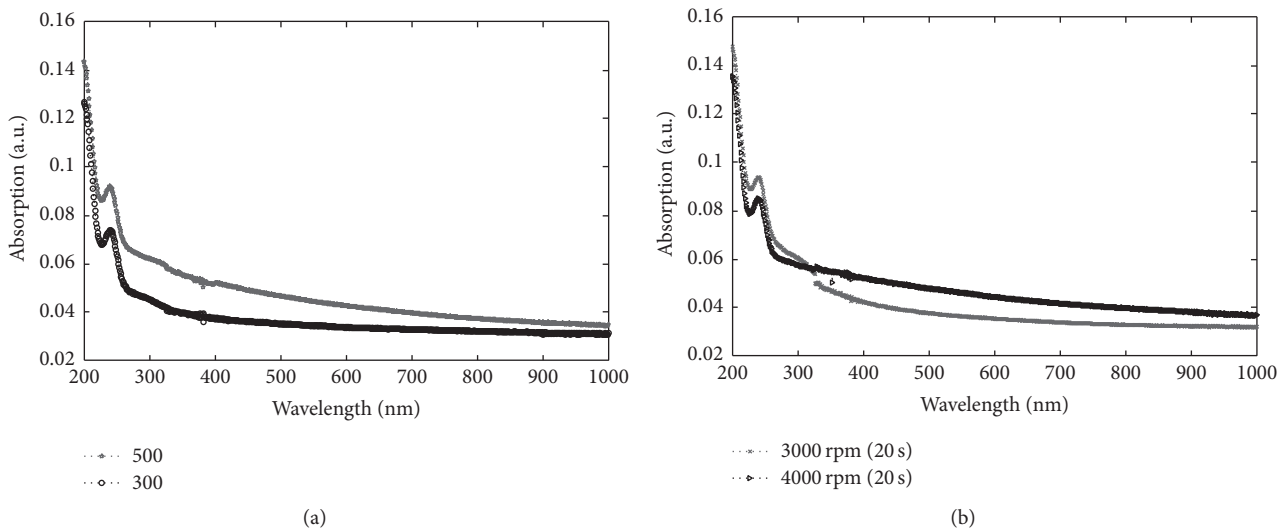


FIGURE 3: The absorption spectra of ZnS:Mn nanocrystals fabricated at different (a) temperatures and (b) times and speeds of rotation.

E_g obtained were around 4.43 eV–4.60 eV depending on the fabrication procedure chosen.

3.4. Effect of Annealing Temperature. Figure 2(a) shows that the intensity of the emission spectrum decreases with an increase in annealing temperature. The level of intensity dropped from 41 a.u. to 14 a.u. for the first emission band while the level for the last emission dropped from 13 a.u. to 4 a.u. for the third emission. Even the small peak at 460 nm dropped as well but it was not as much as the other two emission bands. The higher temperature caused more Mn^{2+} ions to be released from the ZnS matrix which lowered the peak at 590 nm. Besides degradation in the intensity spectrum, higher annealing temperature also increases the light absorption ability of the thin film. From Figure 3(a), the low annealing treatment dampens the absorption ability in the visible region. For transmittance level shown in Figure 4(a),

the sharp fall region for both thin films is within the same range regardless of the annealing temperature used. The level of transmittance in visible range remained at an equal level as well.

In the study of energy band gap, the thin film that was produced under higher annealing temperature has higher E_g value of 4.60 eV. But the increase was only at 0.05 eV. The increase in the energy band gap, absorption, and intensity spectrum could be attributed to the reduction in the size of particles adhered on the substrate as shown in Figure 6. From the FE-SEM images, the size of the spherical particles produced under annealing temperatures 300°C and 500°C was 30.0–36.8 nm and 21.8–23.2 nm, respectively. These images prove that the size of particles reduced when the annealing temperature was raised. This occurred because of potential and kinetic energy during the annealing process [28]. Figure 7 shows the EDX result of ZnS:Mn thin film with composition

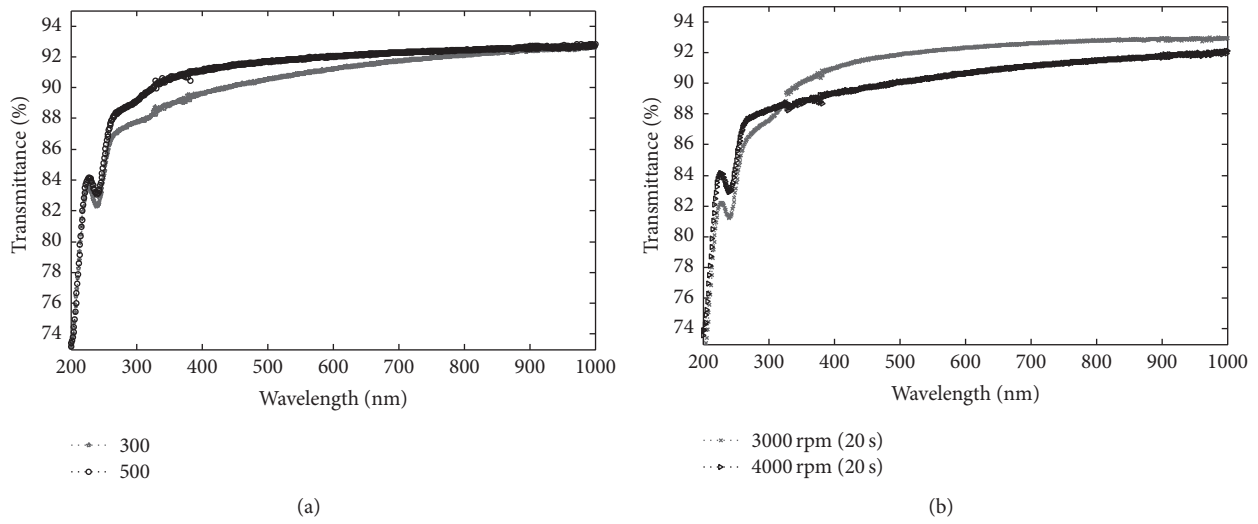


FIGURE 4: Transmittance spectra of ZnS:Mn nanocrystals fabricated at different (a) temperatures and (b) times and speeds of rotation.

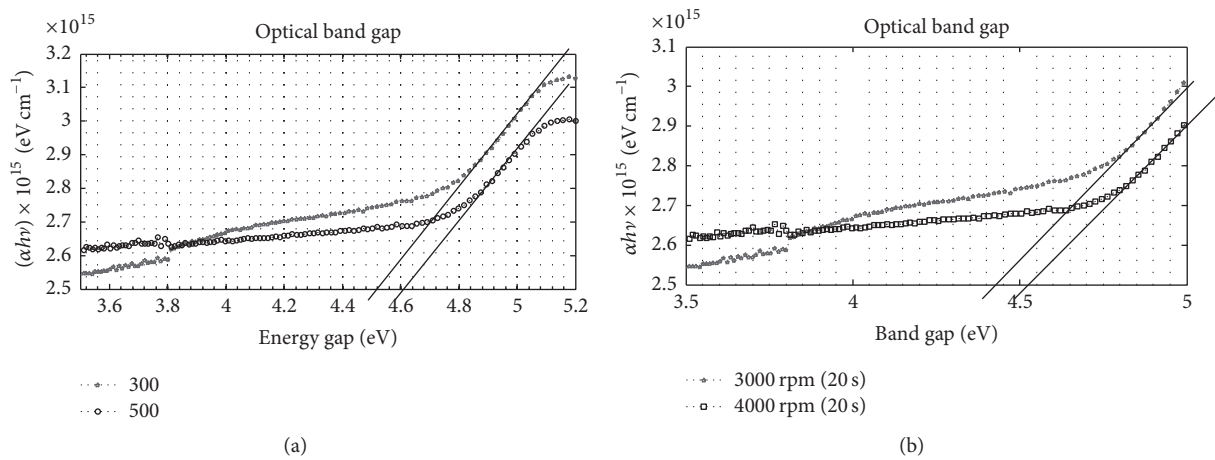


FIGURE 5: Measurement of the energy gap of ZnS:Mn nanocrystals fabricated at different (a) temperatures and (b) times and speeds of rotation.

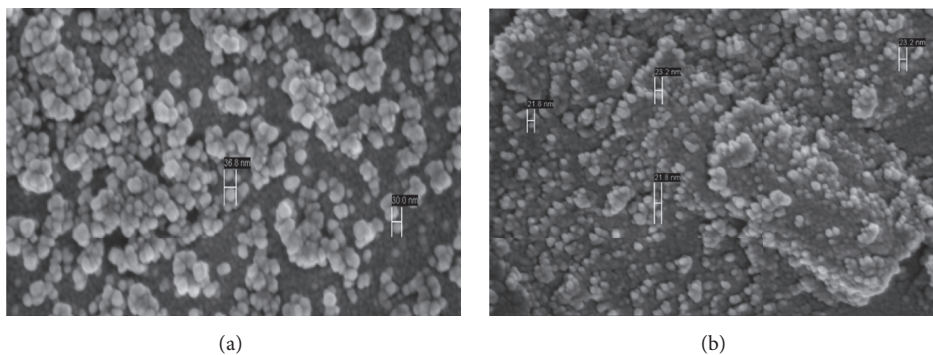


FIGURE 6: Nanocrystalline thin film produced at the heating temperatures of (a) 300°C and (b) 500°C with grain sizes of 30.0–36.8 nm and 21.8–23.2 nm, respectively.

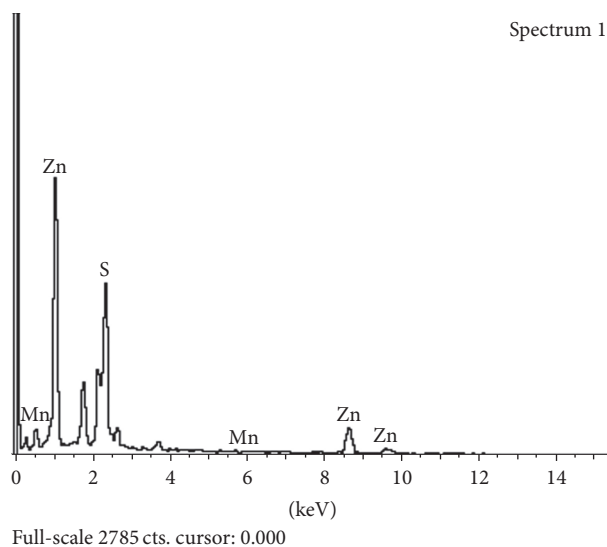


FIGURE 7: EDX result of ZnS:Mn thin film with composition $Zn_{(1-x)}Mn_xS$ at $x = 0.05$.

$Zn_{(1-x)}Mn_xS$ at $x = 0.05$. The proportion of the constituent elements measured was Zn = 65.33%, S = 26.84%, and Mn = 7.83%.

3.5. Effect of Spin Coating Speed. From Figure 2(b), a decrease in the intensity of the emission spectrum for the first and third band is observed when a higher speed of spin coating was used in the deposition process. The intensity of the thin film that underwent higher speed of coating dropped by at least 50% compared to the intensity emitted by another thin film. For the first band, the peak dropped drastically from 3.8 a.u. to 1.3 a.u. while a smaller drop occurred at the third band from 1.1 a.u. to 0.5 a.u. These drops suggest that a slower speed of spin coating should be chosen if high level of intensity in the emission of thin film is a desired property.

From the absorption spectra in Figure 3(b), the light absorption ability in the thin film that underwent higher speed of spin coating is weaker but the differences are not as obvious as the differences observed in the emission spectra. In terms of transmittance, the sharp fall region for both thin films is within the same range again as shown in Figure 4(b). However, for the thin film that underwent higher speed of spin coating, the transmittance level was slightly higher but still within the visible range. For the study of energy band gap, E_g value is found to be higher for the thin film that was fabricated using higher speed of spin coating. When produced at 4000 rpm, the energy band gap was found to be 4.53 eV while it was 4.43 eV for another thin film. This suggests that the nanoparticles of the thin film produced via higher speed of spin coating were smaller. The reduction of particle size as well as thin film thickness can be verified using general relationship (5) [29, 30]. Generally, by calculating or plotting using the experimental values $\omega = 3000$ rpm (20 s) and $\omega = 4000$ rpm (20 s), the relation between thickness H and spin rotation can be determined:

$$H \propto \omega^{-1} t^{-0.5}. \quad (5)$$

4. Conclusions

Spherical ZnS:Mn nanocrystals thin films with grain size of 21.8–36.8 nm have been fabricated via spin coating method with thin film being molded by a metal tape at the spin coating stage. The UV-vis spectra of the ZnS:Mn nanocrystals reveal that the limiting wavelength is 250 nm. The PL spectra for different temperatures show that the decrement in annealing temperature increases the maximum properties. The PL spectra display blue and orange emission while the absorption edge appears at around 250 nm. From the measurements of transmittance for the films, the direct band gap values have been measured and they fall within the range 4.43 eV–4.60 eV. This conventional process is a simple and very useful method to synthesize high quality sphere-like ZnS:Mn nanocrystals thin films. It will be a promising low-cost alternative to other high technology methods in the future.

Competing Interests

The authors declare that they have no competing interests.

Acknowledgments

This work was supported by Universiti Kebangsaan Malaysia Research University Grant and Universiti Malaysia Sarawak Research University Grant (RAGS/SG01(1)/1310/2015(04)), which is gratefully acknowledged.

References

- [1] S. Hamad, S. M. Woodley, and C. R. A. Catlow, "Experimental and computational studies of ZnS nanostructures," *Molecular Simulation*, vol. 35, no. 12-13, pp. 1015–1032, 2009.
- [2] S. Nadana, C. Shanmugam, S. Arumugam, V. Govindan, and K. Nadesan, "Temperature controlled synthesis of ZnS nanocrystals by simple chemical precipitation," *Walailak Journal of Science and Technology*, vol. 10, no. 2, pp. 149–157, 2013.
- [3] K. Manzoor, V. Aditya, S. R. Vadera, N. Kumar, and T. R. N. Kutty, "Spontaneous organisation of ZnS nanoparticles into monocryalline nanorods with highly enhanced dopant-related emission," *Journal of Physics and Chemistry of Solids*, vol. 66, no. 7, pp. 1164–1170, 2005.
- [4] L. W. Schwartz, "Analysis of spin coating for non-ideal conditions," in *Proceedings of the International Coating Science and Technology Symposium*, 2008.
- [5] P. M. B. Walker, *The Wordsworth Dictionary of Science & Technology*, Wordsworth Editions, Hertfordshire, UK, 1995.
- [6] K. H. Yoon, J. K. Ahn, and J. Y. Cho, "Optical characteristics of undoped and Mn doped ZnS films," *Journal of Materials Science*, vol. 36, no. 6, pp. 1373–1376, 2001.
- [7] T. M. Thi, N. T. Hien, D. X. Thu, and V. Q. Trung, "Thin films containing Mn-doped ZnS nanocrystals synthesised by chemical method and study of some of their optical properties," *Journal of Experimental Nanoscience*, vol. 8, no. 5, pp. 530–538, 2013.
- [8] F. A. La Porta, J. Andrés, M. S. Li, J. R. Sambrano, J. A. Varela, and E. Longo, "Zinc blende versus wurtzite ZnS nanoparticles: control of the phase and optical properties by tetrabutylammonium hydroxide," *Physical Chemistry Chemical Physics*, vol. 16, no. 37, pp. 20127–20137, 2014.

- [9] H. A. T. Al-Ogaili, "Synthesis of colloidal zinc sulfide nanoparticle via chemical route and its structural and optical properties," *International Journal of Advanced Research in Science, Engineering and Technology*, vol. 3, no. 3, pp. 1587–1592, 2016.
- [10] F. Al-Sagheer, A. Bumajdad, M. Madkour, and B. Ghazal, "Optoelectronic characteristics of ZnS quantum dots: Simulation and experimental investigations," *Science of Advanced Materials*, vol. 7, no. 11, pp. 2352–2360, 2015.
- [11] F. M. Daniel, *Novel ZnS nanostructures: synthesis, growth, mechanism and applications [Ph.D. thesis]*, Georgia Institute of Technology, 2006.
- [12] A. A. M. A. Noor, S. Shaari, and S. A. R. Mohammad, "Improving the production of self-assembled ZnS:Mn nanocrystals through the modification of sol gel—spin coating approaches," *Advanced Materials Research*, vol. 1024, pp. 23–26, 2014.
- [13] Q. Ma, Q. Xu, C.-L. Tsai, F. Tietz, and O. Guillon, "A novel sol-gel method for large-scale production of nanopowders: preparation of $\text{Li}_{1.5}\text{Al}_{0.5}\text{Ti}_{1.5}(\text{PO}_4)_3$ as an example," *Journal of the American Ceramic Society*, vol. 99, no. 2, pp. 410–414, 2016.
- [14] G. J. Owens, R. K. Singh, F. Foroutan et al., "Sol-gel based materials for biomedical applications," *Progress in Materials Science*, vol. 77, pp. 1–79, 2016.
- [15] N. Shanmugam, S. Cholan, N. Kannadasan, K. Sathishkumar, and G. Viruthagiri, "Effect of annealing on the zns nanocrystals prepared by chemical precipitation method," *Journal of Nanomaterials*, vol. 2013, Article ID 351798, 7 pages, 2013.
- [16] N. Onuma, *Synthesis and characterization of nanocrystalline ZnS:Mn²⁺ polyelectrolyte [Tesis Sarjana]*, Mahidol University, 2005.
- [17] S. Prabha, H. Lubna, and M. M. Malik, "Luminescence and morphological kinetics of functionalized ZnS colloidal nanocrystals," *ISRN Optics*, vol. 2012, Article ID 621908, 8 pages, 2012.
- [18] Z. Paulina, M. Ewa, and P. Malgorzata, "ZnS Cu-doped quantum dots," *Biotechnology and Food Sciences*, vol. 78, no. 1, pp. 53–69, 2014.
- [19] S. Pramanik, S. Bhandari, S. Roy, and A. Chattopadhyay, "Synchronous tricolor emission-based white light from quantum dot complex," *The Journal of Physical Chemistry Letters*, vol. 6, no. 7, pp. 1270–1274, 2015.
- [20] A. A. David, M. A. Saint, and A. Oluwaseun, "Effect of spin coating speed on some optical properties of ZnO thin films," *Journal of Materials Science and Chemical Engineering*, vol. 4, pp. 1–6, 2016.
- [21] A. Battal, D. Tatar, A. Kocyigit, and B. Duzgun, "Comparison effect of spin speeds and substrate layers on properties of doubly doped tin oxide thin films prepared by SOL-GEL spin coating method," *Journal of Ovonic Research*, vol. 10, no. 2, pp. 23–34, 2014.
- [22] T. D. Malevu and R. O. Ocaya, "Effect of annealing temperature on structural, morphology and optical properties of ZnO nanoneedles prepared by Zinc-Air system method," *International Journal of Electrochemical Science*, vol. 10, pp. 1752–1761, 2015.
- [23] E. Mohaghehpour, M. Rabiee, F. Moztarzadeh et al., "Controllable synthesis, characterization and optical properties of ZnS:Mn nanoparticles as a novel biosensor," *Materials Science and Engineering C*, vol. 29, no. 6, pp. 1842–1848, 2009.
- [24] W. Q. Peng, S. C. Qu, G. W. Cong, X. Q. Zhang, and Z. G. Wang, "Optical and magnetic properties of ZnS nanoparticles doped with Mn^{2+} ," *Journal of Crystal Growth*, vol. 282, no. 1-2, pp. 179–185, 2005.
- [25] W. Q. Peng, S. C. Qu, G. W. Cong, and Z. G. Wang, "Concentration effect of Mn^{2+} on the photoluminescence of ZnS:Mn nanocrystals," *Journal of Crystal Growth*, vol. 279, no. 3-4, pp. 454–460, 2005.
- [26] D. Mohanta, G. A. Ahmed, A. Choudhury, F. Singh, and D. K. Avasthi, "Properties of 80-MeV oxygen ion irradiated ZnS:Mn nanoparticles and exploitation in nanophotonics," *Journal of Nanoparticle Research*, vol. 8, no. 5, pp. 645–652, 2006.
- [27] R. Maity and K. K. Chattopadhyay, "Synthesis and optical characterization of ZnS and ZnS:Mn nanocrystalline thin films by chemical route," *Nanotechnology*, vol. 15, no. 7, pp. 812–816, 2004.
- [28] M. S. Ab-Rahman, N. A. A. M. Arif, and S. Shaari, "Effect of thermal treatment on the morphology of ZnS: Mn nanocrystals," *World Applied Sciences Journal*, vol. 12, no. 9, pp. 1505–1511, 2011.
- [29] E. Mohajerani, F. Farajollahi, R. Mahzoon, and S. Baghery, "Morphological and thickness analysis for PMMA spin coated films," *Journal of Optoelectronics and Advanced Materials*, vol. 9, no. 12, pp. 3901–3906, 2007.
- [30] V. Stanić, T. H. Etsell, A. C. Pierre, and R. J. Mikula, "Sol-gel processing of ZnS," *Materials Letters*, vol. 31, no. 1-2, pp. 35–38, 1997.